Glacial sculpting of a martian cratered landscape on the northeastern flank of the Hellas basin

Anna Grau Galofre, Alan D Howard, Alexander M Morgan, Sharon A Wilson, Jeffrey M Moore

Icarus 420 (2024) 116211

Contents lists available at ScienceDirect

Icarus

journal homepage: www.elsevier.com/locate/icarus

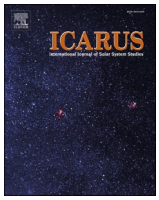

Glacial sculpting of a martian cratered landscape on the northeastern flank of the Hellas basin

Anna Grau Galofre [a,*], Alan D. Howard [b], Alexander M. Morgan [b,c], Sharon A. Wilson [c], Jeffrey M. Moore [d]

[a] Nantes Université, Univ. Angers, Le Mans Université, Laboratoire de Planétologie et Géosciences, CNRS UMR, 6112 Nantes, France
[b] Planetary Science Institute, Tucson, AZ, USA
[c] Center for Earth and Planetary Studies, National Air and Space Museum, Smithsonian Institution, Washington, DC, USA
[d] NASA Ames Research Center, Moffett Field, CA, USA

ARTICLE INFO

Keywords:
Mars(1007)
Glaciation(2302)
Planetary surfaces(2113)
Glaciers(2303)

ABSTRACT

The interiors and exteriors of the >25 km diameter Batson, Nako, Salkhad, and Jori craters (and McCauley crater to a lesser degree) on the northeastern rim of Hellas basin, Mars, were extensively modified by glacio-fluvial and glacio-lacustrine activity during the Middle and Late Amazonian, from some time before 1.4 Ga to the present as revealed by CTX, HiRISE, and CaSSIS observations. This work presents extensive descriptions and discussions of individual candidate glacial and glaciofluvial landforms associated with cratered landscapes, as well as their spatial association. We also present absolute age dates and a relative sequence of events, followed by a possible environmental reconstruction, involving a regional ice cover, subglacial meltwater, and ice-covered lakes. On crater interiors, inferred glacial modification included dissection of interior rims, emplacement of depositional aprons with basinward scarps, remnant glaciers and associated fresh shallow valleys, supraglacial debris, and candidate moraines. On crater exterior rims and on the plateaus surrounding Batson crater we describe moderate incision and sedimentation, subglacial meltwater runoff through Navua A Valles, candidate eskers, valleys discordant with topography but concordant with inferred ice flow direction, and hummocky material, among others. Wet-based glaciation and subglacial runoff may have been favored due to a locally enhanced geothermal heating or strain heating on steep crater slopes. This work presents a comprehensive and detailed characterization of landforms interpreted as glacial in origin, which could be used to guide identifications of glacial landforms in other cratered regions of Mars.

1. Introduction

The importance of ice in sculpting the surface of Mars remains uncertain. For early Mars, before about 3.6 Ga from present, current opinions about processes that degraded craters and created the equatorial valley networks range from relatively warm and wet conditions supporting runoff from rain or seasonal snows (Craddock and Howard, 2002; Howard, 2007; Ramirez and Craddock, 2018; Ramirez et al., 2020) to colder conditions with a thick ice cover of the highlands and occasional supraglacial melting (Wordsworth et al., 2013; Head and Marchant, 2014; Wordsworth, 2016). One intermediate case suggests basal melting of equatorial ice contributing to the formation of some valley networks (Grau Galofre et al., 2020).

For the Hesperian (~3.7-3.0 Ga) and Amazonian (~3.0 Ga-present) periods, the role of snow and ice is somewhat clearer. In the equatorial highlands scattered alluvial fans are likely sourced from meltwater from snow and ice accumulating on crater walls, with attendant incision of headwater valleys on crater walls and tectonic scarps (Moore and Howard, 2005; Williams et al., 2006; Kraal et al., 2008; Williams et al., 2011; Grant and Wilson, 2011, 2012, 2019; Morgan et al., 2014, 2022; Palucis et al., 2014; Wilson et al., 2021). In the mid-latitudes poleward from 25°N/S ice deposits and evidence of glacial flow include lobate debris aprons, lineated valley fills, concentric crater fills, and younger glacial-like forms (e.g., Baker et al., 2010; Levy et al., 2010, 2014, 2021; Dickson et al., 2012; Fastook and Head, 2014; Baker and Carter, 2019; Brough et al., 2019). A mantle deposit rich in water ice covers most of

* Corresponding author.
E-mail addresses: anna.graugalofre@univ-nantes.fr (A. Grau Galofre), ahoward@psi.edu (A.D. Howard), amorgan@psi.edu (A.M. Morgan), purdys@si.edu (S.A. Wilson), jeff.moore@nasa.gov (J.M. Moore).

https://doi.org/10.1016/j.icarus.2024.116211
Received 9 November 2023; Received in revised form 1 July 2024; Accepted 1 July 2024
Available online 5 July 2024

the mid to high-latitude region (Soderblom et al., 1973; Mustard et al., 2001; Kreslavsky and Head, 2002b; Conway and Balme, 2014). Melting of seasonal or glacial ice is hypothesized to have created local incision of fresh, shallow valleys, or FSVs in the latitude range of 35-50°N/S (Fassett et al., 2010; Howard and Moore, 2011; Hobley et al., 2014; Wilson et al., 2016). Poleward of 50°N/S ice deeply fills most craters, and scarps locally expose >100 m thick layers of nearly pure ice (Dundas et al., 2018, 2021).

The degree to which the abundant ice present in the mid-latitudes actively modified the cratered landscape is less clear, in part because the ice and dust mantle obscures the underlying substrate (Head et al., 2003; Gallagher et al., 2021). Current martian ice deposits are frozen to the ground (cold-based). These types of glaciers leave only very subtle erosive landscape imprints on Earth, if any (Atkins, 2013), which could be easily obscured by degradation or mantling on Mars. Small terminal "drop" moraines form in such glaciers if ice flow and landscape geometry enable supra- or englacial deposition and transport of sediment (e.g., Head and Marchant, 2003). Contrarily, warm-based or polythermal glaciation (basal meltwater is present at least sporadically) can produce dramatic landforms such as large moraines or glacial grooves on Earth, which remain largely elusive on Mars (Kargel et al., 1995; Johnson et al., 2019; Grau Galofre et al., 2022). The interplay of low gravity glacial dynamics, widely varying ice distribution due to orbital forcing, and long timespans, raises the question as to what landforms are distinctive of glacial sculpture on Mars, and hence what was the role and degree of glacial erosion in shaping the cratered landscapes of Mars throughout its history.

The efficacy of ice and glacial deposits to have modified crater interiors and exteriors on Mars is limited by the lower martian gravity, even in the presence of basal melt. Glacial hydrology theory applied to Mars (Grau Galofre et al., 2022) finds that basal frictional scour by sliding ice would be reduced by a factor of at least ~20 relative to terrestrial glaciers and ice sheets, but subglacial channelized drainage would be enhanced relative to Earth. Both the recent obscuration of the surface by martian mid-latitude ice and differences in ice accumulation and resurfacing dynamics on Mars relative to Earth limit our ability to assess what surface morphologies would be expected on martian landscapes based on morphology comparisons alone. The near-surface water inventory of Mars has been gradually diminishing over the Hesperian and Amazonian (Carr and Head, 2015). Substantially greater ice cover also existed in the lower mid-latitudes in the past, for example by findings of buried mid-latitude ice sheets (e.g., Bramson et al., 2015; Stuurman et al., 2016).

This paper discusses possible glacial and subglacial surface modification in a region of the northeastern slopes of the Hellas basin (29°S, 83°E, shown in Fig. 1), and describes a suite of candidate glacial landforms that may be of use for identifying sculpture by warm-based martian glaciation elsewhere. The region contains five contiguous craters >25 km diameter (McCauley, Jori, Batson, Nako and Salkhad, Fig. 1), which impacted into a ~150 km broad ridge projecting SSE into the Hellas depression. Several glaciers presently occupy deep valleys on the interior crater rims of Batson and Nako craters. Through geomorphic mapping and detailed study of relict landforms, we hypothesize that much more extensive ice covered much of the interior and exterior slopes of these craters during the Amazonian period. Candidate glacial landforms include broad, shallow grooves by sliding ice or basal runoff on steep slopes, terminal, and lateral moraines, whereas inferred subglaciofluvial landforms include crater floor benches and possible elements of the subglacial drainage system such as eskers, tunnel valleys, and hummocky corridors.

1.1. Background

The northeastern slope of the Hellas basin has experienced extensive Hesperian and Amazonian runoff, in particular through the Navua A Valles (Hargitai et al., 2017a, 2018a, 2018b) that forms the southern

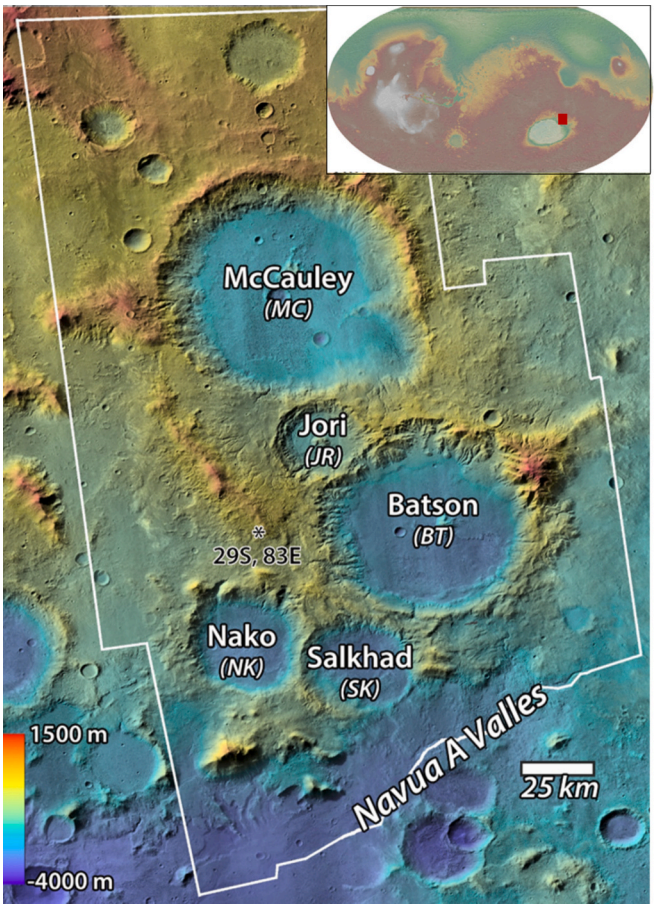

Fig. 1. Location map of study region showing named craters and extent of geomorphic mapping (white boundary). Unless otherwise noted, north is to the top in all figures. The "*" at 83°E, 29°S shows the regional location, and the inset shows the setting relative to the global topography (scale from 21,000 m to -8,000). Image and elevations sources for all figures are listed in supplementary figures, table S1. Context for all figures discussed is shown in Fig. 2.

boundary of the mapped region. Hargitai et al. (2018b) identified lakes, perhaps ice covered, occupying the lower floor of all of the craters studied here as evidenced by deltaic deposits or possible shorelines. Crater counts by Hargitai et al. (2018b) of mapped former lake extents yielded ages ranging from 410 ma to 3.9 Ga, suggesting a long-lived history of lacustrine activity. Several of the interpreted lake ages cluster at ~1 Ga. Most of the study region was geologically mapped at a scale of 1:1 million by Hargitai et al. (2018a) and the fluvial and lacustrine history of the region has been interpreted by Crown et al. (2005), Mest et al. (2010) and Hargitai et al. (2017a, 2017b, 2018b). Zhang et al. (2023) interpreted fan forms with terminal scarps in Batson, Jori, and Nako craters as being deltaic deposits. We adopt the general term "depositional apron" for these and related features. Exposures of light-toned deposits widespread within the mapped region (Howard et al., 2021) (e.g. Fig. S17) are interpreted to be Early to Mid-Amazonian airfall deposits. This light-toned deposit serves as a stratigraphic marker.

Mest et al. (2010) mapped an extensive, integrated drainage system northeast of the Batson crater region shown in Fig. 1, including Vichada Valles draining southwestward towards Batson crater, which they suggest is of Noachian age. This drainage likely formerly connected to the early Navua A Vallis system but became disconnected due to the Batson crater impact as well as ejecta from a 27.6 km crater at 86.1°E, 27.4°S and possibly by distal ejecta from the more distant 70 km Isil crater (87.9°E, 27.0°S). This drainage system appears to have been inactive subsequent to the Batson crater impact. The Navua A Vallis, which has been active during the Amazonian, presently heads southwest of Batson

crater (Fig. 1).

Hargitai and Gulick (2017) and Hargitai et al. (2018a, 2018b) discuss knobby terrain in Navua A Valles and in upland depressions in the Batson crater region, interpreting them to have formed after channel activity and to have possibly formed as till blocks, uncollapsed pingos, spring mounds, or exposed subsurface indurated material. These are mapped and discussed as glaciofluvial material in this paper.

Climate modeling by Wordsworth et al. (2013), Turbet et al. (2017), and Forget et al. (2006) suggest that the region northeast of the Hellas basin acts as a cold trap for water ice at high to moderate planetary spin axis obliquity configurations, concluding that this zone has been particularly prone to glaciation even across much of Mars' history. Forget et al. (2006) conclude that Amazonian net ice accumulation rates in this region were as high as ~100 mm/yr, rapidly deposited following summer solstice sublimation of the southern polar ice cap and northward transport of large amounts of water vapor forced by the deep Hellas basin. There is plenty of evidence for extant ice deposits ranging in age from ~1 Gyr to ~ 10 Myr, and multiple examples of LDAs, VFFs, and CCFs, as well as more recent GLF throughout the region (e.g., Kostama et al., 2010), with a peak density located around 40°S and 100°E, east and southwards from our region of interest. Hellas basin itself may have hosted ice-covered lakes (Moore and Wilhelms, 2001; Wilson et al., 2010).

The high concentration of extant ice deposits within the eastern Hellas basin as well as climate modeling suggesting past episodes of regional ice accumulation directed our attention to the site of the present study. The focus of this work is on identifying landforms and deposits that are indicative of former glaciation, in both the interior and exterior of craters, and use these to infer the paleoenvironmental characteristics of the region, while providing with descriptions useful to identify these landforms and landform associations elsewhere on Mars. Interpretive sections are included for each landform type and clearly designated. Short interpretive sections within paragraphs are denoted by "*Interpretation:*" and apply only to subject material in the paragraph. Longer interpretive sections start with a paragraph starting with "*Interpretation:*" and pertain to the end of the numbered section. Figures in the Supplementary Figures document are designated with an "S" prefix.

1.2. Data and methods

A database of imaging, thermal, and topographic data covering the region was assembled using ArcMap 10.8. This included 100 m/pixel Thermal Emission Imaging System (THEMIS) (Christensen et al., 2004)

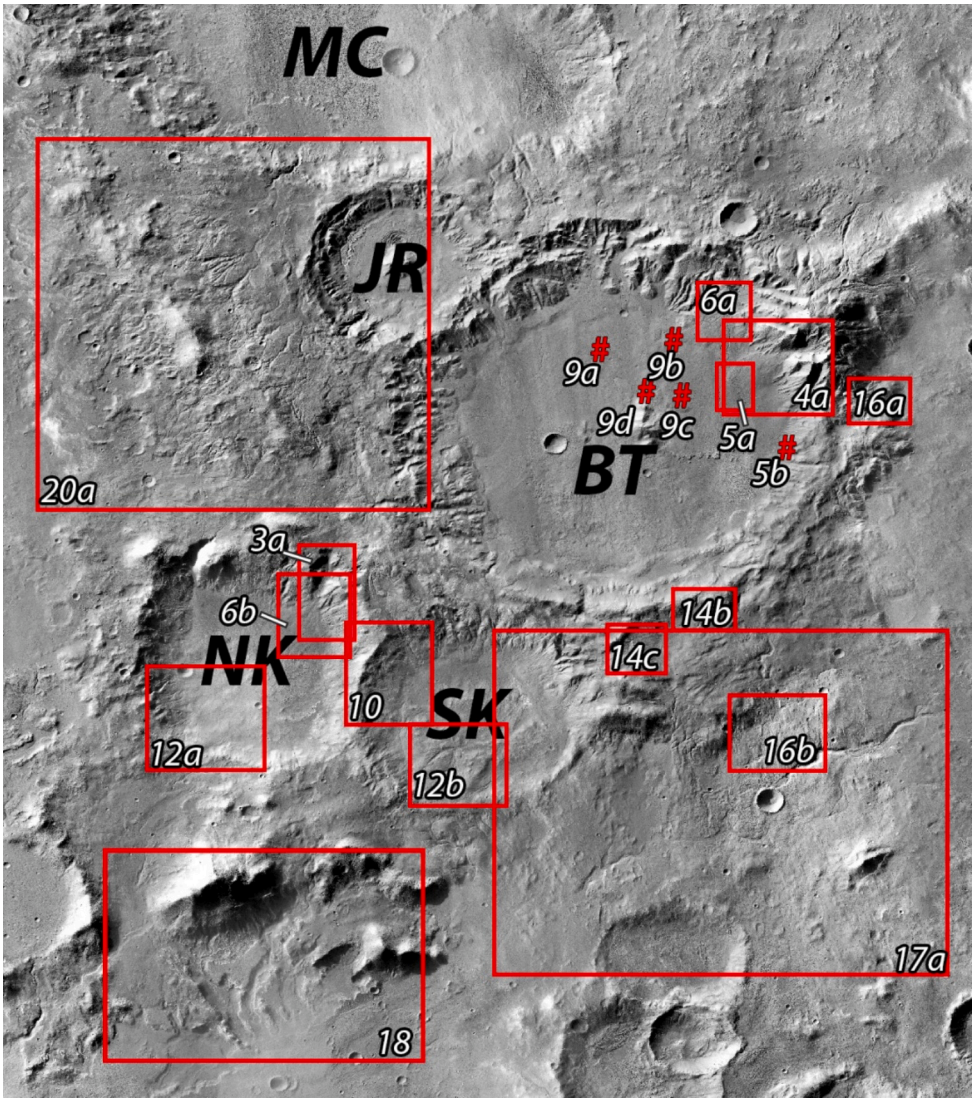

Fig. 2. Location map with context for figures. north is up, figure extent is 31°S, 82.1°E (bottom left) to 27.5°S, 85.3°E (top right). Scale bar is 40 km. Small-area figures are indicated by "#".

day and night IR global mosaics (Edwards et al., 2011), the 200 m/pixel HRSC and MOLA Blended DTM (Fergason et al., 2018), available 6 m/pixel Context Camera (CTX) (Malin et al., 2007) imaging as both individual images and the mosaicked Murray Laboratory global CTX V01 mosaic (Dickson et al., 2018), which is used as the default image base in illustrations, available Color and Stereo Surface Imaging System (CaSSIS) imaging at 4.6 m/pixel (Thomas et al., 2017), and available High Resolution Imaging Science Experiment (HiRISE) imaging at 0.25 and 0.5 m/pixel resolution (McEwen et al., 2007). We also incorporated HiRISE team-produced digital terrain model (DTM) products and stereo anaglyphs, CTX stereo DTMs produced through the MarsSI website (Quantin-Nataf et al., 2018), High Resolution Stereo Camera (HRSC) digital terrain maps (Jaumann et al., 2007; Gwinner et al., 2009), and THEMIS-based thermal inertia mapping (Fergason et al., 2006; Christensen et al., 2013). Topography shown in figures uses a mosaic of available DTM data, with priority increasing through MOLA, HRSC, and CTX DTMs. In addition, we used the ArcGIS 3D Analyst extension to construct topographic profiles from the DTM datasets and we interpreted the landforms and geomorphic history of the region through systematic mapping using ArcGIS. The source image and elevation data for all figures are presented in Supplementary Figures, Table S1, whereas Fig. 2 shows the map context of all figures in the text. In all figures, north is up unless indicated otherwise. When high resolution topographic data was not available, or its coverage was insufficient, we made use of the shadow shape technique to measure landform height (Chappelow and Sharpton, 2002; Daubar et al., 2014). For example, in section 4.6, sinuous ridge heights were measured using this technique, using CTX images B01_009929_1474_XI_32S274W with a light incidence angle of 75.09; and D19_034706_1509_XI_29S275W, with an incidence angle of 70.98, for a total of 33 ridge height measurement acquisitions.

Relative and absolute ages of geomorphic surfaces were dated by crater counting using the Crater Tools add-in for ArcGIS (Kneissl et al., 2011) and the CraterStats 2 software (Michael and Neukum, 2010) for crater retention age dating. To be consistent with previous studies, estimated crater count ages are expressed using the Ivanov (2001) production function and the Hartmann and Neukum (2001) chronology function. In tabulated values we also state ages based on the Hartmann and Daubar (2017) production function and the Hartmann (2005) and Michael (2013) chronology function.

2. Relative crater ages and general morphology of crater interiors

The inferred sequence of the five named >25 km diameter craters, from oldest to youngest is McCauley (including the McCauley-SE rim basin), Nako, Salkhad, Batson, and Jori. Age relationships are inferred from modification of crater rims by contiguous younger impacts and crater floor deposits inferred to be ejecta sourced from adjacent craters (Fig. S1). Ejecta sheet recognition is based upon nearly parallel ridges on the crater floors. Each of the mapped ejecta deposits has arrows pointing in the deposition direction from the inferred source crater in Fig. S1. The oldest age of McCauley crater is based on its advanced degree of degradation and having inferred ejecta sheets from Batson and Jori craters on its floor ("Distal Ejecta" in Fig. S1). The relative ages of Jori and Batson craters are less firm. Deep dissection of the shared rims of Batson and Jori craters obscures age relationships, but rough terrain with aligned ridges on the southern floor of Batson crater is tentatively identified as distal ejecta from Jori crater (Fig. S1). McCauley, Nako, and Salkhad crater have ejecta sheets on their floor from Batson crater. Salkhad crater indents the rim of Nako crater.

All five craters have been extensively infilled, potentially including ejecta, fluvial, eolian, lacustrine, and massive ice deposits. Despite their proximity, the five craters exhibit diverse geomorphic evolution. The highly degraded McCauley crater was only modestly affected by Amazonian post-impact processes. By contrast, Batson and Nako craters contain Late Amazonian glaciers (see Section 3.1). The depth of infilling and the degradation state (*Ds*) of the five craters are given in Table 1, where $Ds=(E-O)/E$: E is the expected depth of a fresh crater of the given diameter and O is the observed rim-to-floor depth (Forsberg-Taylor et al., 2004). $Ds \sim 1$ implies heavy degradation. Interestingly, the range of degradation states is relatively narrow (0.23 to 0.4) and small compared to the 0.5 to 0.9 range of many degraded equatorial craters (Forsberg-Taylor et al., 2004). With the exception of the 1449 m estimated fill depth of Batson crater, fill depths cluster from 950-1000 m.

Despite the appreciable estimated crater fill depths, the presence of ejecta sheets, rough terrain, and hummocky terrain on the floors of all the mapped craters except Jori indicate that the portions of crater floors mapped in Fig. S1 have not been significantly eroded or mantled by the candidate fluvial, glacial, and lacustrine processes discussed below, as well as aeolian processes, subsequent to the Batson and Jori crater impacts, although the Batson crater impact may account for large proportion of the infilling of Nako and Salkhad craters. Eolian erosion and deposition on crater floors has likewise been modest, primarily limited to eolian infilling of depressions at the decameter scale.

Both Nako and Salkhad craters have hilly elevated terrain on their southern crater floors mapped as "Mounded Crater Floor" in Fig. S1. This material is separated from the southern crater walls and does not have recognizable characteristics of being sedimentary deposits derived from crater wall erosion. *Interpretation:* We identify this unit as massive ejecta deposits derived from the Batson crater impact, possibly including avalanche materials from the northern walls of the two craters generated by the forces of the Batson crater impact. The inferred ejecta sheet on the southern floor of Batson crater may likewise contain landslide material sourced from crater walls triggered by the Jori impact.

3. Geomorphology of crater interiors

The descriptive names, geomorphometry, age, and figure references to geomorphic features discussed in Sections 3 and 4 are presented in Table 2. Context location of all figures is shown in Fig. 2.

3.1. Modern glacier like forms

Several deeply incised valleys along the interior rims of Batson and Nako craters contain deposits with longitudinal ridges following the valley axis, indicating that mass flow, likely slow, has driven deposit downslope (e.g., Fig. 3, Table 2). Fig. 3 shows a valley in northeastern Nako crater that hosts a deposit with pronounced longitudinal ridges. Near the upslope end, several infilled valleys converge into single south-flowing trunks, displaying a very similar planform morphology to terrestrial tributary mountain glaciers. Similar inferred deposits are present across the study area (e.g. two illustrated in Figs. 4, 6, and six less definitive attributions in Section 5.1 and mapped in Fig. 20), with the most extensive example extending from the northeast rim of Batson crater (Fig. 4). Here, the deposit below the headwall displays curvilinear

Table 1
Degradation state of the >25 km craters. Craters are listed from oldest to youngest.

Crater	Diameter (km)	Observed Depth[1] (m) (O)	Expected Depth[2] (m) (E)	Estimated Fill Depth (m) (E - O)	Degradation State (Ds) (E – O)/E
McCauley	101	3275	4228	953	0.23
Nako	47	1890	2880	991	0.34
Salkhad	46	1893	2855	963	0.34
Batson	86	2476	3915	1439	0.37
Jori	36	1511	2512	1001	0.40

[1] Based on average rim elevation minus minimum floor elevation from the DTMs.

[2] Based on fresh crater depth versus diameter statistics (Garvin et al., 2002, 2003; Forsberg-Taylor et al., 2004; Howard, 2007).

Table 2
Description of all landforms described in sections 3 (green background) and 4 (yellow background), including key examples with location, morphometry, and reference figures, sections, and symbols used to highlight them through the manuscript. '<res.' indicates below resolution.

Landform	Example locations	Length (km)	Width (m)	Depth (m)	Shape and topology	Age	Figures	sections	symbol	Interpre-tation
Glacial deposits	-29.4, 83.192	15-20	1000-3000	500-650	dendritic, U-shaped valleys	post-dating rim fluvial/ glacio- fluvial activity	Figure 3, 4b, 6, 18	3.1	**α**	extant debris covered glaciers
	-28.456, 84.548	16-24	1500-4500	200-700						
	-28.362, 84.135	12-21	3000 - 6000	100- 450						
Supra-glacial block clusters	-29.388, 83.188	0.1 - < res.	100 - <res.	< res.	irregular blocks, along ice flow lines	exposed after extant glacier deflation	Figure 3, 4b, 6a	3.1.1	**β**	supraglacial debris trains
	-28.452, 84.557	0.27 - <res.	250 - <res.	10 - <res.						
	-28.332, 84.168	0.2 - <res.	200 - <res.	10 - <res.						
Transverse ridges	-28.833, 84.543	1.3 - 2.8	75-100	5 - <res.	terminal arcuate ridges, transverse to valley	after depositional apron and rim-valleys before FSVs	Figure 5	3.2	**γ**	glacial moraines
	-28.995, 84.648	0.9-2.1	70 - 150	10 - <res.						
Fresh shallow valleys (FSV)	-28.551, 84.462	3.5-15	90 - 300	<res. - 15	highly sinuous, tributary networks	after aprons and transverse ridges, before glacial deflation	Figure 5, 6	3.3	**δ**	proglacial channels
	-28.409, 84.136	6-10	90 - 300	30 - <res.						
	-29.569, 83.116	1 - 10	85 - 275	< HRSC res.						
Broad shallow troughs	-28.514, 84.492	2.5 - 6.5	200 - 350	15 - 25	linear, broad troughs	pre-date FSV	Figure 6	3.3	**ε**	subglacial drainage valleys
	-29.514, 83.109	1 - 1.5	450 - 550	<HRSC res. - 10						
Deeply incised valleys	-29.28, 84.60	7.5-8	1000-2500	100-250	dendritic V and U-shaped rim valleys	more than one activation possible	Figure 3, 12	3.4.1	**ψ**	older fluvial valleys, glacial re-activation
	-29.19, 83.50	20-21	1100-1800	100-300						
	-29.61, 83.68	9-10	500-1100	100-200						
Depositional aprons	-28.7, 84.4	30	N/A	?	conical fan deposits in crater interiors	pre-date FSV and broad shallow troughs	Figure 6, 7, 8, 9, S3, S4	3.4.2	**ζ**	outwash fans and plains
	-29.54, 82.83	10	18000	150-200						
	-28.4, 83.6	8	N/A	50-100						
Basinward scarps	-28.63, 84.45	1-1.5	2/3 crater perimeter	100-150	break in apron slope with appreciable relief	during or after apron emplacement Pre-date troughs and FSV	Figure 7, 8, S3, S4	3.4.2.1	**η**	lake level
	-29.18, 83.71	1-1.5	2/3 crater perimeter	150-200						
	-28.20, 83.42	1-1.2	1/4 crater perimeter	100-150						
Crater wall parallel ridges	-29.77, 83.34	0.6-1.6	100-250	20 to <res.	parallel ridge-trough texture	first oriented ESE, then SSE. Both before LTU	Figure 10	3.4.3	**θ**	glacial striations
	-29.66, 83.47	2-4	150-400	90 to <res.						
	-29.80, 83.44	1-2.2	200-400	10-50						
Crater wall benches	-29.47, 82.90	9-10	300-800	20-50	bench step on crater rims	before depositional aprons, pre and post- wall parallel ridges	Figure 11a, S7a, S8	3.4.4	**κ**	lake level
	-29.74, 83.95	3.5-4	800-1200	80-100						
	-29.7, 83.65	3.5-4	800-1200	100-120						
Pancake deltas	-29.81, 83.47	800-850	1.5-2	10-20	flat-topped fans	after LTU, after/ during shallow depressions	Figure 10	3.4.5	**ι**	sub-ice/ subglacial deltas
	-29.221, 84.54	2.2-2.8	4.5-5	120-150						
Undulating plateaus	-28.66, 84.08	<1	<1 km	40-150	broad ridges, hills and depression	pre-dates FSV, post-dates light toned unit	Figure 9, 10, S6	3.4.6	**ς**	older depositional aprons
	-28.64, 84.32	<1	<1 km	40-150						
	-28.86, 84.36	<1	<1km	40 - 150						

Multiply connected valleys	-29.878, 84.362	10±2	280±70	30 ± 9	complex, anasto-mosing	more than one episode possible	Figure 12, 13	4.1	λ	subglacial channels
	-28.457, 84.908	8±2	190±80	60 to 5 m						
	-28.936, 83.303	0.6±0.3	200±20	<res.						
Discordant valleys	-29.567, 84.421	3±2	500±200	50±20	sinuous, no tributaries	posterior to western uplands fluvial activity	Figure 14	4.2	ν	subglacial channels
	-29.649, 84.145	2.0±1.5	500±200	200 to 10						
	-29.02, 82.941	2±1	250±50	< HRSC res.						
Shallow depressions	-29.248, 84.879	5.7±0.8	4000±200	200±50	irregular, concave, bowl-shaped	pre-date or same as hummocks	Figure 15	4.3	ξ	interlinked subglacial cavities
	-29.45, 84.77	7.0±0.7	5000±300	150±50						
	-28.634, 82.647	1000±50	1030±50	< HRSC res.						
Hummocky material	-29.591, 84.622	0.14±0.01	117 ± 8	20 to <res.	mounds	post- or during linear trough incision	Figure 15, 16	4.4	ο	glaciofluvial hummocks
	-29.461, 84.764	0.11±0.01	102 ± 5							
	-29.976, 84.993	0.11±0.01	137±7							
Linear troughs	-29.891, 84.748	12.3±0.1	300±60	19±6	braided, anasto-mosing, linear	syn- or post-Navua A Valles incision	Figure 16	4.4	π	glaciofluvial hummocky corridors (GHC)
	-29.967, 84.669	8.9±0.1	480±80	12±2						
	-29.917, 84.792	12.7±0.2	500±100	30±10						
Navua A Valles	Up-stream	~ 25	1200-2800	200-250	sinuous, tributary valley. Discontinuous	First stage - Noachian, reactivation Amazonian	Figure 17	4.5	φ	subglacial channel
	Middle	~ 50	700-1500	40 - 70						
	Down-stream	~83	1200-3000	<HRSC res.						
Sinuous ridges	-30.036, 84.747	2.80±1.06	62±4	11±1	linear, no bifurcation, sinuous	post- or during hummock deposition and Navua A Valles activity	Figure 12, 14, 15, 17	4.6	μ	eskers/ inverted channels
	-29.573, 84.388	0.85±0.02	31±7	<res.						
	-29.54, 84.751	1.94±0.09	63±7	~ 2m						
SW broad valleys	-30.80, 82.845	18-20	3500-500	200-400	broad, U-shaped. Inverted topography within	pre-dating light toned unit	Figure 18	4.7	τ	tunnel valleys
	-30.750, 82.952	25-30	3000-4500	200-300						
	-29.0, -82.7	1-20	200-350	<HRSC res.	variable: from	pre-date crater rim valley	Figure 19	4.8	υ	
Western uplands valleys	-28.6, 82.6	5-15	150-350	<HRSC res.	labyrinthine to dendritic	incision, after light-toned unit				subglacial // fluvial channels
	-29.9, 83.3	N/A	150-300	<HRSC res.						

downslope-oriented longitudinal bands, and has a concave and nearly circular planform and a narrow exit that is broadly similar to terrestrial glacial cirques.

3.1.1. Interpretation

Planform morphology, textures indicating downslope viscous deformation, and evidence for deflation are all describing characteristics of Glacial Like Forms (GLFs), that is, debris-rich ice deposits with confirmed ice presence (Holt et al., 2008, Plaut et al., 2008, Souness et al., 2012) but unknown ice concentration, which in larger ice bodies ranges from 20-80% (e.g., Mangold, 2003; Head et al., 2005; Hubbard et al., 2014), and found in the thousands on Mars' midlatitude regions (Souness et al., 2012, Hubbard et al., 2014). Following these guidelines, we interpret these deposits to be GLFs, or modern debris-rich glaciers. The downslope longitudinal bands are consistent with the course of glacial flowlines, and are likely the result of compositional banding caused by englacial and supraglacial sediment accumulation and distribution along flowlines due to internal deformation, followed by downglacial transport, and finally revealed by differential sublimation. Examples of analogue glacial longitudinal banding on terrestrial debris covered glaciers are shown in Fig. S3. At locations designated with green "#" in Fig. 3b the surface features are indistinct, probably because of a cover of mantling material and accumulated particulates from ice sublimation. Similar obscuration occurs on most of the inferred glacial deposits.

Deposit deflation and mass loss are evident from downglacier longitudinal bands disconnection from specific upstream sources in valley-infilling deposits in Nako and Batson craters (see analogue in Fig. S3). Examples of this disconnect are shown in the headwalls of a Nako crater deposit (Fig. 3a, red lines) and in a deposit in Batson crater (Fig. 4c), where longitudinal bands on the depositional aprons at "1" and "3" trace upflow to the low relief ridges at "2" and "4", respectively. These low ridges are unlikely to have been direct sources of glacial ice, but if overtopped by glacial ice sourced from much higher and steeper upstream slopes, the glacier could have flown over them. For ice to override these ridges would have required a former depth more than 50 m above the ridges. A similar situation occurs in Fig. 4d where longitudinal bands at "5" were probably sourced from a higher stand of the present

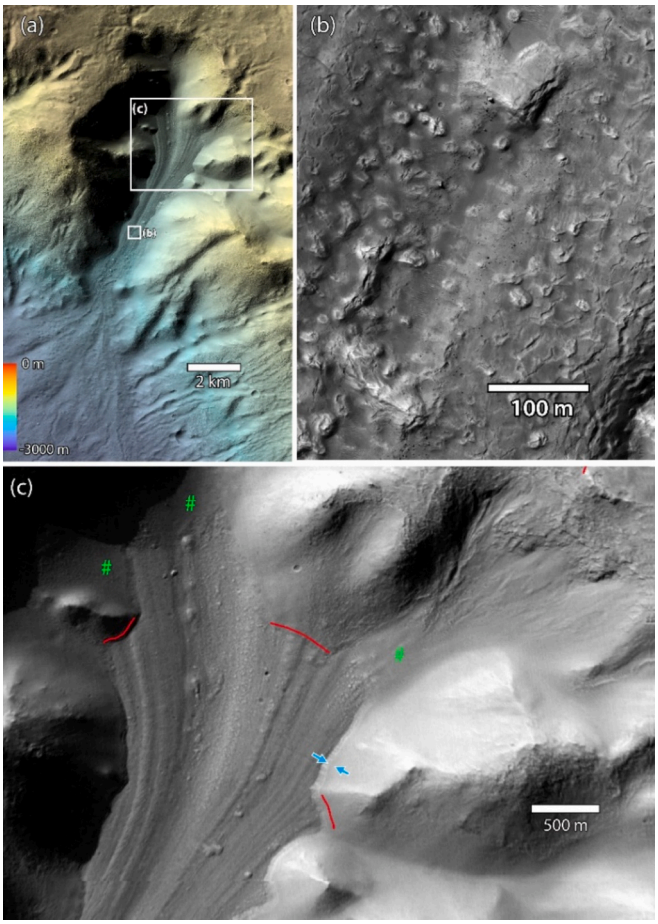

Fig. 3. Debris-covered glacier (GLF) on northeastern rim of Nako crater and surrounding deeply incised valleys. (a) context figure showing the glacier and host valley and fan-like deposit southwest of the glacier. (b) Detail of glacier, showing light-toned appearance of large blocks and rough surface texture. (c) Upper part of the glacier. See text for notations on figure. Image center (a) 83.18°E, 29.45°S. Portions of the glacial surface denoted by "#"s are mantled, whereas katabatic/anabatic wind or reflected solar light from crater walls may keep the downslope portions of the glacier largely mantle-free. The glacial ice has undergone sublimation deflation of at least the depth shown by the band indicated between blue arrows. The red lines show downslope longitudinal bands, aligned following flow streamlines, apparently emerging from mountain slopes but disconnected from localized mass wasting sources, suggesting appreciable past glacial deflation. See sections 3.1 and 3.4.1 for description and interpretation.

glacier than from the basin at "6". The former glacial extent is discussed in more detail in Section 5.

3.1.2. Supraglacial debris

CTX images of glacier surfaces on Nako and Batson crater exhibit clusters of blocky material ranging from the limit of resolution to 250 m in diameter (Figs. 3, 4, 6a, Table 2), distributed forming chains elongated in the inferred direction of downslope glacial flow (Fig. 3) or collected in the cirque-shaped source alcoves into the main glacier trunk (Fig. 4b), protruding well above the glacial surface. Many of the blocks have a distinctive light-toned appearance (Fig. 3b).

3.1.2.1. Interpretation. These observations are consistent with the blocky material being coherent debris masses transported by the glacial flow. The occurrence of substantial debris masses forming elongated trains on inferred glacial deposits has been noted as supraglacial GLF boulder trains (Hubbard et al., 2011, 2014). Previous HiRISE mapping of such blocky deposits by Hubbard et al. (2011, 2014) noted that the debris is formed of boulder-sized material protruding over the host glacier. On a GLF in Protonilus Mensae, supraglacial GLF debris was found to consist of hundreds of individual 1-5 m angular boulders distributed conforming with glacial surface lineations (Hubbard et al., 2011, 2014) and attributed to be wall-rock debris deposited at GLF heads. Fig. 3b exhibits 1-5 m angular boulders of the type noted by Hubbard et al. (2011, 2014), but the majority of the blocks are 10 to >100 m in size, light-toned, and rough-textured with numerous surface fissures. The processes producing the rough texture are undetermined. We interpret that the supraglacial light-toned block clusters are fragments of a decameters-thick layer of light-toned material that was deposited by airfall deposition covering the mapped region at about 1 Ga (Howard et al., 2021) (see Fig. S17). Exposures of this unit on valley walls likely broke off and deposited supraglacial boulders via mass-wasting processes, or else draped an existing glacial surface and were later broken off and transported downflow by glacial deformation. Deflation evidence (Fig. 4), however, indicates that sublimation has removed tens to hundreds of meters of ice from the glacial surfaces, which would leave blocks in positive relief even if they were transported englacially.

3.2. Transverse ridges

Several low, relatively narrow ridges occur within Batson and Jori craters as well as within three D<20 km craters north of McCauley crater (Table 2). They are located near the transition from the interior crater walls and the basin floor, distributed generally aligned perpendicular to the general terrain slope but locally extending upslope along the lower valley wall. The most prominent ridges follow the downslope terminus of the debris-covered glacier extending onto the Batson crater floor from the northeastern crater wall (Fig. 5a, white γ letters). The other major cluster involves curved ridges at the transition from crater wall valleys to the Batson crater floor (Fig. 5b, white and blue γ letters).

3.2.1. Interpretation

A resemblance with terrestrial moraines bounding former mountain glacier extents suggests that these ridges are likely terminal and lateral moraines of the debris-covered rim glaciers. The ridges, however, are narrower than typical terrestrial glacial moraines, suggesting that the martian glaciers have experienced less basal erosion as explained by Grau Galofre et al. (2022). Similar lobate ridges have been noted elsewhere in or bounding glacier-like forms (GLFs), and also are interpreted as moraines (e.g., Hubbard et al., 2011, 2014). These moraines may be deposits pushed by glaciers, or possibly formed by the deposition of passively advected englacial and supraglacial material, similar to cold-based moraines (Head and Marchant, 2003; Hubbard et al., 2011; Parsons et al., 2020).

3.3. Fresh-shallow valleys and broad shallow troughs at glacial termini

A class of shallowly incised, often sinuous valleys has been identified in locations throughout the martian mid-latitudes. They have been termed "fresh shallow valleys", or FSVs (Fassett et al., 2010; Howard and Moore, 2011; Parsons et al., 2013; Hobley et al., 2014; Wilson et al., 2016; Wilson and Howard, 2022). The adjective "fresh" is a designation relative to the comparatively degraded Noachian valley networks of the equatorial cratered uplands. In high-resolution imaging (CTX and limited HiRISE coverage) FSVs are moderately affected by mass wasting and eolian processes. In this study area FSVs are widespread in the interior of all the named craters except McCauley, and they occur locally on the surrounding terrain (Figs. 5, 6, S18b). In Batson and Nako craters all the mapped glacial deposits are associated with FSV systems originating at the inferred glacier terminus. These FSVs cross the broad, gently sloping ramparts mapped as depositional aprons (see section 3.4.2 below). Where the FSVs cross relative depressions they are associated with smooth, sloping deposits. The chains of FSVs originating

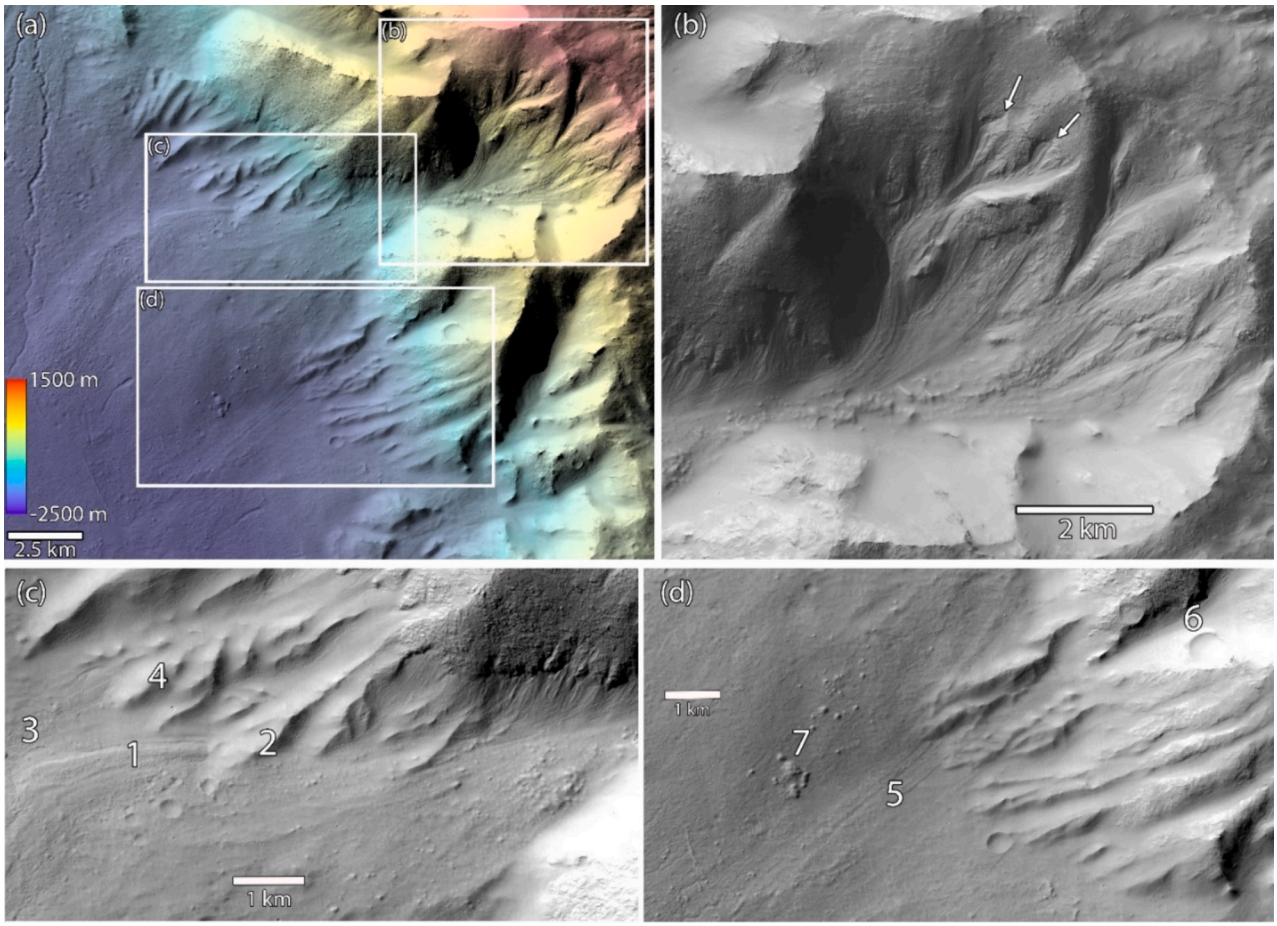

Fig. 4. Glacier on the northeast interior rim of Batson crater. (a) Context image, showing extensive feature interpreted as a piedmont glacier sourced from a cirque-like headwall. Image centered at 84.66°E, 28.75°S (b) Detail of glacial headwall, showing multiple converging downglacier longitudinal bands evocative of flow lines, and large clusters of blocks on the glacial surface in the vicinity of the constricted neck of the glacier. Arrows point to indentations at the headward end of glaciers; (c) At "1" downglacier longitudinal bands appear to emerge from a crater wall ridge at "2". These longitudinal bands indicate sublimation deflation of the glacier by >50 m required for glacial flow to have surmounted the up-flow ridges at 2 and 4. (d) Longitudinal bands at "5" likewise appear from valley wall ridges and are not aligned with crater wall valley incisions at "6". Note extensive clusters of blocks at "7" up to 250 m in diameter. See section 3.1 for interpretation.

from the glaciers on the north interior rim of Batson crater can be traced more than 30 km across the depositional aprons to the low-elevation southern floor of the crater.

Fig. 6a illustrates the down-valley transition from a glacier in northeast Batson crater to FSVs. The current apparent terminus of the glacier is about at "&", with FSVs "δ" initiating and extending downstream. Fig. 6a also shows broad, linear or subtly curved broad shallow troughs radiating downslope from the glacial terminus ("ε", Table 2). These troughs appear more degraded than the FSVs, and are in instances superposed by them, indicating they are most likely older (Fig. 6a, left). The terminus of the glacier in northeast Nako crater presents a similar set of landforms (Fig. 6b). Below the glacial terminus ("&"), we observe similar broad shallow troughs ("ε") as well as a series of narrow ridges ("ω"), which fan out downslope to the edge of an elevated sloping platform (*). FSVs initiate at the base of this platform ("δ") and extend into the crater interior.

3.3.1. Interpretation

Following previous interpretations (i.e., Fassett et al., 2010) we infer that FSVs in this location are proglacial meltwater streams fed by the upslope glaciers, based upon their abrupt sourcing at the glacial margin. The water source for martian FSVs has generally been attributed to snowmelt runoff, but the FSVs radiating from inferred glacier termini (Fig. 6) are likely formed by glacial meltwater. Within this region FSVs not associated with mapped glaciers usually originate from crater wall valleys or other uplands that would have been likely locations for glacial ice accumulation as well. If the depositional aprons into which the FSVs are incised were ice-rich, sinuosity development may have occurred due to turbulent melt processes (Parker, 1975; Karlstrom et al., 2013; Mantelli et al., 2015).

We suggest that the broad shallow troughs shown by "ε"s in Figs. 6a, b may have been subglacial drainageways eroded when the glacier previously extended further downslope across the depositional apron. This deviates from previous interpretations of broad troughs incising crater alluvial fans, which favored late-stage fluvial incision (Anderson et al., 2023). However, we favor the glaciofluvial hypothesis because late-stage fluvial incision does not explain the abrupt upstream terminus of the troughs nor the spatial and directional association with glaciers. Following this line of interpretation and by association with the terminus of the glacier, we suggest that the narrow ridges are candidate eskers, acknowledging that in this context they could also be the result of relief inversion following differential erosion of channel deposits on the host depositional apron, following glacial retreat.

For the case of the FSVs in Fig. 6b, we suggest that at the time of the formation of the FSVs by glacial meltwater the glacier extended to about the edge of the platform marked by "*" symbols, the sinuous ridges ("ω"s) are candidate eskers, and the broad depressions may have been subglacial drainageways. This spatial and temporal sequence of events is consistent with those observed in terrestrial land-terminating proglacial systems, where the terminal portion of a glacier or debris-covered

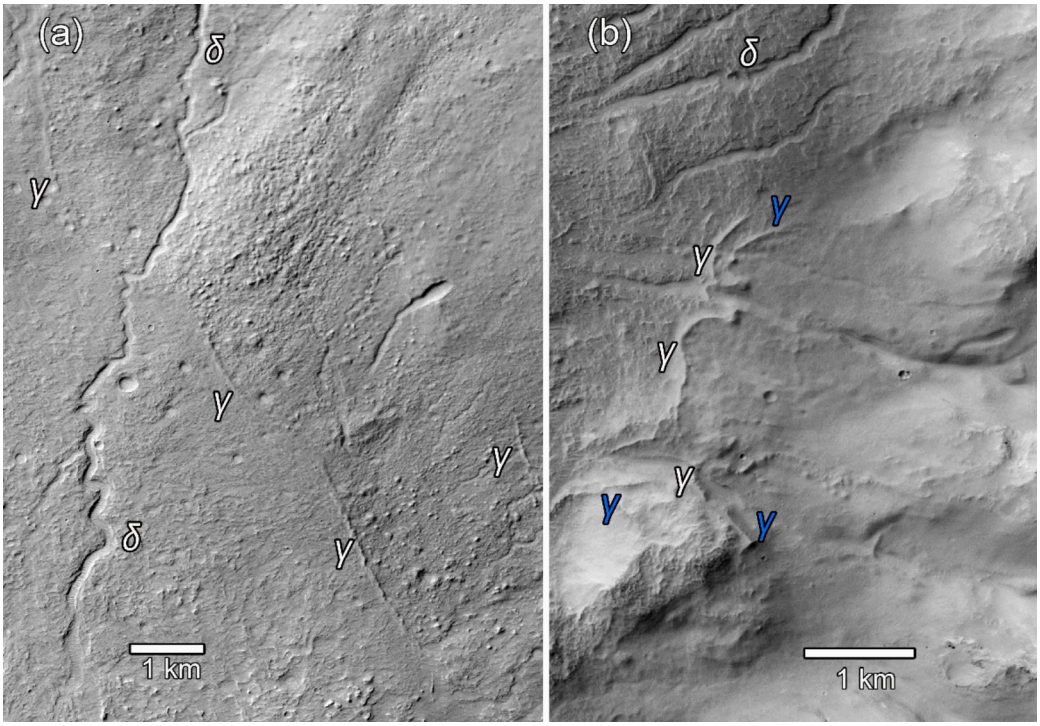

Fig. 5. CTX images of ridges generally perpendicular to local terrain gradient (white 'γ' in (a) and (b)) interpreted to be glacial terminal or recessional moraines. (a) Transverse ridges at the distal end of the glacier shown in Fig. 4. Image centered at 84.53°E, 29.79°S. (b) Transverse ridges at the mouth of west-sloping valleys on the southeastern interior walls of Batson crater. Some ridges (blue γ letters) bend up-valley above the valley floor and may be lateral moraines. See Section 3.2 for discussion. Image centered at 84.67°E, 29.00°S. Fresh-shallow valleys indicated by "*δ*".

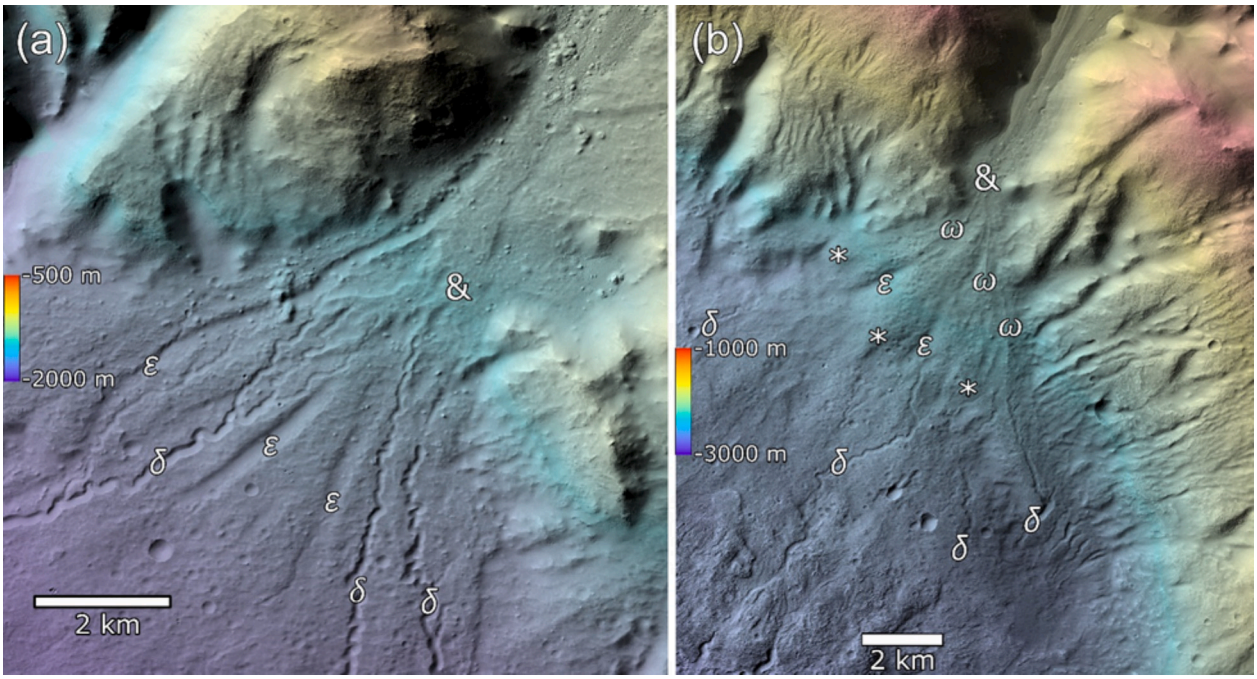

Fig. 6. Inferred glacier distal ends and fresh shallow valleys (FSVs). (a) FSVs ("*δ*"s) on the eastern north interior wall of Batson crater, which originate at the glacial terminus (marked "&") and incise over a depositional apron. Shallow troughs oriented downslope "*ε*"s also incise the depositional apron. Supraglacial block clusters extend down-glacier onto the depositional apron. (b) FSVs ("*δ*"s) on the northeastern floor of Nako crater extending from the glacier at upper right (see Fig. 3) onto a depositional apron. Upstream, FSV transition to inverted distributary channels ("*ω*"s) that originate at the inferred glacial terminus "&". The transition, marked "*", lies on a shallow, rounded scarp on the depositional apron. See Sections 3.1, 3.3, 3.4.2 for details and interpretation. Image centers: (a) 84.49°E, 28.34°S; (b) 83.14°E, 29.54°S.

glacier lies on a glaciogenic sedimentary platform, where eskers and other elements of the subglacial drainage system are distributed (Fig. 6). Beyond the sedimentary platform, moraines ('transverse ridges', Fig. 5b) may or may not be observed, to be followed in sequence with the elements of the proglacial system: outwash fan sedimentary deposits incised by proglacial channels, with possible supraglacial sedimentary deposits on the outwash plain. This sequence is illustrated by analogue sites on Earth including the Finsterwalderbreen and Vestre Lovénbreen glacier termini, Svalbard.

3.4. Crater interior wall and floor morphology

3.4.1. Deeply incised valleys

All the depositional aprons radiate from deep valleys incised into the crater walls, with apron volume and source valley incision volume roughly comparable. The degree of crater wall incision generally correlates with the interior crater relief. The depth and density of valley incision exhibits a strong asymmetry in Batson, Salkhad, and Nako craters, such that south-facing interior rims are incised to a much greater extent than north-facing rims (Figs. 1, 8, 20). Either or both relief and climatological factors might contribute to this pattern. The southern sections of the rims of these craters have lower relief relative to the north rims. Jori crater incision is greatest on the southeastern crater interior wall where the relief is enhanced due to superposition of Batson and Jori crater rims. McCauley crater has only modest rim incision, however, despite the relief of the northern rim equaling or exceeding that of the north walls of Batson, Nako, and Salkhad craters. Rim orientation, rim relief, orbital parameters such as obliquity, and latitude, all play a role in determining solar insolation conditions, which may enhance ice and snow melt on south-facing slopes and facilitate erosive activity in the Amazonian. South-facing crater walls receive less mean solar radiation, so that snow and ice accumulations are less subject to solar-induced sublimation.

Several of the deep valleys host small extant glaciers (Figs. 3, 5, 6) and others are interpreted to retain ice beneath thick mantles. The deeply incised valleys morphologically resemble crater wall valleys hosting alluvial fans in the martial equatorial latitude (Moore and Howard, 2005; Wilson et al., 2021; Morgan et al., 2022). Additionally, rim relief has been identified as contributing factor to the incision of valley walls creating alluvial fans (Moore and Howard, 2005, Wilson et al., 2021, Morgan et al., 2022), likely because of a greater surface area for snow and ice accumulation on longer slopes. The discussion below addresses the question of the relative contribution and timing of valley incision and depositional apron deposition by fluvial and glacial processes.

The valley sidewalls are dominantly relatively planar and only locally display cliffs or steep benches that would suggest rock outcrops. One exception occurs on the steep headwall of the large glacier on the northeastern wall of Batson crater (Fig. 4b). We measured the gradients from crest to floor of 20 sideslopes of valleys incised into the northern interior rim of Batson crater using the stereo CTX DTM. Gradients ranged from 16-47°, averaging 22.8°. Only one profile exceeded 29°.

3.4.1.1. Interpretation. Deeply incised valleys in crater walls could have been eroded primarily by antecedent or interglacial fluvial processes under an apparently warmer climate, or by formerly more extensive glaciers with low lateral erosion rates, or both. Terrestrial valleys formerly occupied by glaciers typically exhibit U-shaped cross-sections, irregular profiles due to differential scour, lateral and terminal moraines, and steep headwalls of cirques and arêtes. The high-relief, rounded headwall of the glacier occupying the eastern interior wall of Batson crater indents the crater walls in a cirque-like planform but lacks steep headwalls (Fig. 4b). One explanation for the lack of steep headwalls and U-shaped valleys might be that martian valley glaciers have little erosive capability when compared to Earth, even if warm-based (Grau Galofre et al., 2022). Over long timescales, however, glacial erosion by warm or cold-based ice deposits could lead to crater wall rock erosion (Atkins, 2013; Grau Galofre et al., 2022), particularly on steep crater walls. Some capacity for glacial flow to be erosive is indeed shown by the low scarps at the headwall termination of flows (e.g., at arrows in Fig. 4b).

Terrestrial mountain glaciers typically incise sideways as well as downwards into dense crystalline or indurated sedimentary rocks, producing and supporting U-shaped valleys with steep or near vertical side walls. However, crater walls would typically be highly fractured due to impact stresses, as observed in terrestrial craters (Osinski et al., 2005). In addition, as pointed out by Rodriguez et al. (2020) the deposits comprising the bulk of the martian highlands may be composed of fine, relatively unconsolidated sediment. If so, this supports the possibility that many of the deeply incised crater wall valleys studied here have been at least partially excavated by present or former glaciers with low lateral erosion rates, encased within valleys with low potential for stability of U-shaped walls. This is further supported by the presence of transverse ridges at the termination of some dendritic, V-shaped valleys, which host remaining ice deposits (Fig. 5b). A lack of strong bedrock in the crater walls would result in rapid mass-wasting to and below angle-of-repose gradients following loss of glacial ice filling valleys, as indicated by the 22.8° average of measured valley sidewalls. Perron et al. (2003) measured debris slope gradients on martian debris slopes and found averages ~20°, well below angle of repose values (~35°); they attributed the low gradients to creep induced by repeated deposition and sublimation of ground ice. Mass wasting following sublimation and melting of formerly deeper glaciers occupying the valleys could account for the lack of identifiable trim lines. The lesser scour potential of martian glaciers vis-à-vis terrestrial glaciers and the enhanced role of erosion by subglacial drainage (Grau Galofre et al., 2022) also may explain the paucity of moraines and the lack of irregular profiles characteristic of many terrestrial valley glaciers.

Fig. 7d shows a valley system in Svalbard, Norway where glacier-occupied divides feature cirques (*c* symbols), but inferred deglaciated former glacial cirques downvalley (*c'*) have been dissected by weathering, mass-wasting, and fluvial dissection. The processes modifying deglaciated valley slopes include rockfalls, small avalanches, and deposition of small fans at the base of slopes (e.g., Ballantyne, 2002, Berthling et al., 2020, de Haas et al., 2015, Hauber et al., 2011). The lithology in the region of Fig. 7d is slightly deformed Devonian sandstone (Elvevold et al., 2007), which may explain the extensive post-glacial modification of the glacial valleys.

3.4.2. Depositional aprons

Jori, Batson, Nako and to a lesser extent Salkhad craters feature large fan-like deposits with gentle surface slopes (<4°) extending partway onto the northern crater floor, largely sourced from the heavily dissected portions of the host crater northern walls. We term these "depositional aprons". They may contain an uncertain proportion of detrital and ice-rich deposits supplied from upslope crater walls and valleys (Table 2). Depositional aprons are converging conical sedimentary deposits sloping about 2° to >4° from sources at major crater wall valleys (Figs. 5, 6, 7, S4, S18 and Tables 2 and 3).

Batson crater features a large depositional apron covering ~2/3 of the crater floor, including most of the crater northern, eastern, and western floor. Nako and Salkhad craters feature smaller depositional aprons than Batson crater, both in size and proportion, and are also primarily sourced from the northern crater rims. Jori crater has a prominent depositional apron on the east side of the crater interior and smaller units on the north and south basin margins (Fig. 11). McCauley has comparatively small depositional aprons, the largest being sourced from the northwestern crater rim. Fig. 7d shows outwash deposits "ζ" sourced from glaciers in the head of a valley in northern Svalbard that are a partial analog to depositional aprons in Batson crater.

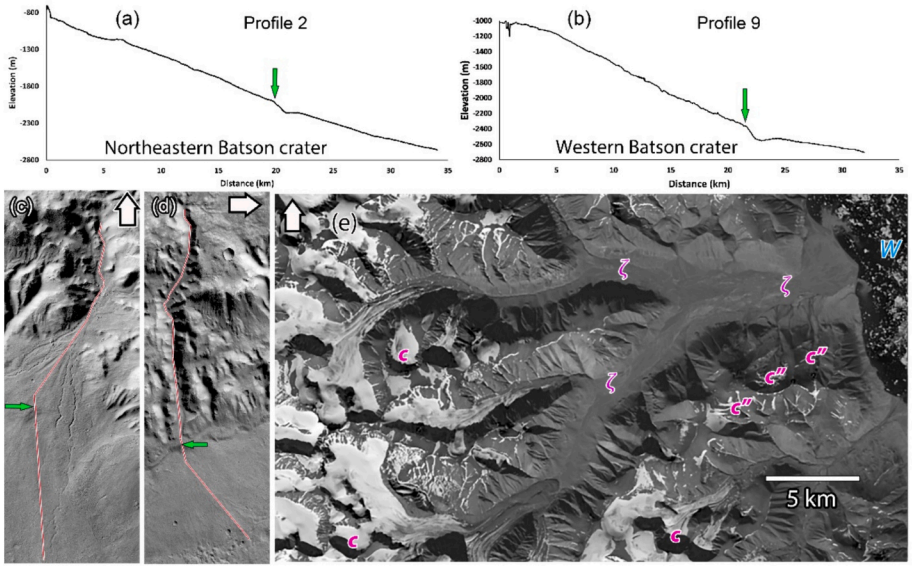

Fig. 7. Example profiles across glaciers and depositional aprons, showing scarps (green arrows mark upper edge of scarps). Note slight depressions at foot of scarps. Location of profiles are shown in Fig. S3 and additional profiles are in Fig. S4. (a) Profile across northeastern Batson crater. Scarp break (green arrow) at 84.45°E, 28.63°S. Upper third of profile follows extant glacier. (b) profile in western Batson crater. Scarp break at 83.71°E, 29.18°S. (c) Trace of profile 2. (d) Trace of profile 9. Thick arrows in (c) and (d) point north. (e) Landsat 8 image of an analogue glacial outwash sequence found in a proglacial environment in Svalbard, Norway (15.0°W, 79.3°N). Moving downflow from the mountains, glaciers terminate in the valleys, leading to outwash sediment and debris deposition and proglacial meltwater channel development on the outwash (plain and fan) '*ζ*', depositing into '*W*', an inlet of the North Atlantic Ocean with scattered float ice. Several cirques retaining ice are labeled with *c*, whereas *c''* are inferred to be former cirques modified by weathering, mass wasting, and fluvial dissection. The outwash plain is labeled "ζ". See sections 3.1 and 3.4.2 for details and interpretation.

Table 3
Relief characteristics of depositional aprons. Slopes are in degrees. See Fig. S4 for profile locations and Fig. S5 for graphical profiles.

Profile Number	Crater	Upper Profile Slope[1] (°)	Scarp Height (m)	Maximum Scarp Slope (°)	Lower Apron Slope[1] (°)
1	Batson	23.6, 9.0, 4.3	—	—	—
2	Batson	3.8, 3.5	180	10.2	2.8, 1.9
3	Batson	3.9, 3.0	205	8.4	1.6
4	Batson	3.0	112	7.0	1.3
5	Batson	4.3	102	8.9	2.0, 1.1
5.5	Batson	3.0	134	10.2	2.3
6	Batson	3.7	131	9.5	2.0
7	Batson	4.0	107	13.9	0.4
8	Batson	7.2, 1.8	74	17.0	3.9
9	Batson	4.1	189	12.1	1.5
10	Nako	4.5, 0.9	140	9.4	—
11	Nako	4.0, 1.6	—	—	—
12	Jori	3.6, 2.9	112	7.1	—
13	Jori	3.0	131	11.0	—

[1] Where multiple values are given the profile contains a break in slope. Lower apron slope refers to portions of aprons below a scarp, where present. Upper apron slopes extend from the upslope start of the profile to the scarp crest, except that steep valley head slopes are not included in tabulated values.

3.4.2.1. Basinward scarps. Enigmatic features of the depositional aprons in Batson, Jori, Nako and possibly Salkhad crater are prominent circumferential basin-center-facing scarps situated partway downgradient from the source basins of the depositional aprons (Fig. 7, 8, S18). In Batson and Nako craters these scarps clearly define an upper and lower apron, with markedly different surface slopes (~3.9° versus ~1.9°, respectively, Table 3). Fourteen topographic profiles were collected along headwater valleys and crossing depositional aprons in Batson, Nako, and Jori craters: Their relief characteristics are summarized in Table 3 (see Fig. S4, S5 for locations).

The mapped profiles above the scarps include both the valley floors (including the mapped glaciers) and the aprons. Excepting profile 8, the profiles do not have a break in slope at the apex of the aprons and have low concavity. Scarp break appearance ranges from convex and rounded in northern Batson crater and northwestern Nako crater to steeper in the west side of Batson crater. Relief drop, measured from upper break in slope to base, ranges from 74 m to 205 m (Table 2). In many locations around the base of the scarps shallow depressions are present up to 1 km in width (e.g., Fig. 7). Many of these are just depressed relative to the overall basin slope, but several are true enclosed depressions (e.g., Profiles 2 and 9, Fig. 7). Interior scarps of the type discussed here are seemingly rare in martian craters.

Basinward-facing scarps in Batson crater can be traced nearly continuously around about two-thirds of the basin circumference (Fig. 8). The elevation of the upper scarp break is not constant, however, being up to 600 m higher along the northern portions of the basin than along the southwestern and eastern parts of the basin perimeter (Fig. 8). This observation places considerable constraints on the possible origin of the scarps, as discussed in section *5.1.2*.

3.4.2.2. Apron stratigraphy. Informative stratigraphic exposures are rare on the upper depositional aprons, including a lack of clear layering where FSV has incised the apron (Fig. 9a), and minimal evidence at the scarps (Fig. 9b). The surface on the upper apron is rough, with significant eolian cover in relative depressions and transverse eolian ridges forming low crests (Fig. 9a). A 1.5 km diameter crater on the upper depositional apron of Batson crater contains layering partly concealed by eolian infill (Fig. S7). The layering appears to be subparallel with only scattered meter-scale gravel content, and with no obvious channel deposits except for shallow unconformities that occur in the upper layers at the north end of the crater near the entry of an FSV channel. No obvious sublimation texturing of the exposures is present.

Boulders and blocky material like those identified as supraglacial debris extend beyond the mapped glaciers into the interior of the 5 craters, with their farthest extent indicated by red stars in Fig. S4. In Batson crater the blocks extend to the edge of the mapped scarps, with some occurrences in the shallow depressions fronting the scarps and on

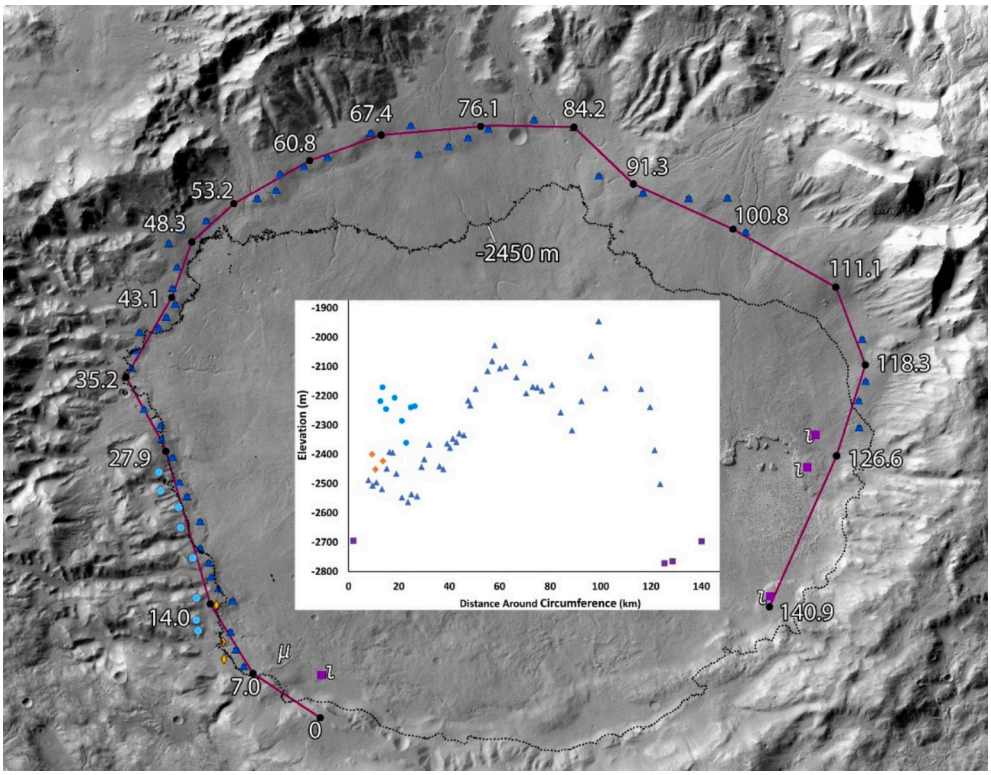

Fig. 8. Elevations of the crests of inward-facing scarps on the depositional apron on the floor of Batson crater. Numbers refer to clockwise distance (in km) around the perimeter of the crater floor clockwise along the purple line. Dark blue triangles denote scarp crests. Orange diamonds are slightly higher secondary crests. Light blue circles are the crests of higher, dissected benches. Purple squares identified by "*ι*"s are low, flat-surfaced depositional benches that share a morphology with interpreted fan-deltas (Zhang et al., 2023). A prominent sinuous ridge on the crater floor is marked by "*μ*". The -2450 m contour roughly corresponds to the top of the scarps along the western crater floor but diverges to the north. See section 3.4.2 for details and interpretation. See Fig. 1 for context.

low benches on the south interior wall. In Nako and Jori craters the blocky material is limited to the upper parts of the depositional apron close to source valley terminus.

3.4.2.3. Interpretation. We interpret the depositional aprons to be sediment deposits, perhaps locally ice-rich, sourced from the erosion of the deep valleys incising the crater rims. The areal extent of the aprons is approximately proportional to the extent of crater wall valley incision, although quantitative assessment of depositional apron volume cannot be made because of uncertain apron thickness. Previous studies interpreted the Batson crater depositional aprons as alluvial fans because of their position downgradient from incised crater wall valleys and sparse ridges locally branching downslope (Fig. S18a) (Moore and Howard, 2005; Wilson et al., 2021; Morgan et al., 2022; and Zhang et al., 2023). However, many of the deeper valleys that fed sediment to the depositional aprons in Batson and Nako craters contain glaciers that were formerly deeper and more extensive (section 3.1), and which could have been erosive, contributing to the deepening and widening of occupied rim valleys. FSV flowing out inferred glacier terminus (Fig. 6) seem to indicate that glacial melt led to the formation of proglacial meltwater streams acting to incise and deposit beyond the glacial margin, although the most recent proglacial activity likely occurred after the emplacement of the aprons.

Therefore, depositional aprons could be of glaciogenic origin, such as terrestrial outwash fans (Fig. 7d), perhaps ice rich, or they could correspond to the deposition as alluvial fans pre-dating glaciation (Section 3.4.1). As previously noted, however, the source of runoff excavating the crater walls and depositing the numerous Hesperian and Amazonian martian alluvial fans is generally attributed to meltwater from snow and ice accumulated in the incised valleys. Because of the spatial association with deeply incised valleys that often display broad or U-shaped cross-sections, characterized by circular headwalls and generally straight thalwegs, some of them currently occupied by glacier deposits, we tend to favor the interpretation of depositional aprons as outwash fans, perhaps ice-rich. We find analogue depositional aprons related to glacial and glaciofluvial activity in polythermal ice caps and plateau glaciers punctured by glacial outlets and hanging glaciers, depositing large sedimentary cones at their foot. Examples of these are found in the Dry Valleys, near the Haughton impact structure on Devon Island, as well as fans below Svalbard glaciers (Fig. 7d).

Depositional aprons are dated using crater counting techniques: Nako crater's apron formed first (1.4-1.05 Gya), followed by Batson crater's (900-1020 Mya), and Jori crater's 680-540 Mya (see Table 5, Fig. S15 and S16). They are genetically related to rim valley incision, and they pre-date FSV and associated inferred fluvioglacial activity. Fig. S13 shows depressions on the upper depositional aprons of Nako and Batson crater that might be related to significant embedded ice. The depressions may either be examples of craters expanded by sublimation (Dundas et al., 2015; Viola et al., 2015) or melting of subsurface ice, as has occurred in floor deposits in Jori crater (Levy et al., 2017).

The features of the depositional aprons that distinguish them from terrestrial and martian alluvial fans are the basinward-facing scarps in Batson, Nako, Salkhad, and Jori. The upper depositional aprons and the associated scarps are unlikely to have resulted from renewed, but areally-restricted subaerial alluvial fan activity. Discharges and sediment delivery from upstream valleys are unlikely to have been so regular as to consistently terminate at a specific distance from the source in a manner that could create terminal scarps 70-200 m high. Higher discharge events would have incised the scarps in the manner that FSVs have incised the scarps that they cross (Fig. S18b).

The observation that most of the profiles of depositional aprons above the basinward-facing scarps in Batson crater intersect the lower

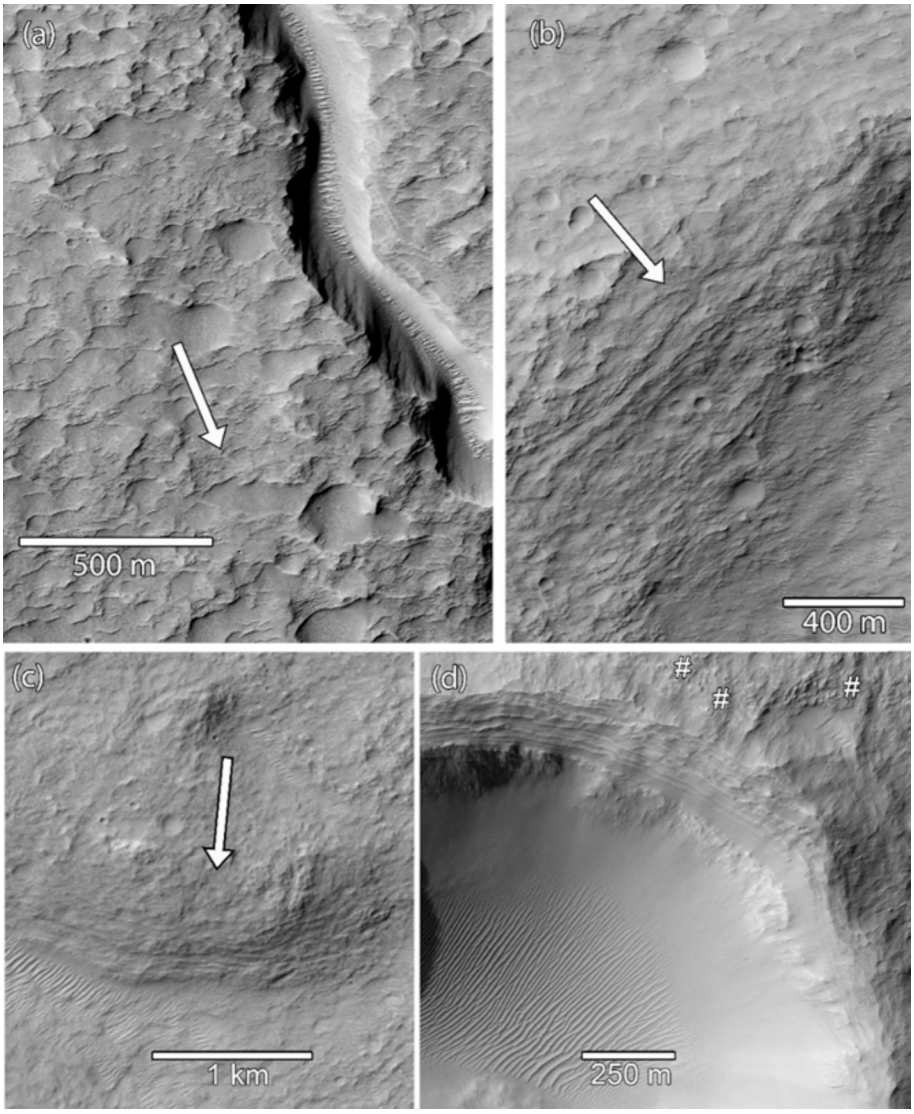

Fig. 9. Banding and surface texture of exposures on depositional aprons and undulating plateaus in HiRISE images of Batson crater floor. (a) Rough surface texture with eolian covering of depressions and degraded small craters on a scarp in depositional apron deposits. The image includes a fresh shallow valley. (b) Contour-parallel ridges and depressions on the face of a depositional apron scarp in Batson crater that may reflect internal layering. (c) Contour-following banding in undulating plateaus surrounding the Batson crater central peak. (d) Layering exposed on the upper interior rim of a 2.2 km crater superimposed on undulating plateau in Batson crater. Light-toned deposits mantle the ejecta at "#"s. Arrows in (a), (b), and (c) point downslope. See Section 3.4.2.2 for details and interpretation (a-b) and 3.4.6 for (c) and (d). Image centers: (a) 84.077°E, 28.659°S; (b) 84.323°E, 28.643°S; (c) 84.357°E, 28.858°S; (d) 84.203°E, 28.856°S. North is up.

aprons within 3 km of the scarp crest (Fig. S5) suggests that the process forming the scarps has been a relatively moderate perturbation of a dominant process of fluvial transport and deposition of the sediment eroded from the deeply incised crater rim as a basin floor bajada, possibly also sourced from glacial runoff. These relationships also suggest that the scarps have been formed at a late stage in evolution of the depositional aprons.

We examine three additional possible origins of the upper depositional aprons and associated scarps: subsurface structural deformation, alluvial fan, deltaic, or glacial activity impinging on interior basin lakes, or a primary origin as the terminal ends of glaciers.

3.4.3. *Structural deformation*

Most of the scarps present a subdued appearance, with rounded lips and maximum slopes less than 15°. The presence of relative depressions fronting the scarps (profiles in Fig. 7) suggests downwarping. Most of the scarps in the crater basins lack traces of movement along fractures and are not strongly linear in planview, disfavoring a structural origin. The depositional platform on the east side of Jori crater, however, exhibits shallow, scarp-parallel depressions at 0.5 and 1.0 km upslope from the scarp face that could reflect large incipient slumps. If slumping were the primary mechanism forming the scarps, considerable smoothing and degradation of scarp morphology would have had to occur after the ~0.95 to 1.3 Ga age surface age of the depositional aprons (Howard et al., 2021). The scarp-parallel depressions in Jori crater may be a special case, because the floor of Jori crater features appreciable distortion and slumping of the crater floor, possibly as result of a thermal anomaly partially melting a thick ice deposit within the crater (Levy et al., 2017).

3.4.3.1. Deposition against a lateral barrier. Here we consider whether a now absent lateral barrier might have limited the extent of basinward transport of deposits originating from the crater walls. The most likely barrier would be lakes within the basin, either open-water or ice-covered. Terrestrial deltas are a logical analog, with the depositional apron upslope from the scarp being topset beds and the scarp as a

lakeward-migrating foreset/ bottomset complex. Such an origin has been suggested for the upper aprons in Batson and Nako craters (Zhang et al., 2023). In several locations the scarp fronts in Batson crater bow outward toward the basin interior below the major valleys debouching from the rim (Fig. 8), supporting a deltaic interpretation. No shoreline-related landforms, such as barrier spits and beach deposits, have been identified. Such features are inhibited, however, when the lakes are frozen due to inhibition of wave action. This explanation does not address the origin of the relative and absolute depressions basinward of the scarps where bottomset deposits might be expected.

Support for former interior lakes occurs as scarp-fronted, "pancake" fluvial deposits around the margins of Batson, Nako, Salkhad, and McCauley craters as well as other low-elevation flat surfaces around the basin interiors, as shown in Figs. 8, 11b, 11d, and 12a. These were proposed as defining former lakes within these craters by Hargitai et al. (2018b) and Zhang et al. (2023).

An inference of interior basin lakes would be bolstered to the degree that scarp rims define a common elevation. As shown in Fig. 8, however, the prominent scarps in Batson crater vary in elevation by about 600 m, which could result from temporally varying lake levels and associated deposition at the lake boundaries. Degraded higher benches on the southwestern interior of Batson crater are within the same range of elevations (-2100 to -2300) as the benches on the northern interior (light blue dots in Fig. 8).

A past filling of the interior of the mapped craters with a thick ice cover, but with deposition occurring below an areally-varying ice thickness could account for the variation in scarp elevations around Batson crater, as discussed in Section 5.3. Similarly, a more level infilling but temporally declining ice surface elevation and asynchronous scarp development could account for the varying scarp elevations. The lower scarps on the southeastern portion of the Batson crater floor (Scarps 6-9 in Fig. S4 and kilometers 0-50 in Fig. 8) are somewhat steeper and less degraded than the scarps on the north side (Scarps 2-5 in Fig. S4 and kilometers 55-100 in Fig. 8), possibly indicating a younger age. Ice or lakes occupying the interior of Batson crater and serving as lateral constraints for scarp formation would have had to subsequently disappear with minimal alteration of the crater floor. Such ice, however, would have likely had much less detrital components than the glaciers and sediment sourced from the valleys incising the crater wall. Overall, we disfavor the asynchronous explanation because of the lateral continuity of scarps around the western and northern circumference of Batson crater (Fig. 8) and a lack of an identified climatic scenario temporally shifting glacial activity from the north to the west crater rim.

3.4.3.2. - Scarps as paleoglacial deposits. The scarps could mark the farthest advance of glacial ice into the interior of the 5 craters. There is indication that the glaciers once extended farther into the interior than as mapped. Collections of blocky material like those that are ubiquitous on the mapped glaciers extend beyond the mapped glaciers into the interior of the 5 craters, extending to the limit of the scarps. As discussed above these blocks are likely large fragments of the light-toned deposit and crater wall rock material transported by the glaciers.

The pattern of blocky material strongly suggests that glaciers in Batson crater formerly extended to the depositional apron scarps. The same is likely true for glaciers in Nako and Jori craters. This leads to the question whether the upper depositional aprons in these craters are largely composed of glacial ice or whether the former glaciers have mostly been depleted by sublimation. If largely composed of glacial ice the glaciers would have to have been thicker than 100-200 m to account for the scarp relief. As noted, exposed layering is sparse and inconclusive as to deposit stratigraphy. The relatively steep scarp fronts (>7°, Table 3) argues against a largely ice composition of the sub-apron deposits. If the scarps are largely composed of fluvial deposits, then the former presence of a lateral barrier is required, probably as a high lake level. If the aprons are mostly composed of glacial ice, a concomitant central basin infilling with ice or an ice-covered lake is compatible, if perhaps not necessary.

The origin and process significance of the numerous shallow depressions that border the basinward edge of the depositional apron scarps remains enigmatic. We entertain three possibilities: 1) downwarping because of the weight of deposits upslope from the scarp; 2) erosion by katabatic wind, either by direct traction scour or indirectly through sublimation (as occurs in the north polar cap scarps (Howard, 1978, 2000, Smith et al., 2013, Spiga and Smith, 2018), or 3) a near-shore process associated with the former presence of ice-covered lakes associated with the scarps. The latter explanation might be most possible if the paleolakes supported a deep ice cover, perhaps promoting scour by subglacial drainage into the lakes, as discussed in Section *5.3.2*.

In summary, the depositional apron scarps had been previously interpreted as fan-deltas (Zhang et al., 2023), but the scarp elevations vary around the periphery of Batson crater. Our interpretation suggests that the scarps formed near the contact between glaciers on the crater walls and perennially ice-covered lakes in the crater interior. This interpretation is based in part on the unlikelihood of unfrozen lakes during the Amazonian period.

3.4.4. Parallel ridges and valleys on crater walls and floors

The western interior rim of Salkhad crater (Fig. 10a) displays numerous parallel ridges and troughs that generally initiate about 100-200 m below the rim and continue to the crater floor oriented roughly downslope (slope ~ 10°), laterally spaced between 100-250 m. On the crater wall the ridges are narrow and sharply defined, and the troughs are broadly concave but filled to an uncertain depth with eolian deposits (see Table 2 for scales), whereas certain troughs ("3") appear enlarged by crater rim-crossing channelized erosion. Parallel ridge and valley alignments similar to those on the Salkhad crater wall are present on the interior crater walls at the north of Nako crater, the northeast of Nako crater (e.g. right side of Fig. 6b), and less distinctly at the north and east of Salkhad crater and the west of Nako crater.

At the base of the crater floor we observe prominent narrow parallel ridges, with terminations marked in Fig. 10b by "*"s (Table 2). Not all the crater-floor ridges can be directly traced to those on the crater rim although they have the same orientation. Between locations "1" and "2" in Fig. 10a, the ridges and troughs on the crater rim are nearly parallel in orientation broadly facing ESE. Near "2" their orientation is about 30°-45° counterclockwise divergent from the general downgradient direction (Fig. 10c). Between "2" and "3" the orientation of the ridges and troughs changes abruptly from ESE to SSE, about a 60° shift in orientation.

3.4.4.1. Interpretation. We interpret that the channels and ridges on the crater walls in Salkhad crater and the adjacent ridges on the crater floor (Fig. 10, Fig. S8) to be the result of subglacial modification by glaciers extending from the rim to at least the basinward terminus of the ridges indicated by "*" in Fig. 10b. The steep gradient of the inner crater wall implies both direct glacial scour and subglacial runoff as possible mechanisms for creating the ridge and trough topography. The deviation of the channels and ridges from orientation directly downslope and the abrupt change of direction between "2" and "3" in Fig. 10a is possibly due to a change in ice flow direction through time. The ridges extending from the base of the inner crater wall marked by "*"s in Fig. 10b are likely constructional, although we cannot rule out erosive or structural influences. The glacial activity in this location appears to pre-date deposition of the light-toned deposit mantling this location and the topography was not subsequently reworked (Howard et al., 2021). The parallel ridges and grooves elsewhere in the study area were likely also sculpted by glacial activity.

3.4.5. Crater wall benches and associated crater floor features

Narrow topographic benches occur along the lower interior crater

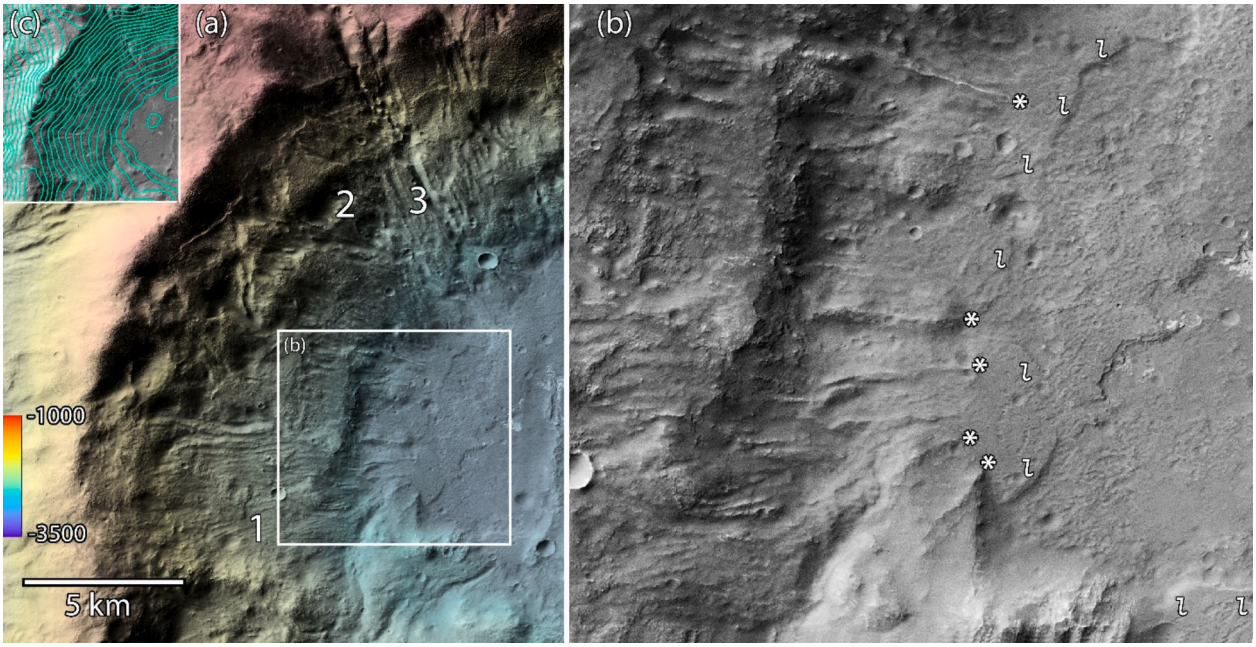

Fig. 10. Western interior crater wall of Salkhad crater showing crater wall parallel ridges (see also Fig. S8), north is up, total relief is 1950 m. (a) Overview. See Section 3.4.3 for descriptions of crater wall ridges, marked by numbers. Image centered at 83.34°E, 29.77°S. Inset (c) shows 100 m contours from the global MOLA DTM. Box shows location of (b). (b) Detail showing parallel ridges on the crater floor, with basin-ward ends of several ridges indicated by "*". Letters "ι" mark the basinward edges of features interpreted as pancake deltas. (c) Inset showing 100 m contours from the global MOLA DTM over region in (a).

walls of the north side of Nako (Fig. 11) and Salkhad (Table 2, Fig. S8) craters. These differ from the depositional apron scarps discussed above because they directly butt against the steep lower interior crater walls, defining a nearly level surface (Fig. 11a). Fig. 11 shows the interior of Nako crater and its crater wall bench (white arrows in Fig. 11b) in the context of all other landforms discussed to this point. Multiple narrow sinuous ridges ("μ"s Fig. 11, 12a) are present on the southern and southwestern Nako crater floor below the -2600 m level, sourced from superjacent interior crater rim valleys. The aligned ridges on the northeast crater floor below the -2600 m contour are interpreted to be Batson crater ejecta, and the rolling elevated topography of the southern crater floor is interpreted to be a mélange of Batson ejecta and slumped Nako crater wall material (Fig. S1).

The elevation ranges corresponding to the benches mark a strong contrast in morphology between the crater rim and floor (i.e., Fig. 11, see valley incision above and below white arrows). Valleys incising the crater wall, generally following the topographic gradient, tend to terminate at the bench level. Below this point we observe two distinctive, but intergrading landforms that extend downslope on the lower crater wall and onto the crater floor: 1) narrow, generally parallel ridges with intervening broad troughs (Fig. 11, black arrows, and paralleling the red line in Fig. S8b), and 2) long, sinuous ridges, sometimes with a downgradient-branched planform (Fig 11b, "μ"). Ridges and troughs do not always conform with crater wall valleys, with an exception shown in Fig. 11a). Longer, sinuous narrow ridges extend towards the basin center in widespread locations within Nako and Salkhad craters ("μ" in Fig. 11b and 12 and Fig. S8 at "2", "3" and "4"). We do not observe benches within Batson crater.

3.4.5.1. Interpretation. We interpret the benches to mark paleolake levels within Salkhad and Nako craters, owing to the marked contrast in landform morphology above and below bench levels on the interior crater wall. The benches do not expose sharp cliffs below the bench level that would suggest that they are outcrops of a resistant bedrock layer, and the bench in Nako crater extends laterally across what is interpreted as depositional apron deposits (rightmost white arrow in Fig 11b). In terms of age, benches seem to pre-date at least some depositional apron activity, e.g., the mantling of the bench at "#" in Fig. 11b. The bench-level contours cross midway down the depositional apron at "1" in Fig. 11a may be mantled with post bench-forming fluvial sediment. The troughs and ridges below the bench level in Figs. 11b and S8b could be constructional, perhaps due to sediment-rich flow sinking beneath an ice cover, or erosional, such as submerged gullies and chutes on steep sidewalls in terrestrial fjords (Batchelor et al., 2018; Brouard and Lajeunesse, 2019; Trottier et al., 2020).

The presence of nearly level benches across 10 to 30 km of the northern crater walls (Figs. 11 and S8) suggests a stable base level encouraging creation of the benches though deposition and possibly erosion. Given the lack of sedimentary infilling of the crater interior to the level of the benches, the lateral constraint promoting bench creation is likely to have been either open-water or ice-covered lakes in the crater basins. Because of the likelihood of cold climate episodes during the late Hesperian-early Amazonian period, lakes would likely have been permanently ice-covered.

The sinuous ridges, troughs, and pancake deltas located below the level of the benches could have formed before, after, or because of, the presence of ice-covered, basin-centered lakes. If formed before the bench formation, then the longer fluvial ridges would likely be channels inverted by eolian erosion. The sinuous ridges marked with "μ" symbols in Figs. 11a and Fig. 12a are light-toned either as a result of mantling by the regional light-toned deposit that was emplaced during the hiatus in regional glacial activity, or by incorporation of eroded light-toned mantle material when deposited. Pre-bench formation does not readily explain the troughs and ridges that lie in contact with, but beneath, the bench levels (Figs. 11b and S8b) and which are not directly connected to valleys above the bench level. FSVs occur on the surfaces of depositional aprons below the bench level, which we and previous studies interpreted to having sourced from melting of former glaciers. The pancake deltas, because of their low elevation in the crater basins, could have formed after considerable drainage of the former ice-covered lakes, but as noted below, formation beneath the ice-covered lakes is also possible.

We suggest that the distinctive geomorphic features below the depositional apron bench levels in Nako and Salkhad craters were created contemporaneously with the benches by subglacial and sub-ice

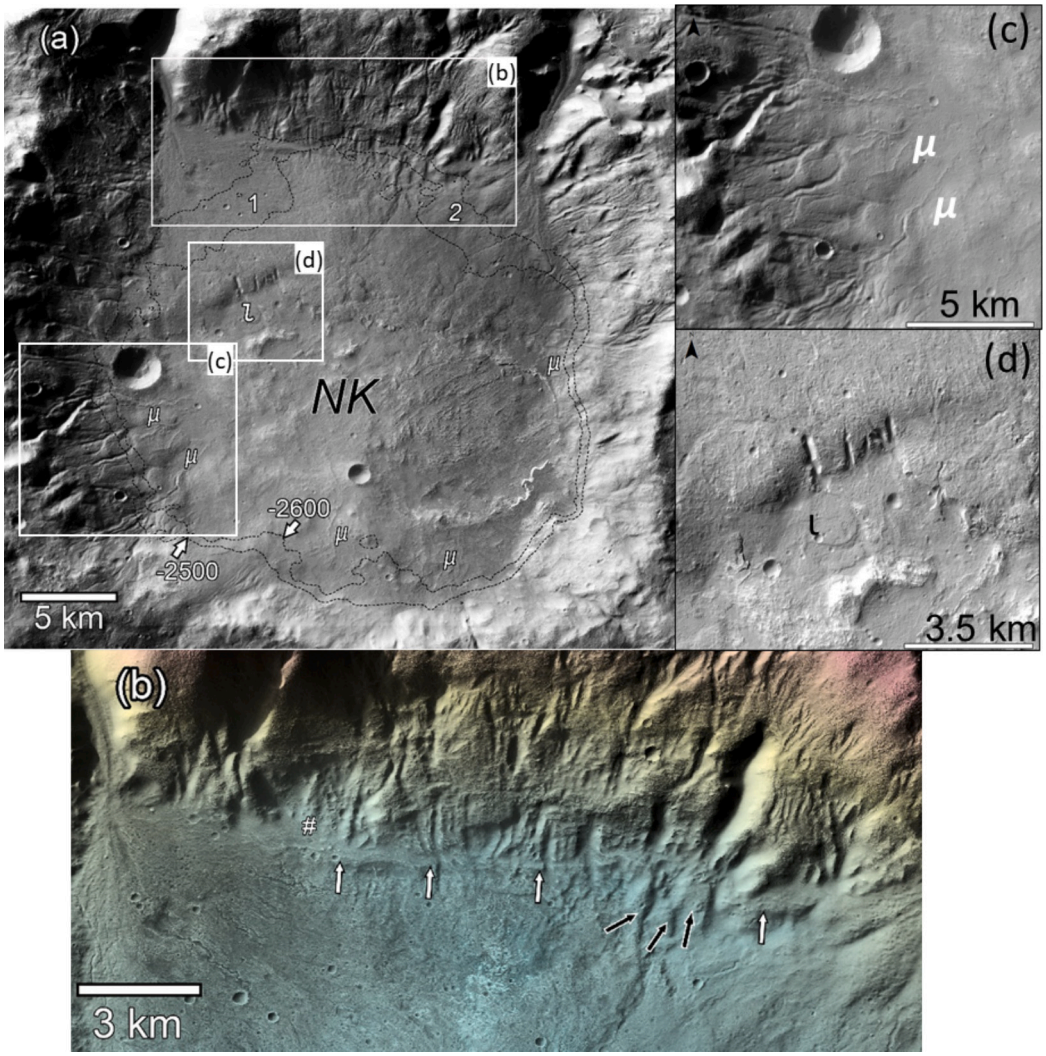

Fig. 11. (a) Interior of Nako crater, showing panels (b), (c), (d), "ι" indicates a crater floor pancake delta, μ are sinuous ridges, and dashed lines indicate contours at -2500 m and -2600 m that bracket the elevation of the bench shown in (b) around the rest of the crater periphery. The bench-level contours cross midway down the depositional apron at "1", and the bench level corresponds to the base of a prominent depositional apron at "2". (b) Narrow topographic bench along the lower northern interior wall of Nako crater (white arrows point to scarp edge). To the left of "#" the bench appears to be mantled by the depositional apron deposits sourced from the valley at the upper left (see the enlargement in Fig. S19). Black arrows point to sloping ridges below the bench level that correspond to valleys on the crater wall. (c) Detail of sinuous ridges "μ". (d) detail of a pancake delta shown by "ι". See Section 3.4.4 and 3.4.5 for details, Fig. 1 for location.

runoff. Subglacial drainage of warm-based glaciers when encountering an ice-covered lake would likely remain as basal drainage beneath the ice cover of the lake, much as Antarctic glaciers drain beneath ice shelves or subglacial lakes. The ice cover on martian crater lakes of Amazonian age would likely be many decameters to hundreds of meters thick, and possibly grounded along the basin margins, limited in ice thickness only by lake chemistry, sublimation mantles, overpressure, supercooled liquid phase, and possible heat influx from glacial strain heating and melt (McKay et al., 1985; Kargel et al., 1995; Kreslavsky and Head, 2002a; Howard and Moore, 2004; Carr and Head, 2019; Turbet and Forget, 2019). If the subglacial water layer was thin, such sub-ice drainage might have formed localized in distinct drainage paths that melt upward through the ice roof while depositing sediment contributed from glacial melting, creating lacustrine analogues to glacial eskers. We suggest that the ridges extending below the bench level are thus esker analogues and are primary rather than inverted features (Fig. 11a). Likewise, the pancake deltas might have formed where sub-ice drainage met deeper water, sandwiched between the ice and the crater floor. The location of the deltas 220-300 m below the bench levels is similar to the estimated ice thickness of ice in the mid-latitude Gorgonum basin at 37°S, where cumulate, flat-topped ridges are suggested to have formed by soft-sediment compressional deformation at the base of the ice cover, either by ice thickening or by loss of total lake volume (Howard and Moore, 2004).

The situation in Batson crater (Figs. 7, 8, S4) is more complex. Depositional aprons extend onto the crater floor interior beyond the depositional apron scarps. These aprons likely pre-date the scarp-forming epoch. Nako crater likewise features depositional aprons that extend below the level of the bench and thus are likely pre-existing. The elevation corresponding to the bench in the northwestern corner of this crater (at "#" in Fig. 11a) appears to have been partially mantled by glacially derived sediment after the bench was formed. That is, this depositional apron received active deposition both before and after the bench-forming episode.

The formation of the benches and associated features in Nako, Salkhad, and Batson craters appears to have occurred late in the glacio-lacustrine history of the region, reflecting an epoch of relative lake level stability but preceded and followed by sedimentation and glacial activity sourced from alpine glaciers on the crater rims.

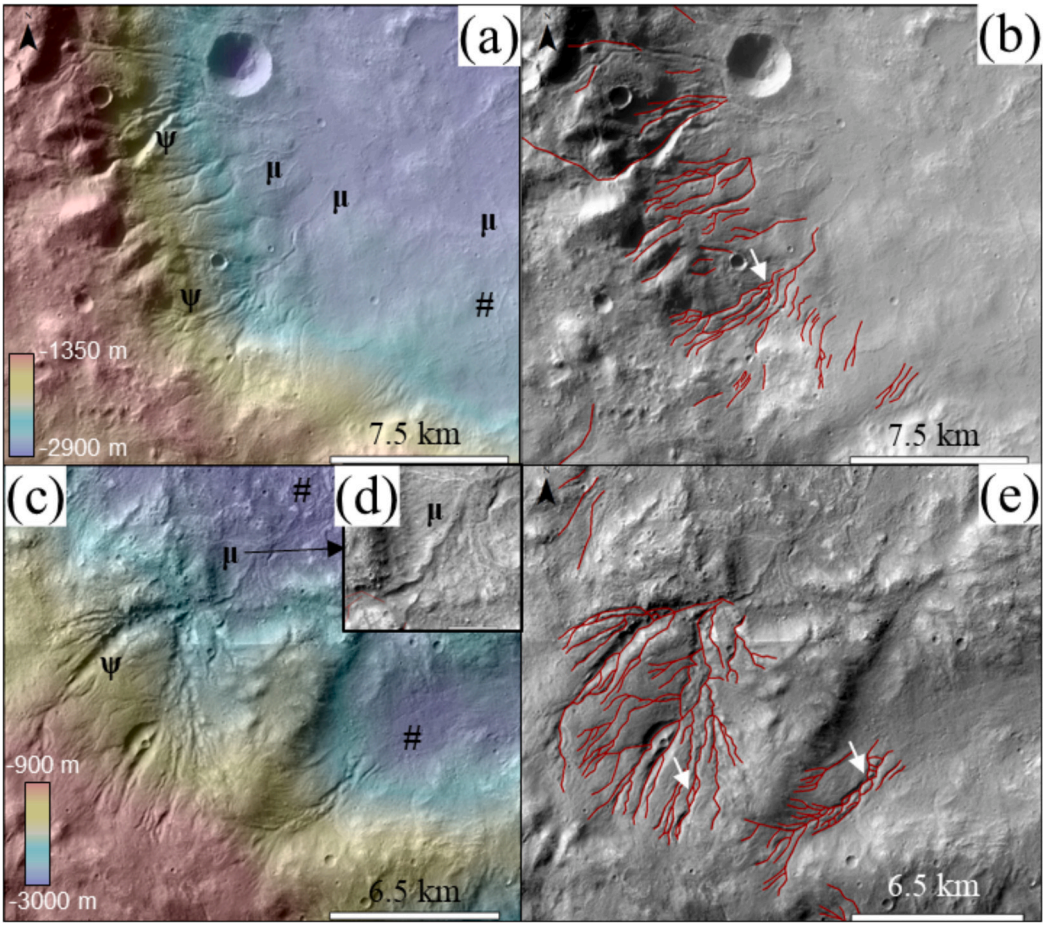

Fig. 12. Fluvial features of crater interiors. (a,b) Southwestern interior of Nako crater. Deeply incised valleys on crater wall (12a, 'ψ') transition downslope into anastomosing valleys (white arrows, 12b) and then continuing as sinuous ridges (12a, 'μ'). (c, d, e) Southwestern interior of Salkhad crater. Lower crater wall valleys are anastomosing (white arrows, 12e). Inset (d) shows a broad sinuous ridge interpreted as an esker or inverted fluvial deposit. Blocky clusters are present on the crater floor near "#"s. Valley axis centerlines shown in (b) and (e) highlight valley anastomosing in the drainages shown in (a) and (c). Image centers: (a) 82.79°E, 29.87°S; (b) 83.63°E, 30.02°S. See Section 4.1, 4.6, and Table 2.

3.4.6. Pancake deltas

Within the crater floors of Batson, Nako, and Salkhad craters are relatively flat topped, fan-like surfaces with low, sharp-edged scarps facing the crater interior, similar in scale and planform to the "Pancake Delta" in Gale crater (Palucis et al., 2016) and "scarp-fronted deposits" mapped globally by Morgan et al. (2022). They occur 220-300 m below mapped bench levels as indicated by "ι"s in Figs. 8, 11d.

3.4.6.1. Interpretation. The convex-outward planform of these scarps and association with upslope valleys indicates they are fluvial deposits characterized as "pancake" deltas (e.g., Irwin III et al., 2005; Palucis et al., 2016; Grant and Wilson, 2019; Wilson et al., 2021). These pancake deltas could have deposited either as sediments from fluvial activity, could have been deposited under an ice or glacial cover, or could have originated as a combination of both. An ice cover could have facilitated deposition as a flat-topped surface. Whereas this remark does not discard a possible subaerial origin, we favor a sub-ice interpretation based on the context, either deposited in a lake covered by a veneer of ice, or in a lake covered by a thick glacial cover. This interpretation also is favored for the pancake deltas found in Salkhad and Nako craters (Fig. 11d).

3.4.7. Undulating plateaus

Gently undulating topography bordering plateau surfaces occurs on the floors of Batson and Jori craters and is characterized by generally smooth uplands bordered by rounded slopes, hills and depressions primarily located surrounding the central peak complex or adjacent to crater walls (Fig. S6), with one occurrence as a band normal to the crater wall west of the lowpoint of the southern Batson crater floor (Table 2). Locally the sides of the uplands exhibit horizontal banding, which, however, cannot be resolved into distinct layers (Fig. 9c). Layering is exposed within a relatively fresh 2.2 km crater to the NE of Batson crater peak. The crater wall exposes sub-horizontal, laterally continuous layering (Fig. 9d), which appears to underlie light-toned material ("#"s), regionally dated to ~ 1Gyr (Howard et al., 2021). However, light-toned deposits also appear to underlie the layered deposits, so that the light-toned exposures on the rim may be overturned crater wall deposits.

3.4.7.1. Interpretation. We interpret this terrain to be the deposit of a sedimentary unit emplaced post-dating the regional light-toned unit previously inferred to be an ashfall deposit (Howard et al., 2021). This interpretation is supported by the observation of layering in the unit stratigraphy (Fig. 9d). The topography along the edge of the undulating unit strongly resembles depositional apron scarps in terms of relief, and indistinct layering (compare Fig. 9a, b with Fig. 9c, d). In Batson crater the elevation of the summits of the hills are in the same elevation range as the depositional apron scarps along the western side of the basin floor but are lower than the scarps in the northern portion of the basin. In Jori crater the undulating unit upper surfaces range from approximately the same elevation as the scarp of the depositional apron on the east side of the crater basin to about 200 m lower. The muted and likely eroded

character of these deposits, however, suggest the undulating plateaus to be an earlier generation of depositional aprons, possibly sourced from the central peaks.

The deposits bordering the central peaks of Batson and Jori crater might alternatively be degraded glacial deposits sourced from the central peaks. Central peak-sourced glaciers are frequently found in mid-latitude craters, e.g. Moreux crater (Sinha and Murty, 2015). The stratigraphic exposures (Fig. 9) are inconclusive of relative components of ice or sediment. We cannot exclude the possibility that these deposits accumulated on a then-higher crater floor and are remnants from later basin floor erosion or subsidence. The exception to these suggested origins may be the undulating plateaus mapped on the lower Batson crater floor (84.41°E and 29.13°S), which are disconnected from the central peak and craters walls and about 300 m lower than the other mapped units.

4. Geomorphology of crater exteriors

4.1. Multiply-connecting and anastomosing valleys

Moderately incised valleys appear on both crater floors and near the sources of drainage from both interior and exterior crater rims, often

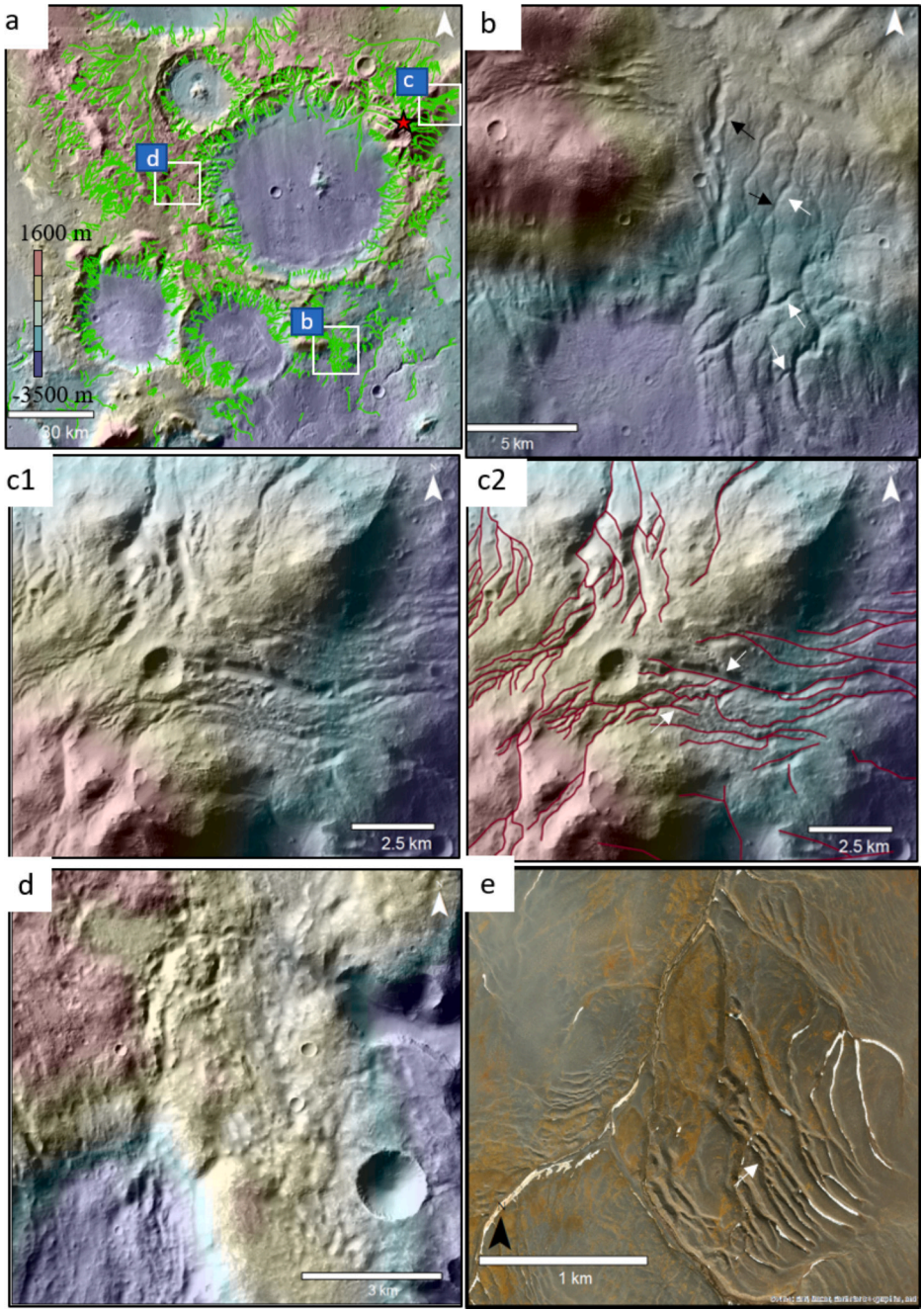

Fig. 13. Context and examples of multiply connected valleys (arrows) (panels b-d) and Earth analogues (e). (a) Elevation shaded CTX mosaic showing all mapped valleys (green polylines), marking the location of panels b-d, and the highest point in the region (red star). (b) shows a southward draining network (center 29.89°S, 84.31°E, elevation -2675 to 625 m) displaying anastomosis in the headwaters and outlet (arrows). (c1 and c2) show a network of subparallel valleys to the NE of Batson crater (center 28.47°S, 84.97°E, elevation -1550 to 1600 m) with anastomosing topologies throughout the whole network (c2 shows mapped streamlines). (d) shows a poorly defined drainage network with labyrinthine topology located west of Batson crater (28.93°S, 83.30°E, elevation -1650 to -450 m), lacking a clearly defined drainage direction. (e) subglacial channels on Devon island, Canada, displaying anastomosis (arrow). See Section 4.1 and Table 2.

featuring anastomosing patterns instead of dendritic planforms. Anastomosis is here understood as multiple interconnections between tributaries, contrastingly with the use of the terms 'anastomosing' and 'anabranching' to describe multiply connected channels in terrestrial sedimentary environments (Knighton and Nanson, 1993; Nanson and Knighton, 1996; Makaske, 2001).

Here the anastomosing valleys are incised into the substrate and appear to lack levees or sediment bars (see, e.g., Fig. 13e for a bedrock terrestrial analogue). Fig. 12 and 13 show examples of valleys with such multiple connections, transitioning downslope into sinuous ridges in Fig. 12a, and intertwining in complex patterns in Fig. 12b (white arrows). Similar valley topologies also occur on the upper crater rims and crater exteriors (Fig. 13b, c). Steeper slopes, including crater walls generally exhibit parallel to dendritic drainage (Fig. 13). Anastomosing valleys in the region are shown in Figs. 12, 13b, 20, S9, S11a.

Several examples of anastomosing networks are observed in the uplands surrounding Batson crater and on the crater rims. Fig. 13 shows three examples of multiply connected valleys, on the rim (Fig. 13c), and on the uplands south (Fig. 13b) and west of Batson crater (Fig. 13d), with morphometric details in Table 2. In Fig. 13b, a swath of valleys draining SSW transitions between dendritic (tree-like), anastomosing (multiply connected), and distributary (tributary bifurcation) topologies (white arrows). Valley cross-sections are largely flat bottomed. The valley displays at least two distinct episodes of formation: an older, more degraded generation drains broadly N-S following the current topographic gradient, including most headwater tributaries. Some of the first-generation valleys were then reactivated by a second erosive episode, enlarging some cross-sections and locally cross-cutting earlier valleys (black arrows in Fig. 13b).

Connecting different tributaries among each other are valleys flowing cross-divide, draining broadly in the ENE-WSW direction, and locally cross-cutting the N-S draining valleys (white arrows). Connecting valleys are often deeper and wider than other tributaries, with steep chutes at either end of the valley. In Fig. 13c, a ~3 km wide anastomosing swath of valleys drains ENE outwards from the NE of Batson crater rim. What appear to be crudely defined fans are located at the end of the valleys branching to the southeast. To the SW of Batson crater rim, labyrinthine drainage consisting of shallow, poorly defined, multiply connected valleys drain into the deeply incised glacial valleys flowing eastwards into the crater, described in previous sections (Fig. 13d, Fig. S9a). Drainage topology in this region ranges from poorly dendritic moving outwards from Batson rim to disorganized and labyrinthine nearing Batson crater (Fig. 13d).

4.1.1. Interpretation

We interpret the weakly dendritic to anastomosing systems, as well as labyrinthine topologies that are observed throughout the uplands surrounding Batson crater (Figs. 12, 13, 18b, e, and S11) to be subglacial in origin. Whereas anastomosing river channels are found on Earth, they most often develop in low energy environments nearing the base level (Makaske, 2001). Braiding channels, another example of multiply connected topologies in fluviatile systems, form when rivers transport large sediment bedload that accumulates forming ephemeral streamlined bars, around which water diverts. Such braided and anastomosing rivers do not feature branches incised deeply into inter-channel islands, or located near the headwater, as seen here.

Network topologies consisting of multiply connected channels or valleys are commonplace in subglacial drainage systems (e.g., Denton and Sugden, 2005, Greenwood et al., 2007, Grau Galofre et al., 2018). Grau Galofre et al. (2018) describe well-preserved subglacial networks on Devon Island, Canada that are nearly parallel, weakly dendritic, and anastomosing in the headwater reaches, and that are excavated into plateaus underlain by dolomite (Fig. 13e). Similar terrestrial examples of anastomosing valleys are shown in Fig. S10b, c. Multiple tributary joints in a network may develop to the point where they dominate the drainage topology and obscure any drainage hierarchy. An example is the reticulate "labyrinth" terrain in Wright Valley, Antarctica (Denton and Sugden, 2005), which consists of a series of channels carved into a 300 m thick layer of limestone bedrock (Fig. S11c). 'Tributary' junctions are marked by deep potholes, whereas longitudinal profiles reveal slope reversals. Labyrinthine terrain, similar in scale but less deeply incised, is also apparent in satellite images of Devon Island (Fig. S11). In general, valley anastomosis in subglacial drainage systems has been related to sequences of subglacial floods of moderate magnitude, e.g., Fig, 13d, Fig. S11 (Lewis et al., 2006; Marchant et al., 2011).

The cross-cutting relationships identified (Fig. 13b) suggest that at least two events were involved in the formation of some valleys in the region, with the second event responsible for driving flow across drainage divides, another typical characteristic of subglacial drainage. Anastomosing patterns and junction morphologies involving steep chutes on either side of valleys connecting between tributaries are typically seen in terrestrial analogue subglacial channel networks (Fig. 13; Grau Galofre et al., 2018).

4.2. Valleys crossing drainage divides

Valleys within drainage networks located on the uplands around Batson, Salkhad, and Nori craters can often be observed in discordance with surface slope, either crossing local drainage divides or flowing oblique to local slopes, as shown in Fig. 14a, b and S9b. Basins "W" and "E" on the southern exterior slope of Batson crater (Fig. 14b) are connected by the three numbered valleys that initially climb from the eastern basin before descending westward. The inset shows a narrow sinuous ridge on the western upward slope of valley 1 associated with a shallow trough leading to basin "W". The divide profile shows that valley 1 incised 60 m into the ridge, which is 145 m high. Valley 3 occupies a linear trough on the western side of the ridge. Valley 2 is not associated with a defined depression on the western downslope.

Fig. 14c shows multiple valleys draining a near-circular, ~3.2 km wide basin, likely a highly degraded impact crater (marked "#"). Runoff to this basin came from multiple sources (arrows). An unusual feature of this basin is multiple valleys that formed from effluent discharge from the basin (at arrows "1"- "5"). Valleys "2" and "5" breach the crater rim close to the floor level of basin "#". Valleys "1" and "3" exit the basin well above the floor level but breach the crater rim. Valley "4" is less definitive in incision depth and rim incision. The valley networks at and downstream from locations "6" and "7" are multiply interconnected. The valley marked "1" cuts into the anastomosing network "6" and flows oblique to topography. A collection of intertwined, slightly sinuous ridges at "8" leads from the drainages sourced from valleys "1"- "7" to the center of the basin "W", which is the same basin shown in (b). Valley cross-sections range from V-shaped to steep sided, flat bottomed, typically ~100-500 m wide. The inflowing drainage along the northernmost white arrow likely was sourced from the upland basin at "&" through the divide notch at 9.

4.2.1. Interpretation

Valleys that cross divides between basins (Fig. 14) might originate from a variety of mechanisms, including:

1. Structural influences, including easily weathered strata, weathering of fracture zones, or narrow grabens, differential uplift, or a constructional initial landscape (e.g. ejecta) with happenstantial inter-basin connections. Often these are just low divides between valleys exploiting structural weaknesses (e.g., Whitfield and Harvey, 2012) and do not imply fluvial flow crossing the divide.
2. Headward erosion of a valley leading to drainage capture (Howard, 1971; Bishop, 1995; Stokes et al., 2023). This usually occurs when fluvial downcutting on one side of a divide exceeds erosion on the other side of the divide, generally driven by greater relief on the side with deeper erosion.

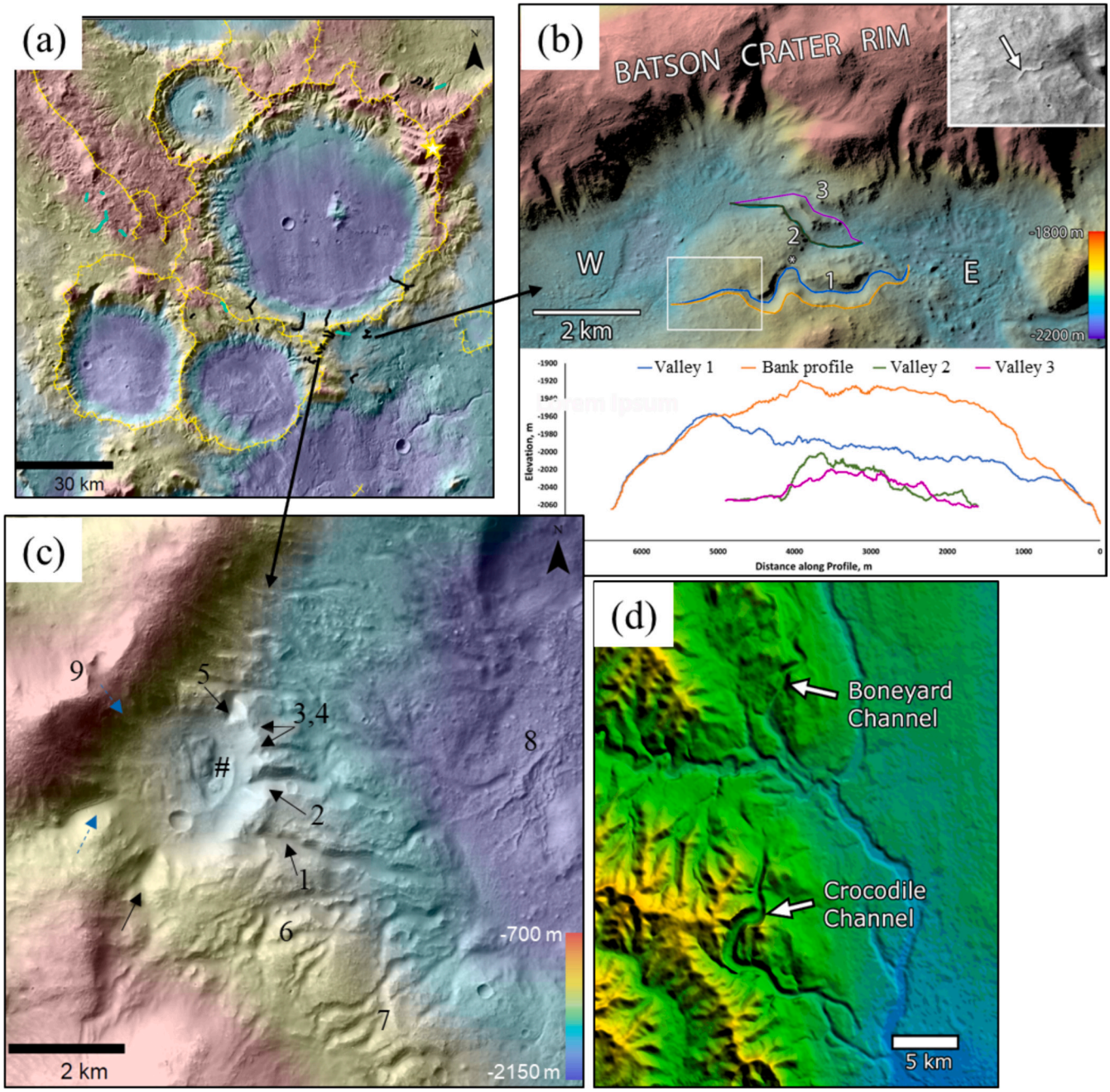

Fig. 14. Valleys discordant with topography on the Batson crater region. (a) Context map showing the main drainage divides (yellow dashed lines), valleys cutting across divides (black) and valleys oblique to topography (turquoise), marking the insets in b-c. (b) Valleys connecting basins across a ridge and their longitudinal profiles. Two depressions on the southern rim of Batson crater are connected by sinuous valleys (marked "1-3") that incise into a 145 m high ridge dividing the basins to the east (E) and west (W). A sinuous ridge (upper right inset) descends from the western end of the incised portion of valley "1". (c) Multiple valleys drain a basin. The near-circular, 3.2 km depression at "#" is likely a highly degraded impact crater with runoff coming from multiple sources (blue arrows: inlets, black arrows: outlets). Valleys "1, 2, 3, 5" are seen breaching the rim and outflowing eastwards into the basin. See section 4.2 for discussion. (d) Colored hillshade of analogue terrestrial tunnel valleys boneyard channel and crocodile channel near Stavely, Canada (Rains et al., 2002). Image location 113.8°W, 50.1°N. Ice flow was NNW to SSE, and total elevation range of about 900 m.

3. Subsurface drainage from a higher valley into a lower valley, implying either soluble bedrock or high permeability, low cohesion substrate (Hack, 1960).
4. Overtopping of divides by ponded drainage, often leading to catastrophic incision such as the Pleistocene overflow of Lake Bonneville (Gilbert and Lake, 1890; Meade, 1968; O'Connor, 1993).
5. Pressurized flow beneath glaciers, creating tunnel valleys and subglacial channels (Kehew et al., 2012; Van der Vegt et al., 2012) or divide-crossing eskers (e.g., Fig. 13b).

Scenarios 1 and 3 are generally random and are unlikely to exhibit multiple instances in a regional setting. In martian landscapes the overall depth of fluvial incision is generally modest relative to terrestrial (e.g., Irwin III et al., 2005; Howard, 2007; Grau Galofre et al., 2020b), so that scenario 2 should likewise be rare. The topography of Mars is largely constructional due to tectonics, volcanism, and impact cratering, encouraging overtopping as a process of valley incision crossing divides. Exit-breach lakes are evidence of this mechanism on Mars (O'Connor, 1993; Howard, 2007; Fassett and Head, 2008; Matsubara et al., 2011;

Mangold and Howard, 2013; Goudge et al., 2021), and a number of small crater ("tadpole-like" craters) evidence exit breach overflow with no upstream contributing area other than the crater itself (Wilson et al., 2016; Warren et al., 2021, 2023). Most martian examples of crater divide breaching by overflow involve significant upstream contributing area. Many exit breach craters have multiple exit breaches at different levels, which is difficult to explain unless ice cover above the rim is involved (Warren et al., 2023), because incising streams are very intolerant of multiple drainage pathways.

In the Batson crater study region multiple potential divide-crossing valleys are present (Fig. 14b, c), and at least two basins have multiple exit valleys, with one example the 3 km basin in Fig. 14c, with 3 or 4 exit breaches. These divide-crossing valleys, as seen in Fig. 14d, are best explained by pressurized overflow under an ice-covered landscape.

4.3. Interconnected shallow depressions

The exterior rim of Batson crater features multiple shallow, irregular depressions (Fig. 15, Table 2). These depressions range in size between 1- 10 km and are roughly elongated in the ENE-SSW direction (Fig. 15a), increasing in size and definition towards the south and east of Batson rim (Fig. 15b, numbered sequence). Some of these shallow depressions are interconnected through channels. Fig 15g. shows three drainage systems draining in distinct directions, numbered according to their order in the sequence : eastwards (Fig. 15b, white sequence 1-4), southwestwards (Fig. 15b, black sequences 1-4) and southwestwards 1'-4'). A deep valley is seen draining westwards into Batson crater between 2' and 3', note the pancake delta 'ι' at its terminus.

We find that clusters of hummocky material tend to occupy the interior of these shallow depressions (Fig. 15b, c, 'o') as described in detail in Section 4.4. However, depressions without hummocks are also found further west (Fig. 15a, b). Sinuous ridges, shown with white arrows in Fig. 15b, c appear within or at the end of some valleys connecting cavities, notably towards the lower reaches of the sequences 1-4 and 1'-4' in Fig. 15b. In Fig. 14c, a sinuous ridge is observed at the termination of a connecting channel (arrow, see inset in Fig. 14b). The depression marked with a white number 3 in Fig. 15b is bounded by a transverse ridge that is breached in at least two locations (black triangle).

4.3.1. Interpretation

We interpret the sequences of interconnected shallow depressions as interconnected subglacial cavity systems. These smooth, seemingly isolated depressions are perched at the top of Batson crater rim, much higher in elevation than the surrounding terrain (Fig. 15a, b). This is inconsistent with surface runoff deposition, as (1) these depressions are often disconnected from any water or sediment source, and (2) they are located near or at the drainage divide, minimizing the source area available (Fig. 15b). Two possible interpretations for the origin of these shallow depressions are: 1) at least one large, widespread snow and ice

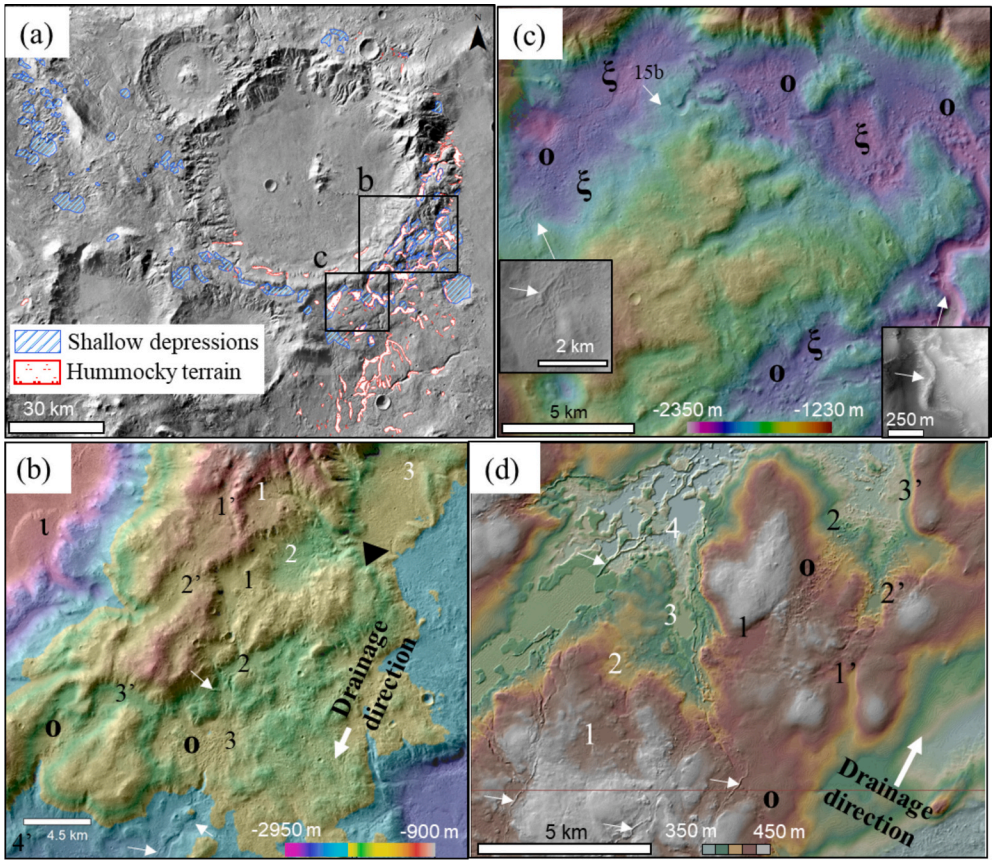

Fig. 15. Interconnected shallow depressions and associated landforms. (a) Distribution of interconnected shallow depressions (dashed blue) and hummocks (dotted red, also Fig. 16). Black boxes mark insets in (b) & (c). (b-d) shallow depressions (numbered in sequence or indicated by 'ξ'), hummocks ('o'), sinuous ridges (white arrows), pancake deltas ('ι'), and breached transverse ridges (black triangle) on Batson crater (b, c) and terrestrial analogue (d). In (b) three different shallow depression drainage sequences are shown numbered from inferred source to sink (numbers in black drain SSW, in white drain E), from inferred source to sink (numbers in black drain SSW, in white drain E). Center: 29.39S, 84.80E. (c) Interconnected shallow depressions and associated landforms south of Batson crater (center: 29.63S, 84.45E). See section 4.3 for discussion. (d) Terrestrial analogue glaciofluvial hummocky corridors and interconnected subglacial cavities. Former subglacial cavities drain in sequence (numbers) through poorly defined channels (orifices), and are associated with glaciofluvial hummocks and eskers. Image center is located 66.764N, 90.219W, the landscape was reworked under the Laurentide ice sheet.

melt event, which could explain the discharge required for the overspill of these shallow depressions, their presence at or near the drainage divides, and the weak connectivity owing to increased water supply, or 2) interconnected subglacial cavities, which could similarly explain their weak connectivity, presence of hummocks infill, and distribution at or near the rim drainage divide (e.g., Lewington et al., 2020).

Analogue interconnected subglacial cavity systems are commonly found on Earth in locations covered by Quaternary glaciation, including Canada and Scandinavia (e.g., Dewald et al., 2022). We propose an example from Nunavut, Canada (Fig. 15d), where we observe similar depression morphologies and scales, and an assemblage of landforms that includes sinuous ridges, hummocks, shallow depressions, and connecting channels at various levels of definition. This terrain (Fig. 15d) was sculpted by the northwestward drainage of the northern Labrador ice dome, former Laurentide ice sheet. Glaciofluvial features are located at the hilltops or near the drainage divides, connected through poorly defined shallow channels, and associated with hummocks (Fig. 15d '**o**') and esker ridges (white arrows). Subglacial cavities (numbered sequences, Fig. 15d) have an irregular shape, slightly elongated towards the drainage direction and in some instances contain hummocky infill '**o**'.

Subglacial interconnected cavities develop when subglacial water drainage accumulates in points of minimum hydraulic potential, which can occur due to local depressions (Flowers, 2015; Livingstone et al., 2022). Subglacial cavities store basal meltwater until the hydropotential seal breaks, which can occur either by increased water pressure or by enhanced cavity leakage. At this point cavities become an active supplier of highly pressurized water and sediment into the subglacial drainage system, and can become interconnected through meltwater corridors and orifices (Kamb, 1987; Fountain and Walder, 1998; Flowers, 2015). Water levels within cavities need not be level, as ice slope plays a more important role than basal slope. This is apparent in Fig. 15d, for

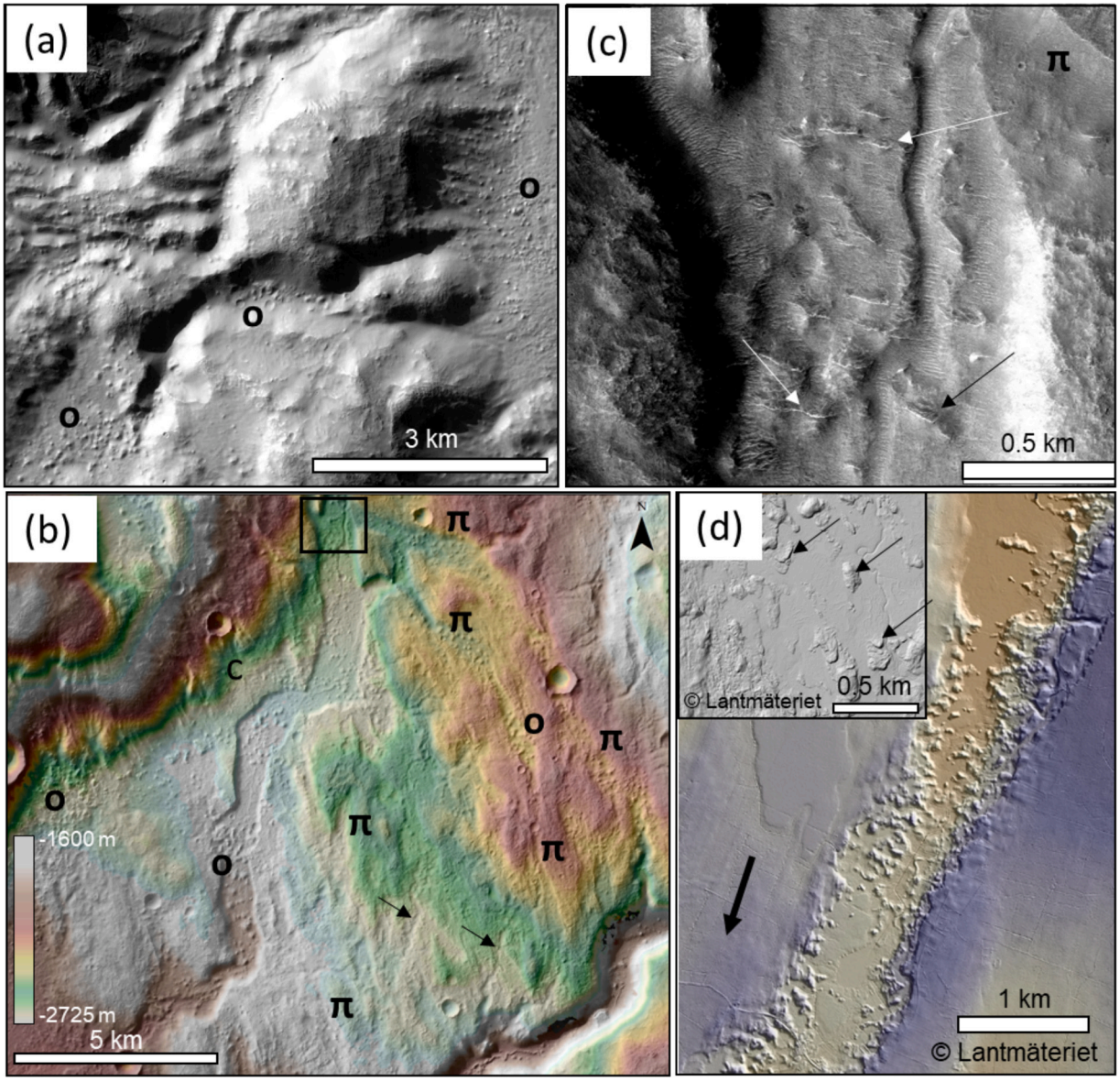

Fig. 16. Hummocks and linear troughs. (a) Eastern exterior slope of Batson crater rim (center: 28.82S, 85.02E), showing hummocks '**o**' accumulated in relative lowpoints and deep fluvial incision, with fan-like deposits at the foot of the valleys (right). (b) NNW-SSE trending shallow troughs '**π**', bounded by the Navua Valles A to the SSE (image bottom) and its main tributary to the NNE (image center), with hummocks '**o**' and shallow channels shown with arrows. Image center: 29.92S, 84.67E, color stretched. (c) HiRISE image focused on the inset in panel (b), showing hummocks (arrows), without visible stratigraphy. Notice crude lee and stoss sides (arrows). (d) Terrestrial analogue Glaciofluvial Hummocky Corridors (GHC) (right) in southern Sweden. Bold arrow shows ice flow direction. Left inset shows a LiDAR example of hummocks and murtoos (arrows) (center: 61°28'N 13°11'E, trough depth ~10 m). See Section 4.4 for details.

example, where cavities are perched on sloping terrain or do not form a clear topographically confined basin; and is also apparent in several depressions on the eastern rim of Batson crater that are sloping or not topographically confined, yet display smooth floors and occasional hummock infill (i.e., 3' in Fig. 15b).

4.4. Hummocky material and linear troughs

Hummocky material, taking the form of blocks distributed in clusters, consists of areally extensive collections of fragments 10 to up to 250 m in size without visible stratigraphy (Figs. 16c '**o**'; S12, arrows). These are different from the supraglacial boulder trains described above because they are not associated with any remaining glacial deposit, they are not found forming trains, and they do not display the characteristic light toned material of GLF supraglacial debris in this region. In addition, they display a shape that is crudely hydrodynamic, with lee and stoss sides that can be identified in some examples (Fig. 16c, arrows). Hummocks within clusters are areally scattered (Figs. 15a, 16a, b, and c '**o**', S12), unlike the congested bars and fans typically deposited by dilute fluvial flows. South of Batson crater, hummocks preferentially occupy the interior of shallow linear troughs (Figs. 15a, 16b '**o**'), the floor of the Navua A Valles (Fig. 16b, S11) and the floor of its main tributary (Fig. 16b, c).

Linear troughs are swaths of subparallel, shallow, crudely defined troughs, found S-E of Batson crater, generally trending NNW- SSE oblique to local slope (Figs. 16b, S12). Troughs are commonly infilled with hummocks (Fig. 16b, '**o**'), and are also found in association with small valleys (Fig. 16b, arrows). Two large troughs are seen branching out of the Navua A NNE tributary at '**π**' (Fig. 16c) and merging with the Navua A Valles to the south (Fig. 16b). Junctions are in a higher level than the tributary or Navua A Valles valley floors, defining a terrace (Fig. 16c). The swath of troughs and hummocks ends to the south at Navua A Valles (Fig. 15a).

4.4.1. Interpretation

We discuss four possible origins of the linear troughs observed south of Batson crater: structural control, ejecta from Batson crater, erosion by glacial sliding, and glaciofluvial erosion. The linear troughs do not have the straight and abrupt lateral boundaries that would suggest a dominant structural control. Control of the broader undulating relief by structure is also not evident. Origin as ejecta texturing is also a possible explanation for terrain surrounding large craters such as Batson crater. Ejecta textures from neighboring craters are a likely explanation for patches of aligned ridges and troughs on the floors of Batson, Salkhad, Nako, and McCauley craters. In the Amazonian-aged Hale crater, El-Maarry et al. (2013) and Morino et al. (2023) described an association of blocky material and channels consisting of braided channels, large amounts of debris transported within the fluvial or debris flows, and fluidized ejecta. This picture is unlikely here for the following reasons: Batson is a Late Noachian crater, whereas Hale is an Amazonian crater. The degree of preservation and exposure found on these landforms makes it unlikely they date from the Noachian. Next, the linear trough direction does not match the expected radial ejecta blanket direction, nor the ejecta direction found further to the south. Finally, troughs and hummocks emerge from the Navua A Valles N tributary (Fig. 16c, '**π**') and merge into the Navua A Valles (Fig. 16b), with the Navua A Valles acting as a significant sink of hummocks (Fig. 15a). Since the Navua A Valles is Amazonian (Hargitai et al., 2018a, 2018b, 2019), and thus much younger than Batson crater, age relationships also stand against this hypothesis. Equally unlikely seem to be the possibility of fluidized ejecta material with other sources, because there are no craters in the region that are both younger and large enough so that their ejecta blanket would extend to the southern and eastern Batson rim. We cannot discard, however, that some of the elements visible in the landscape, notably the surface texture, inherited characteristics from the Noachian ejecta blanket.

Origin as glacial lineations is possible, requiring the presence of a warm-based glacial cover, with large enough driving stresses to offset the lower martian gravity (Benn and Evans, 2010, Grau Galofre et al., 2022), but does not provide an obvious mechanism to preferentially deposit hummocks inside shallow depressions and troughs, as observed in Fig. 15b and 16b. The fourth possibility is deposition by subglacial drainage, once again requiring a glacial cover with basal melt. Terrestrial analogue glaciofluvial landscapes found as vestigial fingerprints of the Scandinavian and Laurentide ice sheets capture similar landform associations to those found in this region, in the form of Glaciofluvial Hummocky Corridors (GHC), shown in Fig. 15d (upper right corner) and 16d (i.e., Dewald et al., 2022). Glaciofluvial hummocky corridors (GHCs) are channelized features with different degrees of definition, formed by subglacial meltwater flow and roughly aligned in the direction of former ice flow (Fig. 16d). Glaciofluvial hummocks, in turn, are mounds gathered forming tracts of irregular topography within GHCs, as shown in Fig. 16d (Utting et al., 2009; Peterson and Johnson, 2018; Vérité et al., 2023). The crudely hydrodynamic, V-shaped planform found in some hummocks (Fig. 16c, arrows) resembles that of murtoos or murtoo-related forms (Peterson et al., 2017; Vérité et al., 2023), a landform found commonly in association with glaciofluvial hummocks (Fig. 16d, inset). Smaller meltwater channels (~10 m), eskers, and transverse ridges are also frequently observed within or around the meltwater corridors (Vérité et al., 2023).

The troughs and hummocks found south of Batson crater match the scale of the terrestrial analogues (compare Fig. 16c, d), which also capture hummock and linear trough distribution, and the association with sinuous ridges and channels (Fig. 16b, arrows). The interpretation of linear troughs and infilling hummocks south of Batson crater as GHCs is consistent with the environmental scenario consisting of a linked subglacial cavity system on the eastern rim of Batson crater, transitioning into a GHC dominated drainage as the system progressed southwest and water input grew. This landscape was emplaced after the erosion of the Navua A Valles, and either after or during the emplacement of its tributary, owing to the distribution of hummocks and the spatial connections described (Fig. 16b and c).

4.5. Navua A Valles and tributary

The Navua Valles consist of a series of fragmented, poorly integrated valleys covering a large area, which have been previously described in detail (Mest et al., 2010; Hargitai and Gulick, 2017; Hargitai et al., 2019) The northwesternmost portion of the system, the Navua A Valles transported water from headwater regions that are indistinct in imaging down the Hellas basin floor with little additional input from independent tributaries (Hargitai et al., 2019). The valley may have originated during the late Noachian as the downstream continuation of drainage systems northeast of Batson crater (Mest et al., 2010) but the connection is obscured by Batson crater ejecta. The present well-defined portion of the valley initiates abruptly southeast of Batson crater at (85.20E, 29.95S, Figs. 1, 17a, and S12) and consists of several segments with different degrees of incision within a drainage basin oriented ENE – WSW. Morphometric details are summarized in Table 2, and in Hargitai et al. (2017a, 2017b, 2019). The longitudinal profile of both the Navua A Valles and its tributary present stepped sections, as well as sections with localized reversed slopes, as shown in Fig. 17b. Both drainage systems are concordant with regional topography.

4.5.1. Interpretation

We infer that the processes shaping the Navua A Valles were likely a combination of fluvial and subglaciofluvial erosion. Previous stratigraphic analysis indicated that different valleys within the Navua Valles system originated at markedly different times and were reactivated (Hargitai et al., 2018a, 2018b), with an older event likely Noachian/Hesperian in age involving the portion of the Navua A Valles downstream from the present study (Hargitai et al., 2018a, 2018b), and a

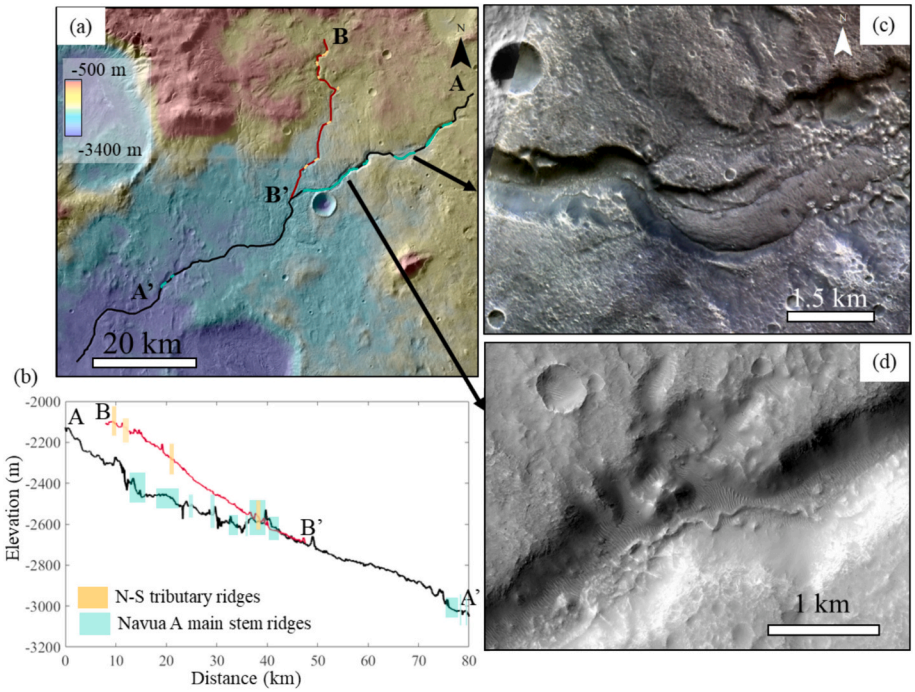

Fig. 17. Navua A Valles and tributary. (a) Color-shaded HRSC elevation on CTX mosaic showing the valley axis of the Navua A Valles (black) and its N-S tributary (dark red). Sinuous ridge segments within the valleys are marked in turquoise for Navua A and in orange for its tributary. (b) Longitudinal profile of Navua A Valles (A-A', black) and its N-S tributary (B-B', red), marking the location of sinuous ridges in relationship with profile slope and with panel (a). (c) CaSSIS image showing a sinuous ridge with a broad and wide geometry (image center). (d) HiRISE image showing a narrow-crested portion of the sinuous ridge. See Sections 4.5 and 4.6 for details.

resurfacing event in the Amazonian leading to the formation of the portion shown in Fig. 17a. Whereas the older event was likely the result of fluvial runoff, we argue here that the Amazonian reactivation of Navua A was driven by subglacial flows, at the very least the portion of the valley south of Batson crater. We support this claim on four bases: (1) the context, where inferred glaciofluvial hummocky corridors drain into the Navua A Valles and other glacial and sub-glaciofluvial landforms are interpreted to be present in the region (eskers, interconnected cavities, crater wall striations, etc.), (2) the presence of sinuous ridges of variable width within the valley, interpreted to be eskers in the next section, (3) the intermittency of the valleys, which appear and disappear but maintain consistent morphologies, and (4) the stepped nature of the longitudinal profile, shown in Fig. 17b. Our interpretation is broadly consistent with Hargitai et al., 2019 remarks on a possible fluvioglacial origin of the Amazonian Navua A Valles.

4.6. Sinuous ridges

Sinuous ridges on crater exteriors are found both in the interior of Navua A Valles and its main tributary, as well as in association with shallow depressions, as discussed in Section 4.3. The sinuous ridges within Navua A Valles have a mean sinuosity of 1.09+/- 0.03 (supplementary dataset) with a mean segment length of 2800 +/- 1060 m, a mean ridge width of 62 +/- 4 m, and a mean ridge height of 11 +/- 1 m. Ridge height was measured using the shadow shape technique as described in section 1.2. We built a width (W) - height (H) scaling from a total of 33 empirical observations (see supplementary dataset and Fig. S10) for the Navua A Valles ridge, yielding:

$$H = CW^{1.1\pm0.3}, \text{with p} - \text{value } p = 1.03E - 10 \quad (1)$$

Narrow ridges within the Navua A Valles are discontinuous and display changing cross-sectional morphologies, which range from narrow crests (Fig. 17d) to broader, wider crests (Fig. 17c) with broader crested ridge sections appearing in valley widenings, possibly because of the decrease in water shear velocities. In Fig. 17b, we show the location of sinuous ridges with respect to the profiles of Navua A Valles (black) and its main tributary (red). Note that many ridges are spatially located in regions of profile flattening, or profile reversals. We find hummocky material associated with these ridges, both inside the Navua A Valles and its main tributary (Fig. 17c and d). Similar, but less extensive sinuous ridges are observed in the uplands S-SE of Batson crater (see e.g., Figs. 14b, 15b, c - white arrows) within or at the termination of valleys.

4.6.1. Interpretation

We interpret the sinuous ridges inside Navua A Valles and its main tributary (Fig. 18), as well as smaller sinuous ridges found on crater

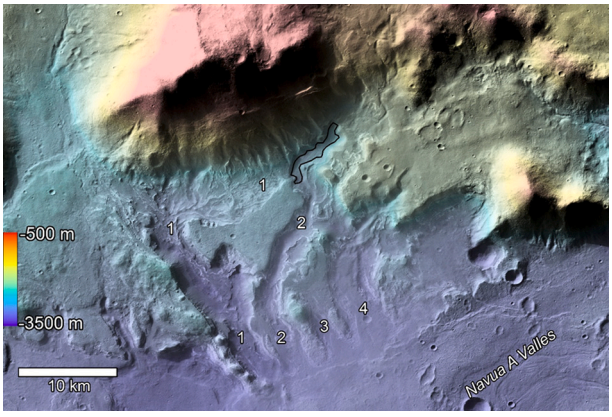

Fig. 18. Features at the southeastern end of the study region. Broad valleys 1-4 extend southward to the Navua A Valles from the massif at top of image. As discussed in (Howard et al., 2021) after the valleys were eroded the landscape received a light-toned mantle that was partially reworked by fluvial processes and eolian erosion. The dark line delineates an extant ice deposit in valleys 1 and 2. See section 4.7 for details. Image center at 83.01°E, 30.63°S.

exteriors (Fig. 17 and 15) to be eskers, acknowledging the limitations in the identification of eskers and inverted fluvial paleochannels from remote sensing observations (Butcher et al., 2021). We favor the esker interpretation given that: (1) sinuous ridges are found here spatially associated with longitudinal profile flattening and slope reversals in the Navua A Valles (Fig. 17b). This is consistent (albeit not distinctive by itself) with subglacial deposition, as flattened and reverse profile sections lower the sediment carrying capacity of channelized subglacial meltwater, favoring sediment deposition.

(2) Sinuous ridges are found associated with hummocks and other interpreted glaciofluvial landforms (e.g., Fig. 17c and d, Fig. 15b, c). Glaciofluvial hummock formation is argued to require high discharges (Vérité et al., 2023), in contrast with the environments known to preserve and expose inverted fluvial paleochannels. However, esker ridges on Earth are commonly associated with hummocks in GHCs, as shown in Fig. 15d (e.g., Utting et al., 2009; Sharpe et al., 2021; Vérité et al., 2023).

(3) Sinuous ridge morphologies are more in line with those of esker ridges observed on Mars and Earth than with those of inverted paleochannels. Eskers are primary, constructional landforms and their morphometric relationships are expected to mirror the characteristics of subglacial channels and the dynamics of subglacial deposition. Inverted channels are not primary landforms, they result from weathering, differential erosion, and degradation, and thus their morphometry is expected to be comparatively much more randomized. The empirical width to height scaling derived here shows a meaningful trend (Fig.S10, $H \sim W^{1.1\pm0.3}$), and implies that height increases here more strongly with width than the $H \sim W^{0.2\pm0.3}$ reported for inverted paleochannels in Utah (supplementary information in Hayden et al., 2019), but within the error bars of the scaling relationships found for eskers on Mars ($H \sim W^{0.7\pm0.3}$ from supplementary data presented in Butcher et al. (2020), for Dorsa Argentea ridges (a linear relationship, H∼W, is shown in Fig. 9, (Butcher et al., 2016), and Earth ($H \sim W^{0.5\pm0.4}$, from data in Burke et al. (2015)).

Additionally, measured sinuosity ($S = 1.09 \pm 0.03$) is consistent with observations of a large database of eskers on Earth ($S = 1.08$ (Canada); $S = 1.06$ (Kola Peninsula, Russia); (Hättestrand and Clark, 2006)), as well as with glacier-linker esker systems on Mars (Butcher et al., 2020) and Dorsa Argentea ridges ($S = 1.10 \pm 0.01$; (Butcher et al., 2016)). By comparison, fluvial inverted paleochannels tend to have slightly higher sinuosity on Earth ($S = 1.2 – 1.5$, (Harris, 1980, Williams et al., 2009)), whereas on Mars Burr et al. (2010) reported that most inverted paleochannels in Aeolis Terra have sinuosity $S \sim 1.1$-1.5. Finally, the assemblage of landforms identified around Batson crater, in particular to the east and south, is most simply captured by a subglacial setting similar to that in Fig. 15d than by a combination of many different processes.

The situation inside the craters, illustrated in Fig. 12 (‘μ’) is less clear. Ridges here are all found at roughly the same topographic level, emerging downslope from a crater rim valley that is often dendritic and anastomosing. Nako crater sinuous ridges are degraded in comparison with ridges found on the intercrater uplands and SE of Batson crater (compare Fig. 12a with Fig. 15 and 17). We cannot discard the hypothesis of relief inversion for ridges in Nako crater given the impact of erosion in their preservation, and the lack of direct association with other possible glaciofluvial landforms. Ridges in Salkhad are much better preserved (Fig. 12c) and are associated with heavily anastomosing valleys, pointing at their origin as eskers. Whereas we cannot completely rule out an origin as inverted paleochannels, the environmental context, morphometry, and morphology consistently support our interpretation of sinuous ridges outside of craters as eskers. We also interpret that sinuous ridges within Salkhad crater are more consistent with eskers than with inverted channels, whereas the lack of associated landforms and the state of degradation of Nako ridges prevents us from reaching a confident interpretation.

4.7. Southwestern (SW) broad valleys

A set of wide, trough-like valleys (“1” - “4” in Fig. 18) extend from the foot of a Hellas basin massif, which preserves a patch of extant ice (outlined in black in Fig. 18), to the Navua A Valles. As discussed by Howard et al. (2021), the valleys appear to be incised into terrace deposits of Navua A Valles. After the valleys were eroded, they were mantled by terrain-conforming light-toned deposits and were partially reworked by fluvial activity (e.g. sinuous channels along the axis of valley “1”). The mantle was subsequently partially stripped.

4.7.1. Interpretation

Fig. 18 shows a small remnant of a possibly larger ice cap that excavated the valleys located at the head of the valleys ‘1’ and ‘2’. The trough-like cross section of the valleys may reflect glacial scour, which although not favored by the low martian gravity (Grau Galofre et al., 2022) may have been aided by the high relief of the massif or the possible unconsolidated state of the terrace deposits into which the valleys were incised. The terrain-conforming light-toned mantling unit was emplaced after the postulated glacial activity in this location, but some fluvial reworking occurred subsequently, perhaps sourced by remnant ice cover on and upslope from the massif. This sequence of post-glacial light-toned mantling followed by moderate, FSV-style fluvial incision is similar to the inferred glacial activity in Nako and Salkhad craters.

4.8. Dissected highlands west of Batson crater

The region located west of Batson crater, bounded by Nako crater on the south and McCauley crater to the north is characterized by undulating terrains incised by locally dense drainage systems, with an NNW-SSE trending massif setting the main drainage divide (Fig. 19a,b). Many of the western uplands valley systems roughly fall within one the three zones identified in Fig. 19c-e: Zone I, dendritic to multiply-connected topology; Zone II, weakly dendritic systems interconnected with shallow basins; Zone III, multiply-connected, labyrinth like topologies.

The region illustrated in Fig. 19c exemplifies drainage topologies in Zone I. Valleys in Zone I are characterized by dendritic planforms with occasional multiply-connected sections (‘λ’), and a drainage density of ∼0.5 m^{-2}. The drainage system here is largely concordant with topography (Fig. 19a, b), although individual valleys are observed to connect separate networks across drainage divides (Fig. 19c, ‘ν’). Cross-cutting relationships observed in valleys in Zone I suggest at least two drainage events occurred (although other drainage configurations are possible), with the second event seemingly enlarging existing valley cross sections. Anastomosing patterns are observed at some locations in the valley headwaters (Fig. 19c, ‘λ’).

Drainage topology in Zone II is weakly dendritic, with incised valleys intercalated with shallow basins, as shown in Fig. 19a, b and d and a much lower drainage density (∼0.19). This drainage zone originates on the same massif, and terminates in a shallow basin with a NNE-SSW facing bounding ridge breached in two different sites (Fig. 19d, arrows). No hummocks, sinuous ridges, or valleys crossing drainage divides are observed in this zone.

Drainage topology in Zone III (Fig. 19a, b and e) ranges from poorly dendritic moving outwards from Batson rim to disorganized and labyrinthine nearing Batson (Fig. 19e). Organized drainage systems in this region drain northwards towards McCauley crater or southwards (Fig. 19a), whereas highly disorganized drainage patterns crudely follow the slope towards Batson crater. Labyrinthine drainage consisting of shallow, poorly defined interconnected valleys connects with the deeply incised glacial valleys flowing eastwards into Batson crater (Fig. 19e, ‘λ’). In Fig. 19e, a series of subparallel valleys are incised along contour lines on the rise shown in Fig. 19e (‘ν’) terminating into the larger depression shown at the bottom of the image, with a flow direction more conformant to local slope. The east-facing slope of the rise is

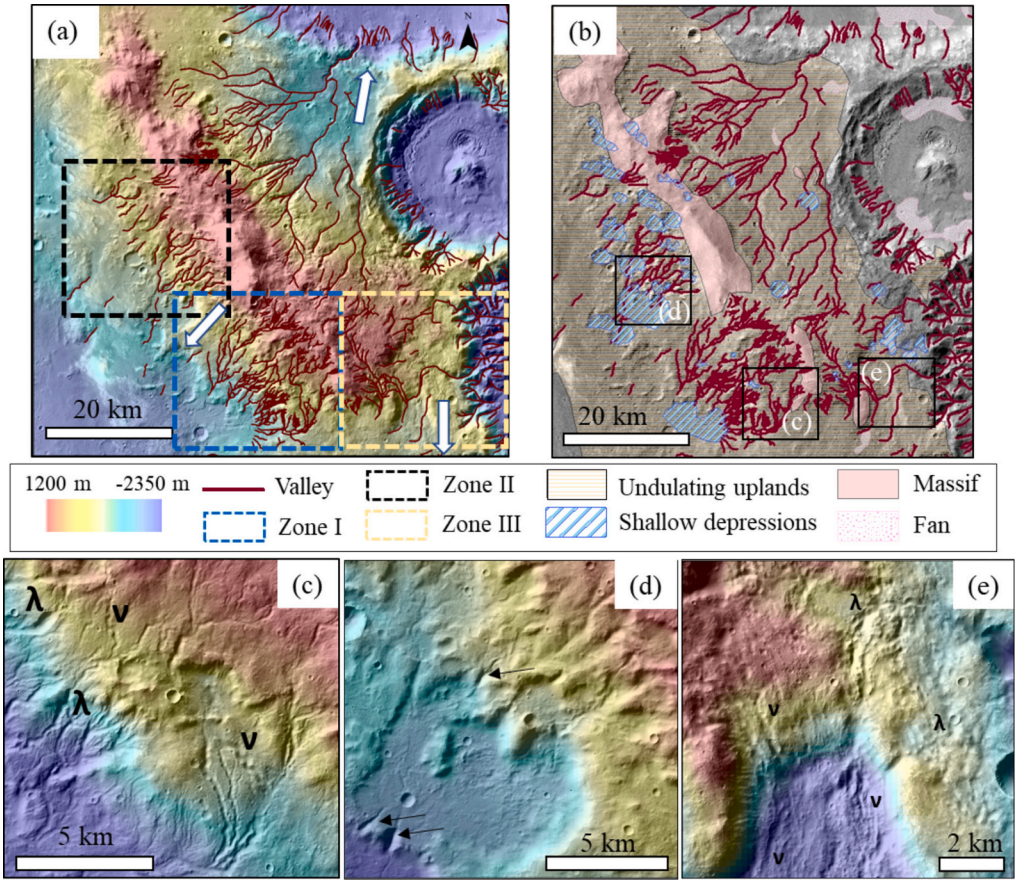

Fig. 19. Western uplands drainage. (a) Topography and main drainage directions (arrows) of the uplands directly west of Batson crater, showing drainage Zones I-III. (b) Mapped main geomorphic elements and valley axis, highlighting the differences in drainage direction, topology, and drainage density in drainage Zones I-III, and the location of insets (c-e). (c) Inset exemplifying drainage in Zone I showing organized, dendritic valleys with occasional interconnections 'λ' and flow direction discordant with topography 'ν'. (d) Inset exemplifying the drainage in Zone II showing shallow depressions connected by narrow valleys (arrows). (e) Inset showing drainage patterns in Zone III, characterized by contour draping parallel valleys discordant with slope (ν), shallow, parallel, short valleys incised downslope, and highly disorganized, interconnected labyrinthine drainage (λ). See section 4.8 for details.

incised by regularly spaced chutes shown in Fig. 19e, which terminate in the contour-aligned valleys.

4.8.1. *Interpretation*

Several elements characteristic of subglacial drainage are visible in drainage Zones I and III, and highlighted in Fig. 19: discordant valleys ('ν'), multiply connected valleys ('λ') In addition, there are instances of valley cross-section variations that are uncorrelated with both tributary junctions (increased input should be reflected in increased area) and location within the network (proximity to the drainage divides should lead to smaller water supply and thus smaller areas), or that vary by 50% along a tributary-less single channel (Fig. 19c).

Terrestrial labyrinthine terrain, as an analogue to drainage in Zone III, are found on Devon Island associated with subglacial channel headwaters and (Fig. S11b) or immediately downstream of a glacier as in the Labyrinth, Antarctica (Fig. S11c). Poor drainage direction in drainage Zone III, (Fig. 19e, '2') could be a sign of weak or competing hydraulic gradients and high subglacial water pressures in this region weakly enclosed by topography. By contrast, labyrinthine drainage landscapes carved in rock, or standing on slopes as is the case of Fig. 19e, are really rare in fluvial environments where the slope would quickly lead water flow into a more organized, parallel or dendritic topology. In addition, valleys incised along contour lines wrapping around existing topography (Fig. 19e, 'ν', Fig. S11d, yellow arrow), could correspond to lateral meltwater channels, often found in association with other glacial landforms (Greenwood et al., 2007; Syverson and Mickelson, 2009). Lateral meltwater channels are ice marginal channels, typically found in association with cold or polythermal-based ice masses on Earth, (e.g., Greenwood et al., 2007; Syverson and Mickelson, 2009) that wrap around former ice margins. By contrast, drainage Zone II (Fig. 19d) does not display any characteristics distinctive of subglacial channelization, and thus we cannot rule out surface runoff other than by environmental context.

5. Discussion

5.1. *Summary of interpretations*

When considered separately, the landforms of the interiors and exteriors of craters in the mapped region may be explained through multiple formative processes. These are summarized in the truth table below, spanning formative hypotheses for key landforms discussed in previous sections.

Following the individual landform analysis summarized in the Table 4, we argue that this suite of landforms is best explained as a record of extensive Amazonian glacial, glacio-fluvial, and glacio-lacustrine processes, acknowledging this is of course, the result of many processes including cratering, previous fluvial activity, and eolian cover, among others.

The resulting assemblage of landforms is presented in a geomorphological map in Fig. 20: Major "Incised Valley" host remnant "Glacial Deposits" of formerly thicker and more extensive glaciers. "Depositional

Table 4
Landforms discussed in the paper (left), list of possible environments of formation, confidence in our interpretations, and reference sections. X indicate that the given environment cannot produce that type of landform.

Environment/ Landform	Glacial	Fluvial/ lacustrine	Geology/ tectonics	Cratering	Mass wasting	Interpretation	Confidence	Section
Glacial deposits	debris-covered glaciers	X	X	X	X	debris-covered glaciers (GLF)	high	3.1
Supraglacial block clusters	glacial transported boulders	fluvial transported boulders	X	ejecta blocks	landslide deposits/ molards	glacial transported boulders	high	3.1.1
Transverse ridges	glacial moraines	sediment bars	wrinkle ridges	X	X	glacial moraines	high	3.2
Fresh shallow valleys	supraglacial channels	proglacial channels	X	X	X	proglacial channels	medium	3.3
Broad shallow troughs	tunnel valleys/ subglacial channels	proglacial channels	X	X	X	tunnel valleys/ subglacial channels	low	3.3
Depositional aprons	outwash fans / ice deposit	alluvial fans/ deltas	subsurface structural deformation	X	landslide deposit	outwash fans/ ice deposits	medium	3.4.2
Basinward scarps	extant glacier termini	delta front/ lake level	basin boundary fault	X	mass wasting deposit edge	lake level	medium	3.4.2.1
Crater wall parallel ridges	glacial striae	grooves due to turbulent sheet flow	bedrock stratigraphy	ejecta blanket	ridged landslide deposits	glacial striae	high	3.4.3
Crater wall benches	X	lake level	bedrock layer outcrop	X	mass wasting deposit edge	lake level	low	3.4.4
Pancake/ step deltas	ice-contact or subglacial delta	delta/ alluvial fan	X	X	X	subglacial fan/delta	medium	3.4.5
Undulating plateaus	degraded older outwash deposits	degraded older alluvial fans	impact basin sediments	Ejecta blanket	Solifluction lobes	degraded older outwash deposits	low	3.4.6
Multiply connected valleys	subglacial channels	braided/ anastomosing channels, low energy	X	fluidized ejecta	X	subglacial channels	high	4.1
Discordant valleys	subglacial channel	lake breach floods/ post-emplacement modification	X	fluidized ejecta	X	subglacial channels	high	4.2
Shallow depressions	inter- connected subglacial cavities	connected lakes / thermokarst	structurally controlled basins	primary rim topography	X	interconnected subglacial cavities modifying primary rim topography	high	4.3
Hummocky material	glaciofluvial hummocks & murtoos	catastrophic flood deposits	X	molards	landslide	glaciofluvial hummocks & murtoos	high	4.4
Linear troughs	grooves / GHC	grooves incised by floods	graben	ejecta	longitudinal ridges	glaciofluvial hummocky corridors (GHC)	high	4.4
Navua Valles	subglacial channel	river valley	X	X	X	river valley with subglacial reactivation	high	4.5
Sinuous ridges	esker	inverted channel	wrinkle ridge	X	X	esker/ inverted channel	High/ medium	4.6
Southwestern broad valleys	glacial and tunnel valleys	sapping/ river valleys	X	X	X	glaciers/ tunnel valleys	medium	4.7
Western uplands valleys	subglacial channel networks	river channel networks	X	X	X	case by case	medium	4.8

aprons" are sedimentary deposits, perhaps ice-rich, formed from glacial outwash and possible contributions from pre-glacial crater wall incision. "Ridges on the depositional aprons" and elsewhere on basin floors are interpreted as channelized fluvial deposits presently in inverted relief. The "Basinward Scarps" mark rounded scarps on the depositional aprons that may mark the termini of glacial advances. "Transverse Ridges" are interpreted as glacial moraines. "Depositional Apron Depressions' lie at the foot of the basinward scarps and are possibly excavated by subglacial runoff. "Fresh Shallow Valleys" are sinuous, shallowly-incised, narrow valleys mostly excavated by late-stage glacial runoff. "Crater Wall Benches" in Nako and Salkhad craters likely record narrow zones of erosion and deposition during former crater lake highstands. "Fluvial Deposits" include relatively late-stage sediment deposited as channel deposits of Navua A Valles, pancake deltas, deposits by fresh shallow valleys, and other crater exterior and interior fluvial sediment. "Hummocky Material" are patches of low mounds that are likely erosional or depositional products of high intensity subglacial runoff. "Sinuous Ridges" in crater interiors and the southeastern Batson crater are likely esker ridges, although we cannot discard channel inversion inside Nako crater. Additional small, unmapped sinuous ridges occur along Navua A Valles and in valleys on the southeastern flank of Batson crater. "Broad Valleys" are about 1 – 4 km wide and up to 400 m deep mantled by light-toned deposits; the valleys may be glacially scoured. See Table 2 for figures showing the mapping units and Table 4 for text sections where the units are discussed. "Undulating Plateaus" mostly surround the central peaks of Batson and Jori craters and may be sediment or glacial ice sourced from the central peaks.

5.2. *Timeline of events and glacial stages*

We establish a timing of events based on three aspects: age dating from crater counting, our own results complemented with previous mapping; a relative age dating to associated landforms based on cross-cutting relationships; and a regional relative age dating with respect to the light toned unit (LTU), dated ~ 1 Gyr (Howard et al., 2021), and which represents an ice-free episode. Crater counting results are

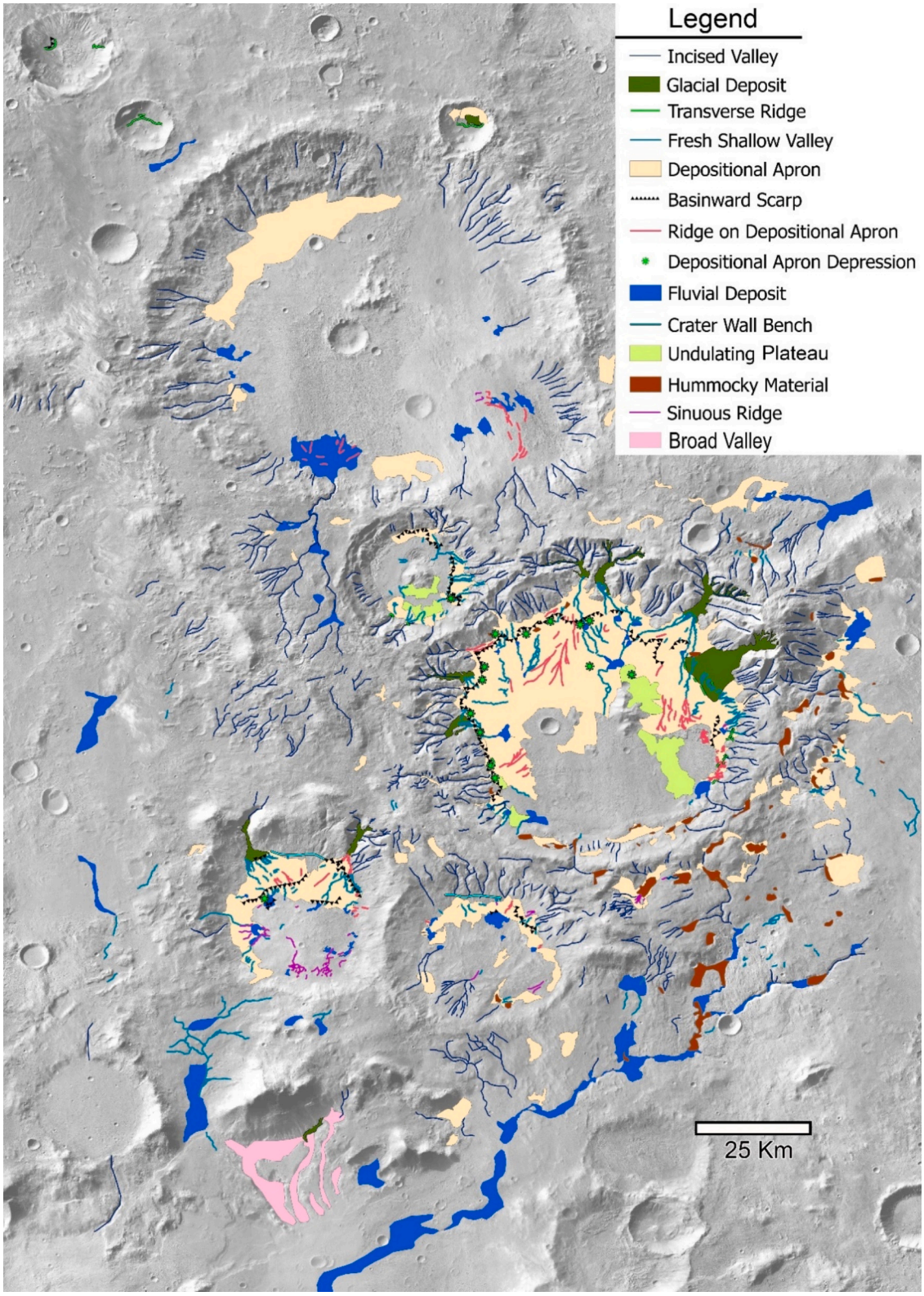

Fig. 20. Geomorphic map of fluvial, glacial, and glaciofluvial landforms. See Fig. S1 for a map of non-fluvial or glacial units of crater floors.

discussed below, whereas individual cross-cutting and relative timing relationships are presented together with the landform description and interpretation. A synthesis of this information is presented in Fig. 21. The following discussion is based on the model ages of crater counts in Table 5 using the Hartmann and Neukum (2001) production function for compatibility with Howard et al. (2021), Zhang et al. (2023) and other age dating for the same region. The Hartmann and Daubar (2017) estimated ages average 36 percent greater than the Hartmann and Neukum (2001) ages using craters in the 30-500m diameter range.

The reliability of planetary surface crater retention age dating using the size distribution of impact craters depends greatly on the size of the geomorphic surface being dated. The established crater counting

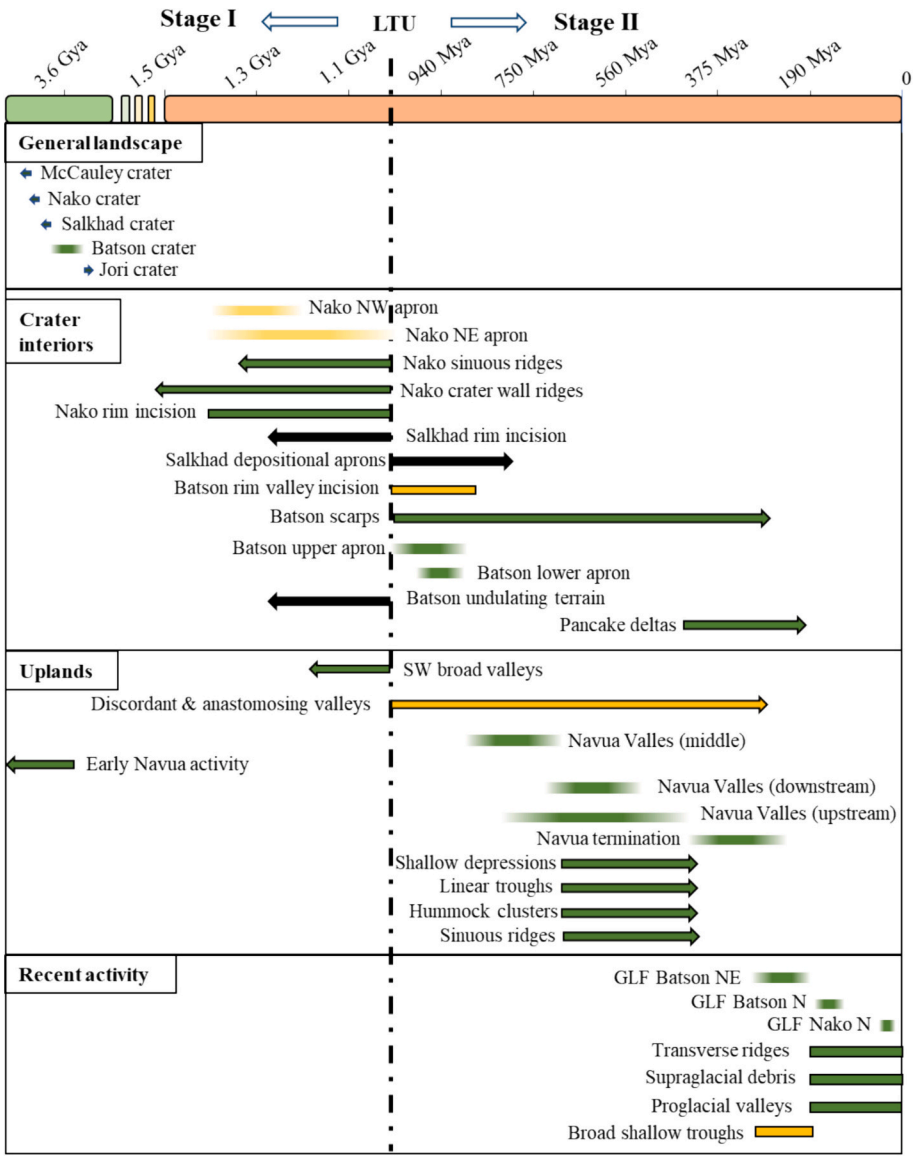

Fig. 21. Absolute and relative ages of the key landforms discussed in this study on a timeline (top), divided by the general landscape (top box), crater interiors, crater uplands, and recent activity. Absolute ages derived from crater counting are presented as diffuse bars, centered on the reported age and with length corresponding to error bounds. Relative ages are shown with arrows when only one cross-cutting relationship could be established, or as bars when pre-dating and post-dating relationships could be established. The light toned unit (LTU) is shown as a regional relative timing marker with a dashed black line (See Fig. S17 for instances of exposure). Confidence is shown in color scale: green is high, yellow is medium, black is low.

procedure that we employ (Michael and Neukum, 2010) provides an estimate of age uncertainty as a function of sampling area as reflected in Table 5, and Figs. S14 and S15. Recent studies (e.g., Warner et al. (2015) and Palucis et al. (2020)) have suggested that error bounds on ages using small craters on small geomorphic surfaces are underestimated by Michael and Neukum (2010). Many of our count areas are well below the minimum of 100 km^2 suggested by Warner et al. (2015). We accepted crater counts only if the cumulative curves closely followed a production function. In addition, for several geomorphic surfaces we broke the count areas into two or three subsamples to test for consistency in derived ages (Batson exterior crater ejecta, Navua A Valles floor, and the ejecta of the 4.6 km diameter crater superimposing Navua A Valles). Finally, we examined derived ages for self-consistency with interpreted geomomorphic relative ages, including, e.g., surfaces mantled with the light-toned deposit dating older than those without. Relative surface ages and sequences of events are better established than absolute ages, which depend upon the selected production function (e.g., Hartmann and Neukum, 2001; Hartmann and Daubar, 2017). We find that the estimated age dates provide a consistent interpretation of geomorphic events in the study area

5.2.1. *Crater counting results*

Table 5 presents crater counting ages, and crater count curves are presented in the Supplemental Information (Fig. S14 and S15).

The inferred age of Batson crater obtained here, of ~3.55 Ga, broadly agrees with the crater age estimate of 3.6 Ga estimate by Hargitai et al. (2018a) (both counts disagree with the age dates in Zhang et al. (2023)), with the Jori crater impact closely following the Batson impact. To account for interpreted glacial erosion affecting craters in the region, the age dating in Fig. S14 utilizes only craters > 1 km diameter, which are less likely to have been eradicated.

The mapped landforms superimposed on the five >25 km diameter craters (Fig. 20) largely post-date the Jori impact (Fig. 21). The geomorphic history of the study area from the Early Hesperian through most of the Early Amazonian is uncertain until the emplacement of the depositional aprons in Nako crater at about 1.3 Ga. In the equatorial

Table 5
Summary of crater-count surface age dating in the study area. Crater counting used the Crater tools add-in for ArcGIS (Kneissl et al., 2011) and the CraterStats 2 software (Michael and Neukum, 2010) for age dating. Number of craters indicates the subset of mapped craters used to fit the cumulative age curves.

Location	Number of Craters[d]	Count Area, km^2	Crater diameter range, m	Estimated Age, Ma[e] (HN)	Estimated Age, Ma[f] (HB)
Batson crater ejecta, NE sector	13	5651.9	10^3 - 10^4	μ3500±100	μ3400+90-200
Batson crater ejecta, SE sector	12	5331.9	10^3 – 10^4	μ3400±150	μ3300+100-500
Batson crater lower depositional apron[a] (BDL)	1324	1002.6	100-500	μ930±30	μ1200±30
Batson crater upper depositional apron[a] (BDU)	619	382.1	100-400	μ980±40	μ1300±50
Batson crater NE interior glacier[b] (BGNE)	24	75.5	100-500	μ240±50	μ320±60
Batson crater N interior glaciers[b] (BGN)	45	36.1	60-500	μ150±20	μ220±30
Nako crater NW depositional apron[a] (NDW)	387	186.3	100-500	μ1340±67	μ1720±86
Nako crater NE depositional apron[a] (NDE)	39	68.3	150-400	μ1250±200	μ1540±240
Nako crater interior glaciers[b] (NG)	15	11.0	30-100	μ22±6	μ40±10
Jori crater upper depositional apron[b] (JD)	70	34.9	80-300	μ610±70	μ880±100
Navua A Valles upstream reach[b] (NAU)	11	56.4	150-500	μ590±200	μ730±200
Navua A Valles middle reach[b] (NAM)	42	110.7	150-500	μ790±100	μ970±100
Navua A Valles downstream reach[b] (NAD)	15	57.5	150-500	μ620±100	μ800±200
Ejecta of 4.6 km diameter crater superimposing Navua A Valles[c] (NSC)	24	58.2	100-350	μ250±50	μ330±70
	30	56.8	100-350	μ360±50	μ490±90

[a] Plots and counting regions as in (Howard et al., 2021), but adjusted by the cumulative resurfacing correction. Parenthetical letters refer to count plots in Fig. S15.
[b] Plots in Figs. S14 and S15.
[c] Separate counts on the eastern and western halves of the ejecta blanket.
[d] Number of craters included in age estimation.
[e] HN: Uses the Hartmann and Neukum (2001) production function.
[f] HB: Uses the Hartmann and Daubar (2017) production function.

latitudes of Mars this "missing" interval corresponds to the main epoch of alluvial fan formation (Morgan et al., 2014; Morgan et al., 2022).

Fig. 21G indicates that at least two different glacial advances took place, separated in time by an ice-free event marked by the deposition of a regional mantling light toned unit (LTU), which occurred roughly ~ 1Gya (Howard et al., 2021). At least two episodes of glaciation are a self-consistent result of comparing crater ages, derived here and in the literature, with relative age dating using exposures of the LTU.

A first stage of glaciation (stage I) spanned the SW of our region of interest, and included Nako and possibly Salkhad craters. This is supported by LTU mantling on the depositional aprons on the north of Nako crater, on Nako crater floor sinuous ridges, exposures on Nako and Salkhad crater wall parallel ridges, and less clear markers on benches exposed in Salkhad crater. The southwestern broad valleys, located SW of Nako crater (Fig. 18) and interpreted to be tunnel valleys or other large-scale glaciofluvial drainage corridors, are also mantled by light toned deposits. It is not possible to establish whether these landforms are all linked to the same glacial advance as we could not establish clear cross-cutting relationships between the southwestern broad valleys and Nako landforms. We refer to this event as glacial stage I, pre-dating LTU (>1 Gya in Fig. 21).

A post-LTU glacial advance (stage II) expanded to cover a larger area, possibly defining a regional maximum. This stage includes Batson crater and crater rim glaciation, glaciation on the uplands south and east of the crater at least to the Navua A Valles (most likely beyond), glaciation on the eastern Salkhad rim, subglacial incision or reworking of valleys located on the massif west of Batson, and a likely ice-covered Batson crater lake, dated from LTU to <190 Ma, before the emplacement of crater floor FSV. Lower Nako crater depositional aprons, and ridge-wall sculpture on Salkhad western crater wall were not appreciably reworked by glacial or fluvial activity after the light-toned deposition event, but the situation on Salkhad depositional aprons and benches is less clear, with evidence for both pre- and post-LTU emplacement activity discussed in section 3.4.4. The situation at Jori crater is even less clear. Blocky material is limited to the very top of the depositional apron, but the apparent crater-date age of the depositional apron is only 0.6 Ga (Fig. S15). The Jori depositional apron is, however, mantled by eolian sediment, which in places obscures craters and makes surface ages dates unreliable.

South of Batson crater, a cluster of surface ages occurs at ~ 0.6 Ga, including the glaciofluvial activity in Navua A Valles. This appears to mark the cessation of glaciofluvial activity from the glacial complex on the Batson crater southeastern exterior rim and probably also corresponds to formation of the FSVs on the Batson crater depositional apron and those in Jori crater. This termination age is consistent with the constraining ~0.3 Ga age of the 4.6 km diameter crater superimposed on Navua A Valles.

A big question mark is the relationship between the youngest glacial landforms (GLFs, FSVs) and the earlier regional maximum. Facing a lack of clear evidence, we adopt the easiest interpretation that the most recent glaciation (last 350 Myr in Fig. 21) simply reflects the retreat of the previous larger ice cover, with south crater rims (equator-facing) undergoing deglaciation before pole-facing slopes, where extant ice deposits are still located. We acknowledge, however, that several episodes of glacial advance and retreat may have occurred in the region owing to the obliquity variability timescales (e.g., Laskar et al., 2004; Forget et al., 2006), which are chaotic, but on average much shorter than the span of the two individual glacial stages we were able to distinguish.

In summary, the time period between the ~3.6 to 3.8 Ga Batson crater impact and the oldest depositional aprons (~1.3 Ga) possibly hosted several moderate epochs of snow and ice accumulation, for which we have no direct evidence. The period between the emplacement of the Nako aprons (~1.3 Ga) and the termination of Navua A Valles activity (~0.6 Ga) experienced the greatest glacial and glaciofluvial activity with two different glacial advances, and active subglacial fluvial and possibly lacustrine activity. Subsequent to 0.6 Ga, subglacial meltwater flow from the ice cover on the Batson crater southeastern exterior slopes ceased along Navua A Valles, and glaciers in the interior of the craters gradually waned by sublimation and minor meltwater generation. Glacial like forms (GLFs) on pole-facing slopes and possibly the upper depositional aprons in the crater interiors still contain remnant glacial ice.

5.3. *Glaciation extent, dynamics, and environments*

Ice flow direction, mapped by glacial landform type and direction, is a useful paleo-environmental indicator of the extent, thermal state, and ice flow rate and direction. Thick ice deposits flow and erode following largely ice-surface slope gradients (Cuffey and Paterson, 2010), whereas

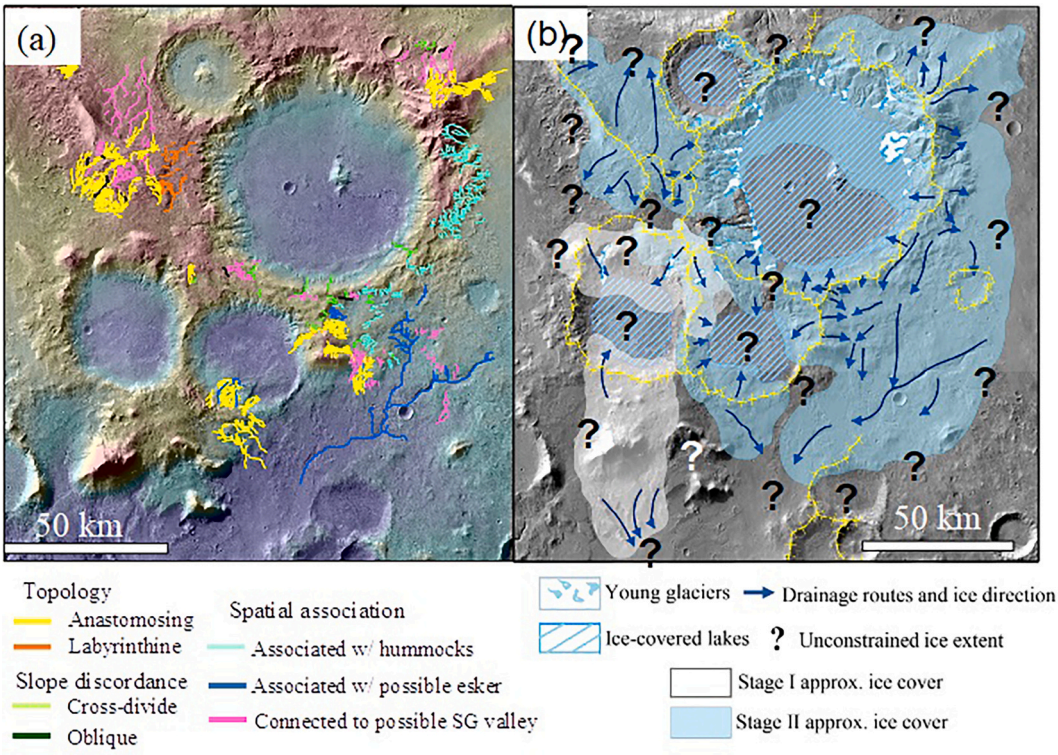

Fig. 22. Main drainage routes and inferred ice extent on the crater uplands. (a) Valleys that display one or more attributes distinctive of subglacial erosion, color coded by distinguishing attribute. (b) Approximate inferred extent of ice cover for stage I (white) and stage II (blue) glacial advances, as well as current GLF deposits ('young glaciers'), based on age dating of interpreted glacial landforms and their direction. Boundaries are highly speculative (marked '?'), and ice thickness is unconstrained. The interior of the craters may have hosted ice-covered lakes or subglacial lakes. Main drainage divides are shown in yellow.

thinner deposits tend to have stronger topographic controls.

5.3.1. Inferred glacial cover and flow direction

Landform distribution and orientation belonging to Stage I indicate that Stage I ice flow was roughly organized N-S (Fig. 22b, white unit). On Nako crater, early glaciation may have flowed from the north basinwards from the rim, forming Nako pre-LTU depositional aprons, and from the southern rim basinwards, incising anastomosing valleys and depositing sinuous ridges. The massif to the south of Nako crater is a likely glacial accumulation zone for ice to flow southwards into the southwestern broad valleys.

LTU mantled crater-wall parallel sculpture on the western wall of Salkhad crater indicates two generations of erosive activity, both interpreted to be glacial scour (Table 2). The first is oriented WNW-ESE basinwards into the crater floor, whereas the second is oriented NNW-SSE, with neither displaying observable continuation across the Salkhad rim into Nako crater. The absence of crater wall parallel sculpture across the Nako-Salkhad rim or marked rim erosion suggests that ice flow did not scour across this divide, following instead topography basinwards into Salkhad crater. Hence a possible configuration of ice pre-LTU could have extended to the N and NE of Nako crater rim, flowing basinwards into Nako crater from the north and east, and spilling into Salkhad crater. A second body of ice pre-LTU could have been located on the massif south of Nako crater, occasioning the valleys flowing into Nako crater, and the SW broad valleys south from the massif. Identified stage I landforms generally conform to topography, suggesting the ice cover was localized to this massif and the north of Nako crater rim.

Ice flow direction in Stage II (post-LTU) indicates a much more generalized NNE-SSW direction not necessarily conforming with topography (Fig. 22b, blue unit). This is visible in the orientation of landforms in Batson crater, on the uplands east and south of Batson crater and east of Salkhad crater, notably in the drainage direction of shallow depressions, hummocky infill of inferred GHCs, divide-crossing channels, and depositional apron distribution (Fig 22b, arrows on the blue unit).

The spatial distribution of the glacial landforms inferred on Batson crater south and east uplands, as well as their overlapping relationships, suggest the following causal association. Isolated, disconnected shallow depressions naturally occurring on the crater rim would be partially filled with subglacial meltwater, which would increase in pressure following the input of surface melt up to a critical threshold, where they would become connected. Meltwater then would flow between these depressions ('linked subglacial cavities') at high water pressure and high discharge, routing towards the S, producing hummocky fill (Vérité et al., 2023). As water pressure decreased and discharge increased, drainage became more organized into the inferred glaciofluvial hummocky corridors, to drain into the Navua A Valles. Meltwater in the Navua A Valles subglacial channel would have flowed at high discharge to the ice margin. Whereas our work did not identify a candidate ice margin in the study site, further work will follow the Navua Valles system to identify possible ice marginal features.

The depth and density of valley incision exhibits a strong asymmetry in Batson, Salkhad, and Nako craters, such that south-facing interior rims are incised to a much greater extent than north-facing rims (Figs. 1, 20). Either or both relief and climatological factors might contribute to this pattern. The southern sections of the rims of these craters have lower relief relative to the north rims. Rim relief has been identified as contributing factor to the incision of valley walls creating alluvial fans (Moore and Howard, 2005; Wilson et al., 2021; Morgan et al., 2022). Jori crater incision is greatest on the southeastern crater interior wall where the relief is enhanced due to superposition of Batson and Jori crater rims. McCauley crater has only modest rim incision, however, despite the relief of the northern rim equaling or exceeding that of the north walls of Batson, Nako, and Salkhad craters. Rim orientation, rim relief, orbital parameters such as obliquity, and latitude, all play a role in

determining solar insolation conditions, which may enhance ice and snow melt on south-facing slopes (e.g., Clow, 1987) and facilitate ice erosive activity.

In addition to the two stages, two styles of glaciation are inferred: (1) crater rim glaciers (Alpine-style glaciation), characterized by cirques, deeply-incised valleys, moraine ridges, and proglacial systems (shown as 'Young glaciers' in Fig. 22b). (2) Plateau glaciers/ice caps, extending beyond and above craters onto the uplands (shown as colored polygons in Fig. 22b). In Fig. 22b, we inferred ice cover and ice boundaries from the presence and direction of subglacial pathways shown in Fig. 22a. Meltwater drainage routes follow ice surface slopes, which in turn should be roughly perpendicular, and appear in proximity to the ice margin. Note that the interior lakes of all craters may have been covered by thick glacial ice, implying a much more extensive, regional glaciation, or maybe perennially ice-covered lakes implying much more localized ice extent. We cannot differentiate one from the other case with our current observations, so we chose the second, more conservative scenario. These subglacial meltwater landforms indicate this areally extensive glaciation was at least partially warm or polythermal-based, whereas the three types of meltwater routes identified inform the nature of the subglacial hydraulics.

The basal melting of the inferred glacial ice formerly covering portions of the study region may have been enhanced by a high regional geothermal gradient. (Levy et al., 2017) identify a 400 m deep depression in the center of the ice-covered floor of Jori crater (Fig. 1), which they attribute to a local subsurface geothermal source inducing melting and collapse of the ice. They also identified a smaller collapse feature on the floor of Salkhad crater. Butcher et al. (2017, 2021), and Gallagher et al. (2021) implicate elevated geothermal heating to explain formation of eskers in other locations on Mars. Warmer ice may have in turn enhanced strain rates and internal frictional strain heating, contributing to melt production (Cuffey and Paterson, 2010).

Glaciation was locally extensive, but was likely not part of a large continental ice sheet complex. This hypothesis is supported by two factors: McCauley crater to the north or Jori crater has been only modestly affected by glacial activity. Also, there is significant variability in the subglacial drainage directions around Batson crater, suggesting either temporal variations on drainage direction, or most likely ice surface slope influenced by local rather than regional basal topography. The obvious influence of the main drainage divides on the subglacial drainage directions (Fig. 22b, yellow lines) further support smaller ice caps instead of a large-scale ice sheet. Ice retreat, starting roughly ~0.6 Ga ago, followed plateau style glaciation and remnant ice deposits retreated to the crater rims and originated Alpine-style crater rim glaciers.

5.3.2. *Subglacial environments and terrestrial analogues*

Table 4 presents landforms belonging to a range of glacial and subglacial environments, from very high to low energy. Depositional aprons, basinward scarps and crater wall benches, as well as pancake deltas, suggest the presence of an ice-covered lake, perhaps subglacial, inside Batson, Nako and Salkhad craters. Subglacial and ice-covered lakes are commonly found under ice sheets and ice caps on Earth, with Lake Vostok under the Antarctic ice sheet being the most obvious example. Depending on their degree of connection with the subglacial drainage system, subglacial lakes make be seasonal, filling and draining with the availability of surface meltwater, or stable over millions of years.

Stable subglacial lakes define a generally low energy system, albeit with pressurized water input events characterized by discharges comparatively larger than open or ice-covered lakes with outlets. Ravier et al. (2014) described a terrestrial subglacial delta in Ireland hosting sediments ranging from planar parallel-laminated and ripple cross-laminated sand to massive and normally graded gravel, describing a higher energy environment than characteristic of open lakes. A similar environment could have characterized an interior lake in Batson, Nako and Salkhad craters. Glacio- lacustrine environments such as in Batson crater define potentially habitable environments well into the Amazonian period on Mars, with terrestrial subglacial analogue lakes known to host microscopic life forms (Abyzov et al., 2001).

Fig. 23 illustrates a possible state of glaciers and ice-covered lakes in and southeast of Batson crater at the maximum extent of glacial activity

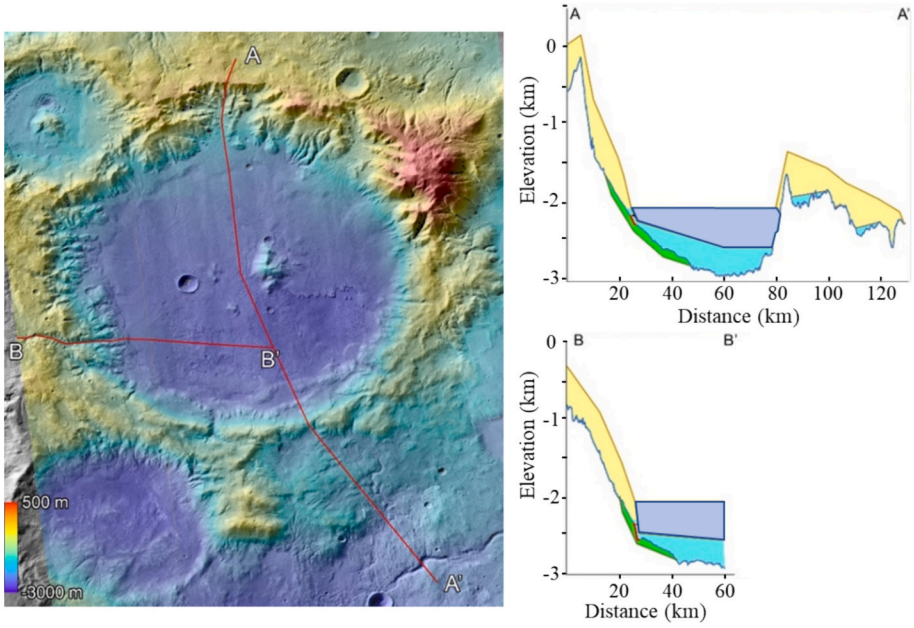

Fig. 23. Concept of ice conditions at time of formation of depositional apron scarps in and south of Batson crater along profiles A-A' and B-B', with the present land surface indicated by blue lines. Glaciers are yellow, lake ice is dark blue, sub-ice lakes are blue, depositional apron sediment is green (thickness uncertain), and depositional apron scarps are red. Where ice surface is sloped glacial ice is present, with episodic basal meltwater feeding into the lake (not illustrated). In the center of Batson crater an ice-covered lake is postulated, with spatially-varying ice thickness of up to 400 m. The apron scarps are interpreted to be formed by sedimentation at the boundary between glacial ice and lake ice cover. The local depressions at the foot of the apron scarps (arrows) may be formed by scour by subglacial drainage into the lake. Subglacial lakes are also inferred to be present in depressions on the southeastern exterior flank of Batson crater.

during stage II. The interior and exterior crater slopes are hypothesized to have been under a thick ice cover. In the interior of Batson crater, crater rim glaciers terminated at an ice-covered lake. Shallower basins on the exterior slopes hosted subglacial lakes. Basal runoff from the glaciers on the interior crater rim helped to incise the deep rim valleys and contributed sediment to the upper parts of the depositional aprons. The apron scarps (red lines along profiles in Fig. 23) are suggested to have formed by sedimentation (or possibly erosion of previous depositional apron deposits) at the interface between the glaciers and the ice-covered lakes. The shallow depressions basinward of the scarps ("*"s in Fig. 20) may have been excavated by subglacial runoff feeding into the lake. Batson crater is a nearly closed hydrological system. Subglacial runoff would have raised the level of the basin-center lake, encouraging sediment deposition on the depositional apron at and upstream of the interface between the glaciers and the lakes, thereby creating the elevated depositional apron and associated scarps. The ~300 m difference of apron scarp elevations within Batson crater (Fig. 8) are suggested in Fig. 23 to result from areal differences of the elevation of the ice-water elevation within the basin-central lake, as discussed in section 3.4.2.1. Subglacial overflows of enclosed basins on the exterior rim of Batson crater (right side of profile A-A' in Fig. 23) resulted in the excavation of subglacial valleys, general fluvial scour and formation of blocky material.

Contrastingly, the suite of landforms composed by the connected and isolated shallow depressions on Batson crater rim, and the shallow troughs filled by hummocks on the uplands southeast of Batson crater, interpreted as subglacial interconnected cavities and glaciofluvial hummocky corridors (GHC) respectively (Table 4), exemplify high energy environments. GHC and interconnected subglacial cavities are both fingerprints of hydraulically connected distributed subglacial drainage systems (Lewington et al., 2020; Simkins et al., 2023; Vérité et al., 2023). Drainage dynamics in GHCs, including discharge, pressure gradients, connectivity, and the resulting sedimentary record, are intimately linked to meltwater availability and bed properties (Schoof, 2010; Ojala et al., 2022; Vérité et al., 2023). GHCs could also originate as focused subglacial flood events following water release from a subglacial water body (Sharpe et al., 2021; Shaw, 2002). Fig. 16c shows a detailed image of these hummocks (arrows), which display a hydrodynamic lee/stoss asymmetry and in occasions an angular shape (arrows). This morphology suggests that these hummocks could in fact be murtoos, V-shaped subglacial hummocky landforms associated with large subglacial meltwater fluxes formed by till deposition and sedimentation from meltwater with subsequent deformation, likely from supraglacial input during periods of enhanced meltwater supply (Peterson et al., 2017; Peterson and Johnson, 2018; Vérité et al., 2023). Inferred GHCs and connected cavities in the region thus may be relicts of a time-transgressive, subglacial drainage system, evolving to accommodate larger meltwater inputs and higher discharges and pressures (Vérité et al., 2023).

Subglacial interconnected cavities, identified here as shallow depressions partially infilled with hummocks and poorly connected with neighboring depressions, develop when subglacial water drainage accumulates in points of minimum hydraulic potential, which can occur due to local depressions (Flowers, 2015; Livingstone et al., 2022). Subglacial cavities store basal meltwater until the lake hydropotential seal breaks, which can occur either by increased water pressure or by enhanced cavity leakage. At this point cavities become an active supplier of highly pressurized water, flowing at low discharges in weakly connected meltwater corridors and orifices (Kamb, 1987; Flowers, 2015). On another hand, glaciofluvial hummocky corridors on the southeastern Batson exterior rim are part of the subglacial hydraulically connected distributed drainage, supplying more efficient drainage than linked cavities, and less efficient drainage than subglacial channels, and represented by very high discharges and high water pressures (Lewington et al., 2020). Finally, subglacial channels constitute efficient, channelized drainage systems under ice covers, characterized by low pressure and high discharge (Figs. 13-18, 21, S12). Both subglacial channels and glaciofluvial hummocky corridors represent high and very high energy environments.

5.3.3. Earth-Mars glacial hydrology comparison

Evidence for any former presence of regional glaciation on Mars is likely to be cryptic relative to Earth. Many of the distinctive landforms of terrestrial valley glaciers and ice caps would likely be absent or muted in martian glacier systems due to the lower gravity, which greatly diminishes the scouring potential due to decreased ice sliding (Grau Galofre et al., 2022). This includes U-shaped valleys, arêtes, glacial scour features, landforms consisting of glacial till deposition such as drumlins, lineations, moraines, and irregular topography with roche moutonées and depressions. The rims of the larger craters in the study region are often rounded at the kilometer scale, lacking the steep sculpting of terrestrial alpine glaciation. On the other hand, the lower martian gravity reduces glacial flow rates relative to Earth, stabilizing subglacial drainage due to decreased closure and collapse rates of cavities and tunnels (Grau Galofre et al., 2022). Thus, landforms resulting from subglacial meltwater erosion and glacio-fluvial deposition may provide the strongest evidence for former glacial extent.

5.4. Comparison with other studies of martian ice-related landform evolution

Whereas there is ample direct and indirect evidence for glacial episodes throughout Mars history, from modern viscous flow features to ice accumulation climate models, relatively few studies have addressed the role of ice in modifying the host terrain. An exception to this has been the controversial suggestion that melting of Noachian/Early Hesperian equatorial ice sheets has been responsible for excavating the valley networks, based on the difficulty for atmospheric modeling to create a warm enough climate to produce rain (e.g., Head and Marchant, 2014; Grau Galofre et al., 2020). Networks of broad, sinuous ridges occur on the floor of dozens of craters in the equatorial region (e.g., Boatwright and Head, 2023). Unlike the narrow sinuous ridges we attribute to formation as eskers, equatorial crater floor ridges are organized into networks indicative of erosional inversion of fluvial deposits (Davis et al., 2019; Boatwright and Head, 2021, 2022a, 2022b, 2023; Gullikson et al., 2023). Boatwright and Head (2021, 2022b) attribute the deposits forming through top-down melting of cold-based glaciers on the crater rims during the Noachian/Hesperian boundary. Bouquety et al. (2019, 2020) identified possible cirques in crater interiors and proglacial valleys on crater exterior slopes in the equatorial highlands based on valley and headwall morphometry. Rather than top-down melting, they suggested fluvial runoff from polythermal ice caps on uplands and crater rims during the Noachian/Hesperian transition. By contrast, Boffo et al. (2022) conclude that subglacial runoff could have occurred beneath equatorial ice sheets if the geothermal gradient was sufficiently high. In the mid to high latitudes evidence for subglacial runoff from this age is more definitive. Numerous eskers are exposed at high southern latitudes in the Dorsa Argentea Formation, dated 3.4-3.8 Ga (e.g., Howard, 1981; Head and Pratt, 2001; Butcher et al., 2016) and the floor of the Argyre basin, dated ~3.6 Ga (e.g., Banks et al., 2009; Bernhardt et al., 2013).

Several studies have identified eskers emerging from sublimation of Amazonian ice deposits (Gallagher and Balme, 2015; Butcher et al., 2017, 2020, 2021; Gallagher et al., 2021; Woodley et al., 2022), confirming wet-based glacial activity. Gallagher et al. (2021) also suggest the presence of tunnel valleys in the Phlegra Montes as well as glacial basal scour creating whaleback hills, glacial troughs, and parallel grooving.

6. Conclusions

The interiors and exteriors of Batson, Nako, Salkhad, and Jori craters (and McCauley crater to a lesser degree) were extensively modified by

glaciofluvial and glacio-lacustrine activity during the Early to Middle Amazonian, from somewhat before 1.3 Ga. Modifications included dissection of crater interior rims, emplacement of depositional aprons, moderate incision and sedimentation on crater exteriors, and subglacial runoff east to south of Batson crater and through Navua A Valles. Glacial sculpture in crater modification in this region is partly cryptic because of its primary manifestation through glaciofluvial activity. The case for glacial involvement is based on diagnostic geomorphic features:

- Remnant glaciers occur on the interior rims of Batson and Nako craters within deeply incised valley walls. Evidence indicates that these valley glaciers were formerly thicker but have shrunk through sublimation as well as having sourced meltwater that excavated a network of shallow, sinuous valleys into the depositional aprons.
- Incision of the deep valleys on the interior of the craters may have occurred through runoff from snowmelt prior to the main glacial activity, or by glacial and glaciofluvial processes related to glaciation.
- Portions of the headwater channel systems and channels debouching onto crater floors display incised reticulate to anastomosing topology, characteristic of subglaciofluvial incision.
- Distributary sinuous ridges lead from channels draining into crater floors toward the basin interiors: the morphology of these is not distinctive of inverted channels or eskers. Single sinuous ridges occur within valleys draining the exterior slopes of Batson crater and centrally within Navua A Valles. These are best interpreted as eskers.
- Depositional aprons in Batson and Nako craters feature basinward-facing, rounded scarps with ~150 m of relative relief. Narrow benches also occur on the northern lower interior walls of Nako and Salkhad craters. We infer basinward apron scarps to have formed near the contact between glaciers on the crater walls and perennially ice-covered lakes in the crater interior (e.g., Figs. 22, 23).
- Portions of the interior crater walls of Batson, Nako, and Salkhad craters feature crater wall parallel ridges. In Salkhad crater these ridges are parallel over about a third of the western crater wall despite circumferential change in the orientation of the crater wall. We interpret these ridges to have formed by glacial scour toward a basin-center ice-covered lake.
- On the exterior slopes of Batson crater numerous valleys cross divides between depressions. Whereas some of these valleys breach the divides, others have convex profiles when crossing the divide. We interpret these valleys to have formed by subglacial runoff crossing divides under pressurized flows.
- Groups of hummocks occur on the exterior rim of Batson crater, primarily located in relative depressions and within linear troughs draining toward Navua A Valles. Individual hummocks range up to more than 100 m in size. We interpret them as glaciofluvial hummocks within subglacial corridors on the basis of the similarity with terrestrial formerly glaciated terrains.
- A 65 km wide expanse of southeastern exterior slopes of Batson crater between the crater rim and Navua A Valles features linear troughs, parallel with a NNW-SSE orientation that is not radial to Batson crater. Some of these troughs are infilled with hummocks. We attribute this texturing to runoff in glaciofluvial hummocky corridors beneath an ice sheet covering the eastern and southeastern flanks of Batson crater.

We infer that the rims of Batson, Nako, Salkhad, and Jori craters were encased in glacial ice that extended across the interior crater slopes and partway onto the crater floor, interacting with ice-covered lakes in the basin centers (Fig. 22b). The eastern and southeastern exterior of Batson crater were covered by a plateau glacier, which is also inferred to have covered the upland plateau west of Batson crater, extending southward to the Navua A Valles at the southern end of the study area. Basal glacial meltwater, possibly produced by a locally-enhanced geothermal gradient, sculpted many of the fluvial features of the study region. The detailed sequence of glacial extent and glacial runoff is largely uncertain, but likely occurred in at least two episodes of advance. The low martian gravity relative to Earth is the primary reason that past glacial activity on Mars is most likely evidenced by glaciofluvial morphology rather than by direct sculpting by glacial scouring (Grau Galofre et al., 2022). The detailed description of all landforms presented in this paper, their context, distribution, and spatial association are intended to be used as guidance for aiding in the search for glacial and glaciofluvial sculpture elsewhere on the cratered landscapes of Mars.

CRediT authorship contribution statement

Anna Grau Galofre: Writing – review & editing, Writing – original draft, Visualization, Validation, Methodology, Investigation, Funding acquisition, Conceptualization. **Alan D. Howard:** Writing – review & editing, Writing – original draft, Visualization, Validation, Software, Resources, Methodology, Investigation, Funding acquisition, Conceptualization. **Alexander M. Morgan:** Writing – review & editing, Validation. **Sharon A. Wilson:** Writing – review & editing, Validation. **Jeffrey M. Moore:** Writing – review & editing, Validation.

Declaration of competing interest

The authors declare they have no competing interest for this publication.

Data availability

Data will be made available on request.

Acknowledgements

A. Howard was partially supported through NASA MDAP grants 80NSSC18K1476 to the University of Colorado and 80NSSC19K1221 to the Smithsonian Institution through subcontracts to the Planetary Science Institute. A. Grau Galofre was partially supported by the European Commission through the Marie Sklodowska-Curie Action H2020-MSCA-IF-2020: MGFR-10102790. CaSSIS is a project of the University of Bern funded through the Swiss Space Office via ESA's PRODEX programme. CaSSIS data is being currently released to PSA. The instrument hardware development was also supported by the Italian Space Agency (ASI) (ASI-INAF agreement no. I/018/12/0), INAF/Astronomical Observatory of Padova, and the Space Research Center (CBK) in Warsaw. Support from SGF (Budapest), the University of Arizona (Lunar and Planetary Lab.), NASA, and the UK Space Agency (grant ST/R003025/1) are also gratefully acknowledged. Geospatial support for the development of ArcticDEM was provided by the Polar Geospatial Center under NSF-OPP awards 1043681, 1559691, and 2129685. DEMs provided by the Polar Geospatial Center under NSF-OPP awards 1043681, 1559691, 1542736, 1810976, and 2129685. A. Grau Galofre also kindly acknowledges the financial support from Région Pays de la Loire, AAP PULSAR 2023 - 271289. The authors thank Lauren Miller (Simkins) for insightful discussions about the glacial landscape of the Batson crater region. Detailed and constructive comments provided by two reviewers have been greatly appreciated in guiding manuscript revision.

Appendix A. Supplementary data

Supplementary data to this article can be found online at https://doi.org/10.1016/j.icarus.2024.116211.

References

Abyzov, S.S., Mitskevich, I.N., Poglazova, M.N., Barkov, N.I., Lipenkov, V.Ya., Bobin, N. E., Koudryashov, B.B., Pashkevich, V.M., Ivanov, M.V., 2001. Microflora in the basal strata at Antarctic ice core above the Vostok lake. Advances in Space Research 28 (4), 701–706. https://doi.org/10.1016/S0273-1177(01)00318-0. ISSN 0273-1177.

Anderson, R.B., Williams, R.M.E., Gullikson, A.L., Nelson, W.S., 2023. Morphology and paleohydrology of intracrater alluvial fans north of Hellas basin, Mars. Icarus 394, 115122. https://doi.org/10.1016/j.icarus.2022.115122.
Atkins, C.B., 2013. Geomorphological evidence of cold-gased glacier activity in south Victoria Land, Antarctica. Geol. Soc. Lond. Spec. Publ. 381 https://doi.org/10.1144/SP381.18, 299-318.
Baker, D.M.H., Carter, L.M., 2019. Probing supraglacial debris on Mars 2: crater morphology. Icarus 319, 264–280. https://doi.org/10.1016/j.icarus.2018.09.009.
Baker, D.M.H., Head, J.W., Marchant, D.R., 2010. Flow patterns of lobate debris aprons and lineated valley fill north of Ismeniae Fossae, Mars: evidence for extensive mid-latitude glaciation in the late amazonian. Icarus 207, 186–209. https://doi.org/10.1016/j.icarus.2009.11.017.
Ballantyne, C.K., 2002. Paraglacial geomorphology. Quat. Sci. Rev. 21, 1935–2017. https://doi.org/10.1016/S0277-3791(02)00005-7.
Banks, M.E., Lang, N.P., Kargel, J.S., McEwen, A.S., Baker, V.R., Grant, J.A., Pelletier, J. D., Strom, R.G., 2009. An analysis of sinuous ridges in the southern Argyre Planitia, Mars using HiRISE and CTX images and MOLA data. J. Geophys. Res. 114, E09003 https://doi.org/10.1029/2008JE003244.
Batchelor, G.L., Dowdeswell, J.A., Rignot, E., 2018. Submarine landforms reveal varying rates and styles of deglaciation in north-west Greenland fjords. Mar. Geol. 402, 60–80. https://doi.org/10.1016/j.margeo.2017.08.003.
Benn, D.L., Evans, D.J.A., 2010. Glaciers & Glaciation. Routledge, London, p. 802. https://doi.org/10.4324/9780203785010.
Bernhardt, H., Hiesinger, H., Reiss, D., Ivanov, M., Erkeling, G., 2013. Putative eskers and new insights into glacio-fluvial depositional settings in southern Argyre Planitia, Mars. Planet. Space Sci. 85, 261–278. https://doi.org/10.1016/j.pss.2013.06.022.
Berthling, I., Berti, C., Mancinelli, V., et al., 2020. Analysis of the paraglacial landscape in the Ny-Ålesund area and Blomstrandø Kongsfjorden, Svalbard, Norway. J. Maps 16, 818–833. https://doi.org/10.1080/17445647.2020.1837684.
Bishop, P., 1995. Drainage rearrangement by river capture, beheading and diversion. Prog. Phys. Geogr. 19, 449–473, 19.1177/030913339501900402.
Boatwright, B.D., Head, J.W., 2021. A Noachian proglacial paleolake on Mars: fluvial activity and lake formation within a closed-sorce drainage basin crater and implications for early Mars climate. Planet. Sci. J. 2, 52. https://doi.org/10.3847/PSJ/abc773.
Boatwright, B.D., Head, J.W., 2022a. Constraining early Mars glacial conditions from paleodischarge estimate of intracrater inverted channels. Geophys. Res. Lett. 49, e2022GL101227 https://doi.org/10.1029/2022GL101227.
Boatwright, B.D., Head, J.W., 2022b. Noachian proglacial paleolakes on Mars: regionally recurrent fluvial activity and lake formation within closed-source drainage basin craters. Planet. Sci. J. 3, 38. https://doi.org/10.3847/PSI/ac4d36.
Boatwright, B.D., Head, J.W., 2023. Inverted fluvial channels in Terra Sabaea, Mars: geomorphic evidence for proglacial paleolakes and widespread highlands glaciation in the late noachian-early hesperian. Planet. Space Sci. 225, 105621 https://doi.org/10.1016/j.pss.2022.105621.
Boffo, J.J., Ojha, L., Meyer, C.R., Ferrier, K.L., Palucis, M.C., 2022. Revisiting subglacial hydrology as an origin for Mars' valley networks. Earth Planet. Sci. Lett. 594, 117669 https://doi.org/10.1016/j.epsl.2022.117699.
Bouquety, A., Sejourné, A., Costard, F., Mercier, D., Bouley, S., 2019. Morphometric evidence of 3.6 Ga glacial valleys and glacial cirques in martian highlands south of Terra Sabaea. Geomorphology 334, 91–111. https://doi.org/10.1016/j.geomorph.2019.01.022.
Bouquety, A., Sejourné, A., Costard, F., Bouley, S., Leyguarda, E., 2020. Glacial landscape and paleoglaciation in Terra Sabaea: evidence for a 3.6 Ga polythermal plateau ice cap. Geomorphology 350. https://doi.org/10.1016/j.geomorph.2019.106858.
Bramson, A.M., Byrne, S., Putzig, N.E., Sutton, S., Plaut, J.J., Brothers, T.C., Holt, J.W., 2015. Widespread escess ice in Arcadia Planitia, Mars. Geophys. Res. Lett. 42, 6566–6574. https://doi.org/10.1002/2015GL064844.
Brouard, D., Lajeunesse, P., 2019. Glacial to postglacial submarine landform assemblages in fiords of northeastern Baffin island. Geomorphology 330, 40–56. https://doi.org/10.1016/j.geomorph.2019.01.007.
Brough, S., Hubbard, B., Hubbard, A., 2019. Area and volume of mid-latitude glacier-like forms on Mars. Earth Planet. Sci. Lett. 507, 10–20. https://doi.org/10.1016/j.espl.2018.11.031.
Burke, M.J., Brennand, T.A., Sjogren, D.B., 2015. The role of sediment supply in esker formation and ice tunnel evolution. Quat. Sci. Rev. 115, 50–77. https://doi.org/10.1016/j.quascirev.2015.02.017.
Burr, D.M., Williams, R.M.E., Wendell, K.D., Chojnacki, M., Emery, J.P., 2010. Inverted fluvial features in the Aeolis/Zephyria plana region, Mars: formation mechanism and initial paleodischarge estimates. J. Geophys. Res. 115, E07011. https://doi.org/10.1029/2009JE003496.
Butcher, F.E.G., Conway, S.J., Arnond, N.S., 2016. Are the Dorsa Argentea on Mars eskers? Icarus 275, 65–84. https://doi.org/10.1016/j.icarus.2016.03.028.
Butcher, F.E.G., Balme, M.R., Gallagher, C., Arnond, N.S., Conway, S.J., Hagermann, A., Lewis, S.R., 2017. Recent basal melting of a mid-latitude glacier on Mars. J. Geophys. Res. Planets 122, 2445–2468. https://doi.org/10.1002/2017JE005434.
Butcher, F.E.G., Balme, M.R., Conway, S.J., Gallagher, C., Arnond, N.S., Storrar, R.D., Lewis, S.R., Hagermann, A., 2020. Morphometry of a glacier-linked esker in NW Tempe Terra, Mars, and implications for sediment-discharge dynamics of subglacial drainage. Earth Planet. Sci. Lett. 524, 115325 https://doi.org/10.1016/j.epsl.2020.116325.
Butcher, F.E.G., Balme, M.R., Conway, S.J., Gallagher, C., Arnond, N.S., Storrar, R.D., Lewis, S.R., Hagermann, A., Davis, J.M., 2021. Sinuous ridges in Chukhung crater, Tempe Terra, Mars: implications for fluvial, glacial, and glaciofluvial activity. Icarus 357, 114131. https://doi.org/10.1016/j.icaarus.2020.114121.
Carr, M.H., Head, J.W., 2015. Martian surface/near-surface water inventory: sources, sinks, and changes with time. Geophys. Res. Lett. 42 (3), 726–732.
Carr, M., Head, J., 2019. Mars: formation and fate of a frozen Hesperian ocean. Icarus 319, 433. https://doi.org/10.1016/j.icarus.2016.08.021.
Chappelow, J.E., Sharpton, V.L., 2002. An improved shadow measurement technique for constraining the morphometry of simple impact craters. Meteorit. Planet. Sci. 37, 479–486. https://doi.org/10.1111/j.1945-5100.2002.tb00834.x.
Christensen, P.R., Jakosky, B.M., Kieffer, H.H., Malin, M.C., McSween, H.Y.J., Nealson, K., Mehall, G.L., Silverman, S.H., Ferry, S., Caplinger, M., Ravine, M., 2004. The Thermal emission imaging system (THEMIS) for the Mars 2001 odyssey mission. Space Sci. Rev. 110, 85–130. https://doi.org/10.1023/B:SPAC.0000021008.16305.94.
Christensen, P.R., Fergason, R.L., Edwards, C.S., Hill, J., 2013. THEMIS-derived thermal inertia mosaic of mars: product description and science results. In: 44th Lunar and Planetary Science Conference, The Woodlands, TX, Abstract 2822.
Clow, G.D., 1987. Generation of liquid water on Mars through the melting of a dusty snowpack. Icarus 72 (1), 95–127.
Conway, S.J., Balme, M.R., 2014. Decameter thick remant glacial ice deposits on Mars. Geophys. Res. Lett. 41, 5401–5409. https://doi.org/10.1002/2014GL060314.
Craddock, R.A., Howard, A.D., 2002. The case for rainfall on a warm, wet early Mars. J. Geophys. Res. 107, 5111. https://doi.org/10.1029/2001je001505.
Crown, D.A., Bleamaster, L.F.I., Mest, S.C., 2005. Styles and timing of volatile-driven activity in the eastern Hellas region of Mars. J. Geophys. Res. 110, E12S22 https://doi.org/10.1029/2005JE002496.
Cuffey, K.M., Paterson, W.S.B., 2010. *The physics of glaciers*, 4th edition. Butterworth & Heinemann, Elsevier.
Daubar, I.J., Atwood-Stone, C., Byrne, S., McEwen, A.S., Russell, P.S., 2014. The morphology of small fresh craters on Mars and the Moon. J. Geophys. Res. Planets 119, 2620–2639, 10,1012/2014JE004671.
Davis, J.M., Gupta, S., Balme, M., Grindrod, P.M., Fawdon, P., Dickeson, Z.I., Williams, R.M.E., 2019. A diverse array of fluvial depositional systems in Arabia Terra: evidence for mid-Noachian to early Hesperian rivers on Mars. J. Geophys. Res. Planets 124, 1913–1934. https://doi.org/10.1029/2019JE005976.
de Haas, T., Kleinhans, M.G., Carbonneau, P.E., Rubensdotter, L., Hauber, E., 2015. Surface morphology of fans in the high-Arctic periglacial environment of Svalbard: controls and processes. Earth Sci. Rev. 146, 163–182. https://doi.org/10.1016/j.earscirev.2015.04.004.
Denton, G.H., Sugden, D.E., 2005. Meltwater features that suggest Miocene ice-sheet overriding of the transantarctic mountains in Victoria Land, Antarctica. Geogr. Ann. 87A, 67–85. https://doi.org/10.1111/j.0435-3676.2005.00245.x.
Dewald, N., Livingstone, S.J., Clark, C.D., 2022. Subglacial meltwater routes of the Fennoscandian Ice Sheet. J. Maps 18 (2), 382–396.
Dickson, J.L., Head, J.W., Fassett, C.I., 2012. Patterns of accumulation and flow of ice in the mid-latitudes of Mars during the amazonian. Icarus 219, 723–732. https://doi.org/10.1016/j.icarus.2012.03.010.
Dickson, J., Kerber, L., Fassett, C., Ehlmann, B., 2018. A global, blended Ctx mosaic of mars with vectorized seam mapping: a new mosaicking pipeline using principles of non-destrictive image Editing. In: 49th Lunar and Planetary Science Conference, Woodlands, TX, Abstract 2840.
Dundas, C.M., Byrne, S., McEwen, A.S., 2015. Modelling the development of martian sublimation thermokarst landforms. Icarus 262, 154–169. https://doi.org/10.1016/j.icarus.2015.07.033.
Dundas, C.M., Bramson, A.M., Ojha, L., Wray, J.J., Mellon, M.T., Byrne, S., McEwen, A. S., Putzig, N.E., Viola, D., Sutton, S., Clark, E., Holt, J.W., 2018. Exposed subsurface ice sheets in the martian midlatitudes. Science 359, 199–201. https://doi.org/10.1126/science.aao1619.
Dundas, C.M., Mellon, M.T., Conway, S.J., Daubar, I.J., Williams, K.E., Ojha, L., Wray, J. J., Bramson, A.M., Byrne, S., McEwen, A.S., Posiolova, L.V., Speth, G., Viola, D., Landis, M.E., Morgan, G.A., Pathare, A.V., 2021. Widespread exposures of extensive clean shallow ice in the midlatitudes of Mars. J. Geophys. Res. Planets 126, e2020JE006617. https://doi.org/10.1029/2020JE006617.
Edwards, C.S., Christensen, P.R., Hill, J., 2011. Mosaicking of global planetary image datasets: 2. Modeling of wind streak thicknesses observed in thermal emission imaging system (THEMIS) daytime and nighttime infrared data. J. Geophys. Res, Planets 116, E10008. https://doi.org/10.1029/2010JE003755.
El-Maarry, M.R., Dohm, J.M., Michael, G., Thomas, N., Maruyama, S., 2013. Morphology and evolution of the ejecta of Hale crater in Argyre basin, Mars: results from high resolution mapping. Icarus 226, 905–922. https://doi.org/10.1016/j.icarus.2013.07.014.
Elvevold, S., Dallmann, W., Blomeier, D., 2007. Geology of Svalbard. Norwegian Polar Institute, Tromsø, Norway.
Fassett, C.I., Head, J.W.I., 2008. Valley network-fed, open-basin lakes on Mars: distribution and implications for Noachian surface and subsurace hydrology. Icarus. https://doi.org/10.1016/j.icarus.2008.06.016.
Fassett, C.I., Dickson, J.L., Head, J.W., Levy, J.S., Marchant, D.R., 2010. Supraglacial and proglacial valleys on amazonian Mars. Icarus 208, 086–110. https://doi.org/10.1016/j.icarus.2010.02.021.
Fastook, J.L., Head, J.W., 2014. Amazonian mid- to high-latitude glaciation on Mars: supply-limited ice sources, ice accumulation patterms, and concentric crater fill glacial flow and ice sequestration. Planet. Space Sci. 91, 60–76. https://doi.org/10.1016/j.pss.2013.12.002.
Fergason, R.L., Christensen, P.R., Kieffer, H.H., 2006. High-resolution thermal inertia derived from the thermal emission imaging system (THEMIS): thermal model and applications. J. Geophys. Res. E: Planets 111, E12004. https://doi.org/10.1029/2006JE002735.

Fergason, R. L., Hare, T. M., Laura, J., 2018. HRSC and MOLA Blended Digital Elevation Model at 200m v2. Astrogeology PDS Annex, U.S. Geological Survey, http://bit.ly/HRSC_MOLA_Blend_v0.
Flowers, G.E., 2015. Modelling water flow under glaciers and ice sheets. Proc. R. Soc. 471 (2176), 20140907 https://doi.org/10.1098/rspa.2014.0907.
Forget, F., Haberle, R.M., Montmessin, F., Levrard, B., Head, J.W., 2006. Formation of glaciers on Mars by atmospheric precipitation at high obliquity. Science 311, 368–371. https://doi.org/10.1126/science.1120335.
Forsberg-Taylor, N.K., Howard, A.D., Craddock, R.A., 2004. Crater degradation in the Martian highlands: morphometric analysis of the Sinus Sabaeus region and simulation modeling suggest fluvial processes. J. Geophys. Res. E: Planets 109, E05002. https://doi.org/10.1029/2004JE002242.
Fountain, A.G., Walder, J.S., 1998. Water flow through temperate glaciers. Rev. Geophys. 36 (3), 299–328.
Gallagher, C., Balme, M., 2015. Eskers in a complete, wet-based glacial system in the Phlegra Montes region, Mars. Earth Planet. Sci. Lett. 431, 96–109. https://doi.org/10.1016/j.epsl.2015.09.023.
Gallagher, C., Butcher, F.E.G., Balme, M., Smith, I., Arnond, N., 2021. Landforms indicative of regional warm based glaciation, Phlegra Montes, Mars. Icarus 355. https://doi.org/10.1016/j.icarus.2020.114175.
Garvin, J.B., Sakimoto, S.E.H., Frawley, J.J., Schnetzler, C., 2002. Global geometric properties of Martian impact craters. Lunar Planet. Sci. Conf. XXXIII, 1255 abstract.
Garvin, J.B., Sakimoto, S., Frawley, J.J., 2003. Craters on Mars: Global geometric properties from gridded MOLA topography. In: Sixth Intern. Conf. Mars, Pasadena, Ca. Abstract 3277.
Gilbert, G.K., Lake, B., 1890. Monograph 3. U. S. Geological Survey, Reston, p. 438.
Goudge, T.A., Morgan, A.M., de Quay, G.S., Fassett, C.I., 2021. The importance of lake breach floods for valley incision on early Mars. Nature 597, 645–649. https://doi.org/10.1038/s41586-021-03860-1.
Grant, J.A., Wilson, S.A., 2011. Late alluvial fan formation in southern Margaritifer Terra, Mars. Geophys. Res. Lett. 38, L08201 https://doi.org/10.1029/2011GL046844.
Grant, J.A., Wilson, S.A., 2012. A possible synoptic source of water for alluvial fan formation in southern Margaritifer Terra, Mars. Planet. Space Sci. 72, 44–52. https://doi.org/10.1016/j.pss.2012.05.020.
Grant, J.A., Wilson, S.A., 2019. Evidence for late alluvial activity in Gale crater, Mars. Geophys. Res. Lett. 46, 7287–7294. https://doi.org/10.1029/2019GL0834444.
Grau Galofre, A., Jellinek, A.M., Osinski, G.R., Zanetti, M., Kukko, A., 2018. Subglacial drainage patterns of Devon island, Canada: detailed comparison of rivers and subglacial meltwater channels. Cryosphere 12, 1461–1478. https://doi.org/10.5194/tc-12-1461-2018.
Grau Galofre, A., Jellinek, A.M., Osinski, G.R., 2020. Valley formation on early Mars by subglacial and fluvial erosion. Nat. Geosci. 13, 663–668. https://doi.org/10.1038/s41561-020-0618.
Grau Galofre, A., Bahia, R.S., Jellinek, A.M., Whipple, K.X., Gallo, R., 2020b. Did Martian valley networks substantially modify the landscape? Earth Planet. Sci. Lett. 547, 116482.
Grau Galofre, A., Whipple, K.X., Christensen, P.R., Conway, S.J., 2022. Valley networks and the record of glaciation on ancient Mars. Geophys. Res. Lett. 49 https://doi.org/10.1020/2022GL097974 e2022GL097974.
Greenwood, S.L., Clark, C.D., Hughes, A.L.C., 2007. Formalising an inversion methodology for reconstructing ice-sheet retreat patterns from meltwater channels: appliation to the British ice sheet. J. Quat. Sci. 22, 637–645 doi10.1002/jqs.1083.
Gullikson, A.L., Anderson, R.B., Williams, R.M.E., 2023. Spatial and temporal distribution of sinuous ridges in southeastern Terra Sabaea and the northern region of Hellas Planitia, Mars. Icarus 394, 115399. https://doi.org/10.1016/j.icarus.2022.115399.
Gwinner, K., Scholten, F., Spiegel, M., Schmitt, R., Giese, B., Oberst, J., Heipke, C., Jaumann, R., Neukum, G., 2009. Derivation and validation of high-resolution digital terrain models from Mars express HRSC data. Photogramm. Eng. Remote. Sens. 9, 1127–1142.
Hack, J.T., 1960. Interpretation of erosional topography in humid temperate regions. Am. J. Sci. 258-A, 80–97.
Hargitai, H.I., Gulick, V.C., 2017. Knobby terrains at the sources of the navua-hadriacus drainage systems on mars: what are the knobs. In: Lunar and Planetary Science Conference 48. Absract 1763.
Hargitai, H.I., Gulick, V.C., Glines, N.H., 2017a. Discontinuous drainage systems formed by highland precipitation and ground-water outflow in the Navua Valles and southwest Hadriacus Mons regions, Mars. Icarus 294, 172–200. https://doi.org/10.1016/j.icarus.2017.03.005.
Hargitai, H.I., Gulick, V.C., Glines, N.H., 2017b. Navua Valles and Hadriacus Mons: Discontinuous Channels, Paleolakes, Knobby Terains and Mound Fields. In: Astrobiology Science Conference 2017, Abstract 3621.
Hargitai, H.I., Gulick, V.C., Glines, N.H., 2018a. The geology of the Navua Valles region of Mars. J. Maps 14, 504–508. https://doi.org/10.1080/17445647.2018.1496858.
Hargitai, H.I., Gulick, V.C., Glines, N.H., 2018b. Paleolakes of Northeast Hellas: precipitation, groundwater-fed, and fluvial lakes in the Navua-Hadriacus-Ausonia Region, Mars. Astrobiology 18, 1435–1459. https://doi.org/10.1089/ast.2018.1836.
Hargitai, H.I., Gulick, V.C., Glines, N.H., 2019. Evolution of the Navua Valles region: implications for Mars' paleoclimatic history. Icarus 330, 91–102.
Harris, D.R., 1980. Exhumed paleochannels in the lower cretaceous cedar mountain formation near Green River. Brighan Young Univ. Geol. Stud. 27, 51–66.
Hartmann, W.K., 2005. Martian cratering 8: isochron refinement and the chronology of Mars. Icarus 174, 294–320. https://doi.org/10.1016/j.icarus.2004.11.023.
Hartmann, W.K., Daubar, I.J., 2017. Martian cratering 11. Utilizing decameter scale crater populations to study martian history. Meteorit. Planet. Sci. 52, 493–510. https://doi.org/10.1111/maps.12807.
Hartmann, W.K., Neukum, G., 2001. Cratering chronology and the evolution of Mars. Space Sci. Rev. 96, 165–194. https://doi.org/10.1023/A:1011945222010.
Hättestrand, C., Clark, C.D., 2006. The glacial geomorphology of Kola Peninsula and adjacent areas in the Murmansk Region, Russia. J. Maps 2, 30–42. https://doi.org/10.4113/jom.2006.41.
Hauber, E., Reiss, D., Ulrich, M., 2011. Landscape evolution in Martian mid-latitude regions: insights from analogous periglacial landforms in Svalbard. In: Balme, M.R., et al. (Eds.), Martian Geomorphology. Geological Society. Special Publication, London, pp. 111–131. https://doi.org/10.1144/SP356.7.
Hayden, A.T., Lamb, M.P., Fischer, W.W., Ewing, R.C., McElroy, B.J., Williams, R.M.E., 2019. Formation of sinuous ridges by inversion of river-channel belts in Utah, USA, with implications for Mars. Icarus 332, 92–110. https://doi.org/10.1016/j.icarus.2019.04.019.
Head, J.W., Marchant, D.R., 2003. Cold-based mountain glaciers on Mars: western Arsia Mons. Geology 31, 641–644. https://doi.org/10.1130/0091-7613(2003)031<0641:CMGOMW>2.0.CO;2.
Head, J.W., Marchant, D.R., 2014. The climate history of early Mars: insights from the Antarctic McMurdo dry Valleys hydrologic system. Antarct. Sci. 26, 774–800. https://doi.org/10.1017/S0954102014000686.
Head, J.W., Pratt, S., 2001. Extensive Hesperian-aged south polar ice sheet on Mars: evidence for massive melting and retreat, and lateral flow and pending of meltwater. J. Geophys. Res.Planets 106, 12275–12299. https://doi.org/10.1029/200JE001359.
Head, J.W., Mustard, J.F., Kreslavsky, M.A., Milliken, R.E., Marchant, D.R., 2003. Recent ice ages on Mars. Nature 426 (6968), 797–802.
Head, J.W., Neukum, G., Jaumann, R., Hiesinger, H., Hauber, E., Carr, M., Masson, P., Foing, B., Hoffmann, H., Kreslavsky, M., Werner, S., Milkovich, S., van Gasselt, S., Team, H.C.-I., 2005. Tropical to mid-latitude snow and ice accumulation, flow and glaciation on Mars. Nature 434, 346–351. https://doi.org/10.1038/nature03359.
Hobley, D.E.J., Howard, A.D., Moore, J.M., 2014. Fresh shallow valleys in the Martian midlatitudes as features formed by meltwater flow beneath ice. J. Geophys. Res. Planets 119, 128–153. https://doi.org/10.1002/2013JE004396.
Holt, J.W., Savaenili, A., Plaut, J.J., Head, J.W., Phillips, R.J., Seu, R., Kempf, S.D., Choudhary, P., Young, D.A., Putzig, N.E., Biccari, D., Gim, Y., 2008. Radar sounding evidence for buried glaciers in the southern mid-latitudes of Mars. Science 322, 1235–1238. https://doi.org/10.1126/science.1164236.
Howard, A.D., 1971. Simulation model of stream capture. Geol. Soc. Am. Bull. 82, 1355–1375. https://doi.org/10.1130/0016-7606(1971)82[1355:SMOSC]2.0.CO;2.
Howard, A.D., 1978. Origin of the stepped topography of the Martian poles. Icarus 34, 581–599. https://doi.org/10.1016/0019-1035(78)90047-7.
Howard, A.D., 1981. Etched plains and braided ridges of the south polar region of Mars: features produced by basal melting of ground ice? [Abstract]. reports of the planetary geology program -1981 NASA tech. Memorandum 84211, 286–288.
Howard, A.D., 2000. The role of eolian processes in forming surface features of the martian polar layered deposits. Icarus 144, 267–288. https://doi.org/10.1006/icar.1999.6305.
Howard, A.D., 2007. Simulating the development of martian highland landscapes through the interaction of impact cratering, fluvial erosion, and variable hydrologic forcing. Geomorphology 91, 332–363. https://doi.org/10.1016/j.geomorph.2007.04.017.
Howard, A.D., Moore, J.M., 2004. Scarp-bounded benches in Gorgonum Chaos, Mars: Formed beneath an ice-covered lake? Geophys. Res. Lett. 31, L01702 https://doi.org/10.1029/2003GL018925.
Howard, A.D., Moore, J.M., 2011. Late Hesperian to early amazonian midlatitude Martian valleys: evidence from Newton and Gorgonum basins. J. Geophys. Res. 116, E05003 https://doi.org/10.1029/2010JE003782.
Howard, A.D., Wilson, S.A., Morgan, A.M., Moore, J.M., White, O.L., 2021. Light-toned deposit in the northeastern Hellas basin formed by terrain-conforming airfall sedimentation. Icarus 360. https://doi.org/10.1016/j.icarus.2021.114356.
Hubbard, B., Milliken, R.E., Kargel, J.S., Limaye, A.B., Souness, C., 2011. Geomorphological characterisation and interpretation of a mid-latitude glacier-like form: Hellas Planitia, Mars. Icarus 211, 330–346. https://doi.org/10.1016/j.icarus.2010.10.021.
Hubbard, B., Souness, C., Brough, S., 2014. Glacier-like forms on Mars. Cryosphere 8, 2047–2061. https://doi.org/10.5194/tc-8-2047-2014.
Irwin III, R.P., Maxwell, T.A., Howard, A.D., Craddock, R.A., Moore, J.M., 2005. An intense terminal epoch of widespread fluvial activity on early Mars: 2. increased runoff and paleolake development. J. Geophys. Res. 110, E12S15 https://doi.org/10.1029/2005JE002460.
Jaumann, R., Neukum, G., Behnke, T., Duxbury, T.C., Eichentopf, K., Flohrer, J., Gasselt, S.V., Giese, B., Gwinner, K., Hauber, E., Hoffmann, H., Hoffmeister, A., Köhler, U., Matz, K.-D., McCord, T.B., Mertens, V., Oberst, J., Pischel, R., et al., 2007. The high-resolution stereo camera (HRSC) experiment on Mars express: instrument aspects and experiment conduct from interplanetary cruise through the nominal mission. Planet. Space Sci. 55, 928–952. https://doi.org/10.1016/j.pss.2006.12.003.
Johnson, A., Raack, J., Hauber, E., 2019. Possible Recessional Moraines in the Nilosyrtis Mensae Region, Mars. In: 50th Lunar and Planetary Science Conference, Woodlands, TX, Abstract 3085.
Kamb, B., 1987. Glacier surge mechanism based on linked cavity configuration of the basal water conduit system. J. Geophys. Res. 92, 9083–9100. https://doi.org/10.1029/JB092iB09p09083.
Kargel, J.S., Baker, V.R., Beget, J.E., Lockwood, J.F., Pewe, T.L., Shaw, J.S., Strom, R.G., 1995. Evidence of ancient continental-glaciation in the Martian northern plains. J. Geophys. Res.Planets 100, 5351–5368. https://doi.org/10.1029/94JE02447.

Karlstrom, L., Gajjar, P., Manga, M., 2013. Meander formation in supraglacial streams. J. Geophys. Res. Earth Surf. 118, 1897–1907. https://doi.org/10.1002/jgrf.20135.
Kehew, A.E., Piotrowski, J.A., Jørgenson, F., 2012. Tunnel valleys: concepts and controversies — a review. Earth Sci. Rev. 113, 33–58. https://doi.org/10.1016/j.earscirev.2012.02.002.
Kneissl, T., van Gasselt, S., Neukum, G., 2011. Map-projection-independent crater size-frequency determination in GIS environments – new software tool for ArcGIS. Planet. Space Sci. 59, 1243–1254. https://doi.org/10.1016/j.pss.2010.03.015.
Knighton, A.D., Nanson, G.C., 1993. Anastomosis and the continuum of channel pattern. Earth Surf. Process. Landf. 18, 613–625. https://doi.org/10.1002/esp3290180705.
Kostama, V.P., Ivanov, M.A., Raitala, J., Törmänen, T., Korteniemi, J., Neukum, G., 2010. Evidence for multiple ice deposits on the northeastern rim of Hellas basin, Mars. Earth Planet. Sci. Lett. 294, 321–331. https://doi.org/10.1016/j.epsl.2009.11.021.
Kraal, E.R., Asphaug, E., Moore, J.M., Howard, A.D., Bredt, A., 2008. Catalogue of large alluvial fans in martian impact craters. Icarus 194, 101–110. https://doi.org/10.1016/j.icarus.2007.09.028.
Kreslavsky, M., Head, J.W., 2002a. Fate of outflow channel effluents in the northern lowlands of Mars: the Vastitas Borealis formation as a sublimation residue from frozen bodies of water. J. Geophys. Res, Planets 107, 5121. https://doi.org/10.1029/2001JE001831.
Kreslavsky, M.A., Head, J.W., 2002b. Mars: nature and evolution of young latitude-dependent water-ice-rich mantle. Geophys. Res. Lett. 29 https://doi.org/10.1029/2002GL015392.
Laskar, J., Correia, A.C.M., Gastineau, M., Joutel, F., Levrard, B., Robutel, P., 2004. Long term evolution and chaotic diffusion of the insolation quantities of Mars. Icarus 170, 343–364. https://doi.org/10.1016/j.icarus.2004.04.005.
Levy, J.S., Head, J.W., Marchant, D.R., 2010. Concentric crater fill in the northern mid-latitudes of Mars: formation processes and relationships to similar landforms of glacial origin. Icarus 209, 390–404. https://doi.org/10.1016/j.icarus.2010.03.036.
Levy, J.S., Fassett, C.I., Head, J.W., Schwartz, C., Watters, J.L., 2014. Sequestered glacial ice contribution to the global Martian water budget: geometric constraints on the volume of remnant, midlatitude debris-covered glaciers. J. Geophys. Res. Planets 119, 2188–2196. https://doi.org/10.1002/2014JE004685.
Levy, J.S., Goudge, T.A., Head, J.W., Fassett, C.I., 2017. Candidate volcanic and impact-induced ice depressions on Mars. Icarus 285, 185–194. https://doi.org/10.1016/j.icarus.2016.10.021.
Levy, J.S., Fassett, C.I., Holt, J.W., Parsons, R., Cipolli, W., Goudge, T.A., Tebolt, M., Kuentz, L., Johnson, J., Ishraque, F., Cvijanovich, B., Armstrong, I., 2021. Surface boulder banding indicates Martian debris-covered glaciers formed over multiple glaciations. PNAS 118, e2015971118. https://doi.org/10.1073/pnas.201597118.
Lewington, E.L., Livingstone, S.J., Clark, C.D., Sole, A.J., Storrar, D.R., 2020. A model for interaction between conduits and surrounding hydraulically connected distributed drainage based on geomorphological evidence from Keewatin, Canada. Cryosphere 14, 2949–2976. https://doi.org/10.5194/tc-14-2949-2020.
Lewis, A.R., Marchant, D.R., Kowalewski, D.E., Baldwin, S.L., Webb, L.E., 2006. The age and origin of the Labyrinth, western Dry Valleys, Antarctica: evidence for extensive middle Miocene subglacial floods and freshwater discharge to the Southern Ocean. Geology 34, 513–516. https://doi.org/10.1130/G22145.1.
Livingstone, S.J., Li, Y., Rutishauser, A., Sanderson, R.J., Winter, K., Mikucki, J.A., Björnsson, H., Bowling, J.S., Chu, W., Dow, C.F., Fricker, H.A., 2022. Subglacial lakes and their changing role in a warming climate. Nat. Rev. Earth Environ. 3, 106–124. https://doi.org/10.1038/s43017-021-00246-9.
Makaske, B., 2001. Anastomosing rivers: a review of their classification, origin and sedimentary products. Earth Sci. Rev. 53, 149–196. https://doi.org/10.1016/S0012-8252(00)00038-6.
Malin, M.C., Calvin, W.M., Clancy, R.T., Edgett, K.S., Edwards, L., Haberle, R.M., James, P.B., Lee, S.W., Ravine, M.A., Thomas, P.C., Wolff, M.J., Bell, I.J.F., Cantor, B. A., Caplinger, M.A., 2007. Context camera investigation on board the Mars reconnaissance Orbiter. J. Geophys. Res. E: Planets 112, E05S04. https://doi.org/10.1029/2002JE001900.
Mangold, N., 2003. Geomorphic analysis of lobate debris aprons on Mars at Mars orbiter camera scale: evidence for ice sublimation initiated by fractures. J. Geophys. Res. 108, 8021. https://doi.org/10.1029/2002JE001885.
Mangold, N., Howard, A.D., 2013. Outflow channels with deltaic deposits in Ismenius Lacus, Mars. Icarus 226, 385–401. https://doi.org/10.1016/j.icarus.2013.05.040.
Mantelli, E., Camporeale, C., Ridolfi, L., 2015. Supraglacial channel inception: modeling and processes. Water Resour. Res. 51 https://doi.org/10.1002/2015WR017075.
Marchant, D.R., Jamieson, S.S.R., Sugden, D.E., 2011. The geomorphic signature of massive subglacial floods in Victoria Land, Antarctica. Am. Geophys. Union Geophys. Monogr. 192, 111–127. https://doi.org/10.1029/2020GM000943.
Matsubara, Y., Howard, A.D., Drummond, S.A., 2011. Hydrology of early Mars: lake basins. J. Geophys. Res. 116, E04001 https://doi.org/10.1029/2010JE003739.
McEwen, A.S., Hansen, C.J., Delamere, W.A., Grant, J.A., Gulick, V.C., Herkenhoff, K.E., Keszthelyi, L., Kirk, R.L., Mellon, M.T., Squyres, S.W., Thomas, N., Weitz, C.M., Eliason, E.M., Bergstrom, J.W., Bridges, N.T., 2007. Mars reconnaissance orbiter's high resolution imaging science experiment (HiRISE). J. Geophys. Res. E: Planets 112, E05S02. https://doi.org/10.1029/2005JE002605.
McKay, C.P., Wharton Jr., R.A., Squyres, S.W., Clow, G.D., 1985. Thickness of ice on perennially frozen lakes. Nature 313, 561–562. https://doi.org/10.1038/313561a0.
Meade, H.E., 1968. The catastrophic Late Pleistocene Bonneville Flood in the snake River Plain, Idaho. U.S. Geological Survey, Washington, p. 52.
Mest, S.C., Crown, D.A., Harbert, W., 2010. Watershed modeling in the Tyrrhena Terra region of Mars. J. Geophys. Res. 115, E09001 https://doi.org/10.1029/2009JE003429.
Michael, G.G., 2013. Planetary surface dating from crater size-frequency measurements: multiple resurfacing episodes and differential isochron fitting. Icarus 226, 885–890. https://doi.org/10.1016/j.icarus.2013.07.004.
Michael, G.G., Neukum, G., 2010. Planetary surface dating from crater size-frequency distribution measurements: partial resurfacing events and statistical age uncertainty. Earth Planet. Sci. Lett. 294, 223–229. https://doi.org/10.1016/j.epsl.2009.12.041.
Moore, J.M., Howard, A.D., 2005. Large alluvial fans on Mars. J. Geophys. Res. 110, E04005 https://doi.org/10.1029/2004JE002352.
Moore, J.M., Wilhelms, D.E., 2001. Hellas as a possible site of ancient ice-covered lakes on Mars. Icarus 154, 258–276. https://doi.org/10.1006/icar.2001.6736.
Morgan, A.M., Howard, A.D., Hobley, D.E.J., Moore, J.M., Dietrich, W.E., Williams, R.M. E., Burr, D.M., Grant, J.A., Wilson, S.A., Matsubara, Y., 2014. Sedimentary and climatic environment of alluvial fans in the martian Saheki crater and a comparison with terrestrial fans in the Atacama Desert. Icarus 229, 131–156. https://doi.org/10.1016/j.icarus.2013.11.007.
Morgan, A.M., Wilson, S.A., Howard, A.D., 2022. The global distribution and morpholotic characteristics of fan-shaped sedimentary landforms on Mars. Icarus 385, 115137. https://doi.org/10.1016/j.icarus.2022.115137.
Morino, Costanza, Susan, Conway, Meven, Philippe, Coralie, Peignaux, Kristian, Svennevig, Antoine, Lucas, Axel, Noblet, Gioachino, Roberti, Frances, Butcher, Jake, Collins-May, 2023. Permafrost molards as an analogue for ejecta-ice interactions at Hale Crater, Mars. Icarus 391, 115363. https://doi.org/10.1016/j.icarus.2022.115363. ISSN 0019-1035.
Mustard, J.F., Cooper, C.D., Rifkin, M.K., 2001. Evidence for recent climate change on Mars from the identification of youthful near-surface ground ice. Nature 412, 4111–4114. https://doi.org/10.1038/35086515.
Nanson, G.C., Knighton, A.D., 1996. Anabranching rivers; their cause, character and classification. Earth Surf. Process. Landf. 21, 217–239. https://doi.org/10.1003/(SICI)1096-9837(199603)21:3<217::AID-ESP611>3.0.CO;2-U.
O'Connor, J.E., 1993. Hydrology, hydraulics, and geomorphology of the Bonneville flood. Geol. Soc. Am. Spec. Pap. 274 https://doi.org/10.1130/SPE274, Boulder.
Ojala, A.E., Mäkinen, J., Kajuutti, K., Ahokangas, E., Palmu, J.P., 2022. Subglacial evolution from distributed to channelized drainage: evidence from the Lake Murtoo area in SW Finland. Earth surface processes and landforms 47 (12), 2877–2896.
Osinski, G.R., Lee, P., Spray, J.G., Parnell, J., Lim, D.S.S., Bunch, T.E., Cockell, C.S., Glass, B., 2005. Geological overview and cratering model for the Haughton impact structure, Devon island, Canadian high Arctic. Meteorit. Planet. Sci. 40, 1759–1776. https://doi.org/10.1111/j.1945-5100.2005.tb00145.x.
Palucis, M.C., Dietrich, W.E., Hayes, A.G., Williams, R.M.E., Gupta, S., Mangold, N., Newsom, H., Hardgrove, C., Calef, F.I., Sumner, D.Y., 2014. The origin and evolution of the Peace Vallis fan system that drains to the Curiosity landing area, Gale Crater, Mars. J. Geophys. Res. Planets 119. https://doi.org/10.1002/2013JE004583.
Palucis, M.C., Dietrich, W.E., Williams, R.M.E., Hayes, A.G., Parker, T., Sumner, D.Y., Mangold, N., Lewis, K., Newson, H., 2016. Sequence and relative timing of large lakes in gale crater (Mars) after the formation of mount sharp. J. Geophys. Res, Planets 121, 472–496. https://doi.org/10.1002/2015JE004905.
Palucis, M.C., Jasper, J., Garczynski, B., Dietrich, W.E., 2020. Quantitative assessment of uncertainties in modeled crater retention ages. Icarus 341, 113623 doi: 10.111016.112020.113623.
Parker, G., 1975. Meandering of supraglacial melt streams. Water Resour. Res. 11, 551–552. https://doi.org/10.1029/WR011i004p00551.
Parsons, R.A., Moore, J.M., Howard, A.D., 2013. Evidence for a short period of hydrologic activity in Newton crater, Mars, near the Hesperian-amazonian transition. J. Geophys. Res. 118, 1082–1093. https://doi.org/10.1002/jgre.20088.
Parsons, R.A., Kanzaki, T., Hemmi, R., Miyamoto, H., 2020. Cold-based glaciation of Pavonis Mons, Mars: evidence for moraine deposition during glacial advance. Prog. Earth Planet. Sci. 7 (13) https://doi.org/10.1186/s40645-020-0323-9.
Perron, J.T., Dietrich, W.E., Howard, A.D., McKean, J.A., Pettiga, J.R., 2003. Ice-driven creep on Martian debris slopes. Geophys. Res. Lett. 30 (14), 1747. https://doi.org/10.1029/2003GL017603.
Peterson, G., Johnson, M.D., 2018. Hummock corridors in the south-central sector of the Fennoscandian ice sheet, morphometry and pattern. Earth Surf. Process. Landf. 43, 919–929. https://doi.org/10.1002/esp.4294.
Peterson, G., Johnson, M.D., Smith, C.A., 2017. Glacial geomorphology of the south Swedish uplands - focus on the spatial distribution of hummock tracts. J. Maps 13, 534–544. https://doi.org/10.1080/17445647.2017.1336121.
Plaut, J.J., Safaeinili, A., Holt, J.W., Phillips, R.J., Campbell, B.A., Carter, L.M., Leuschen, C., Gim, Y., Seu, R., Team, S., 2008. Radar evidence for ice in lobate debris aprons in the mid-northern latitudes of Mars. Lunar Planet. Inst. Conf. Abstracts 39, 2290.
Quantin-Nataf, C., Lozac'h, L., Thollot, P., Loizeau, D., Bultel, B., Fernando, J., Allemand, P., Dubuffet, F., Poulet, F., Ody, A., Clenet, H., Leyrat, C., Harrisson, S., 2018. MarsSI: Martian surface data processing information system. Planet. Space Sci. 150, 157–170. https://doi.org/10.1016/j.pss.2017.09.014.
Rains, R.B., Shaw, J., Sjogren, D.B., Munro-Stasiuk, M.J., Skoye, K.R., Young, R.R., Thompson, R.T., 2002. Subglacial tunnel channels, Porcupine hills, southwest Alberta, Canada. Quat. Int. 90, 57–65. https://doi.org/10.1016/S1040-6182(01)00092-1.
Ramirez, R.M., Craddock, R.A., 2018. The geological and climatological case for a warmer and wetter early Mars. Nat. Geosci. 11, 230–237. https://doi.org/10.1038/s41561-018-0093-9.
Ramirez, R.M., Craddock, R.A., Usui, T., 2020. Climate simulations of early Mars with estimated precipitation, runoff, and erosion eates. J. Geophys. Res. Planets 125, e2019JE006160. https://doi.org/10.1029/2019JE006160.
Ravier, E., Buoncristiani, J.F., Clerc, S., Guiraud, M., Menzies, J., Portier, E., 2014. Sedimentological and deformational criteria for discriminating subglaciofluvial

deposits from subaqueous ice-contact fan deposits: AP leistocene example (I reland). Sedimentology 61 (5), 1382–1410.
Rodriguez, J.A.P., Noe Dobrea, E., Kargel, J.S., Baker, V.R., Crown, D.A., Webster, K.D., Berman, D.C., Wilhelm, M.B., Buckner, D., 2020. The oldest highlands of Mars may be massive dust fallout deposits. Nat. Commun. 10, 10347. https://doi.org/10.1038/s41596-020-64676-z.
Schoof, C., 2010. Ice-sheet acceleration driven by melt supply variability. Nature 468 (7325), 803–806.
Sharpe, D.R., Lesemann, J.-E., Knight, R.D.B.A.K., 2021. Regional stagnation of the western Keewatin ice sheet and the significance of meltwater corridors and esker, northern Canada. Can. J. Earth Sci. 58, 1005–1026. https://doi.org/10.1139/cjes-2020-0136.
Shaw, J., 2002. The meltwater hypothesis for subglacial bedforms. Quat. Int. 90, 5–22. https://doi.org/10.1016/S1040-6182(01)00089-1.
Simkins, L.M., Greenwood, S.L., Winsborrow, M.C.M., Bjarnadóttir, L.R., Lepp, A.P., 2023. Advances in understanding subglacial meltwater drainage from past ice sheets. Ann. Glaciol. 63, 83–87. https://doi.org/10.1017/aog.2023.16.
Sinha, R.K., Murty, S.V.S., 2015. Amazonian modification of Moreux crater: record of recent and episodic glaciation in the Protonilus Mensae region of Mars. Icarus 245, 122–144. https://doi.org/10.1016/j.icarus.2014.09.028.
Smith, I.B., Holt, J.W., Spiga, A., Howard, A.D., Parker, G., 2013. The spiral troughs of Mars as cyclic steps. J. Geophys. Res, Planets 118, 1835–1857. https://doi.org/10.1002/jgre.20142.
Soderblom, L.A., Kreidler, T.J., Masursky, H., 1973. Latitudinal distribution of a debris mantle on the martian surface. J. Geophys. Res. 78, 4117–4122. https://doi.org/10.1029/JB078i020p04117.
Souness, C., Hubbard, B., Milliken, R.E., Quincey, D., 2012. An inventory and population-scale analysis of martian glacier-like forms. Icarus 217 (1), 243–255.
Spiga, A., Smith, I., 2018. Katabatic jumps in the Martian northern polar regions. Icarus 308, 197–208. https://doi.org/10.1016/j.icarus.2017.10.021.
Stokes, M.F., Larsen, I.J., Goldberg, S.L., McCoy, S.W., Prince, P.P., Perron, J.T., 2023. The erosional signature of drainage divide motion along the blue ridge escarpment. J. Geophys. Res. Earth Surf. 128 https://doi.org/10.1029/2022JF006757.
Stuurman, C.M., Osinski, G.R., Holt, J.W., Levy, J.S., Brothers, T.C., Kerrigan, M., Campbell, B.A., 2016. SHARAD detection and characterization of subsurface water ice deposits in Utopia Planitia, Mars. Geophys. Res. Lett. 43, 9484–9491. https://doi.org/10.1002/2016GL070138.
Syverson, K.M., Mickelson, D.M., 2009. Origin and significance of lateral meltwater channels formed along a temperate glacier margin, glacier bay, Alaska. Boreas 38, 132–145. https://doi.org/10.1111/j.1502-3885.2008.00042.x.
Thomas, N., Cremonese, G., Ziethe, R., Gerber, M., Brändli, M., Bruno, G., Erismann, M., Gambicori, L., Gerber, T., Ghose, K., Gruber, M., Gubler, P., Mischler, H., Jost, J., Piazza, D., Pommerol, A., Reider, M., Roloff, V., Servonet, A., Trottman, W., Uthaicharoenpong, T., Zimmermann, C., Vernani, D., Johnson, M., et al., 2017. The Colour and stereo surface imaging system (CaSSIS) for the ExoMars trace gas orbiter. Space Sci. Rev. 212, 1897–1944. https://doi.org/10.1007/s11214-017-0421-1.
Trottier, A.-P., Lajeunesse, P., Gagnon-Poiré, P., 2020. Morphological signatures of deglaciation and postglacial sedimentary processes in a deep fjord-lake (Grand Lake, Labrador). Earth Surf. Process. Landf. 45, 928–947. https://doi.org/10.1002/esp.4786.
Turbet, M., Forget, F., 2019. The paradoxes of the late Hesperian Mars ocean. Sci. Rep. 9, 5717. https://doi.org/10.1039/s41598-01942030-2.
Turbet, M., Forget, F., Head, J.W., Wordsworth, R., 2017. 3D modelling of the climatic impact of outflow channel formation events on early Mars. Icarus 288, 10–36.
Utting, D.J., Ward, B.C., Little, E.C., 2009. Genesis of hummocks in glaciofluvial corridors near the Keewatin ice divide, Canada. Boreas 38, 471–481. https://doi.org/10.1111/j.1502-3885.2008.00074.x.
Van der Vegt, P., Janszen, A., Moscariello, A., 2012. Tunnel valleys: current knowledge and future perspectives. Geol. Soc. Lond. Spec. Publ. 368 https://doi.org/10.1144/SP368.13.
Vérité, J., Livingstone, S.J., Ravier, E., McMartin, I., Campbell, J., Lewington, E.M.L., Dewald, N., Clark, C.D., Sole, A.J., Storrar, R.D., 2023. Conceptual model for the formation of bedforms along subglacial meltwater corridors (SMCs) by variable ice-water-bed interactions. Earth Surf. Process. Landf. 49, 170–196. https://doi.org/10.2002/esp.5725.
Viola, D., McEwen, A.S., Dundas, C.M., Byrne, S., 2015. Expanded secondary craters in the Arcadia Planitia region, Mars: evidence for tens of Myr-old shallow subsurface ice. Icarus 248, 190–204. https://doi.org/10.1016/j.icarus.2014.10.032.
Warner, N.H., Gupta, S., Calef, F., Grindrod, P., Boll, N., Goddard, K., 2015. Minimum effective area for high resolution crater counting of martian terrains. Icarus 245, 198–240, 110.1016/j.icarus.2014.1009.1024.
Warren, A.O., Holo, S., Kite, E.S., Wilson, S.A., 2021. Overspilling small craters on a dry Mars: insights from breach erosion modeling. Earth Planet. Sci. Lett. 554 https://doi.org/10.1016/j.epsl.2020.116671.
Warren, A.O., Wilson, S.A., Kite, E.S., 2023. Mechanisms for overspilling fresh, YOUNG martian craters multiple times, and above the lowest points on their rims. In: 54th Lunar and Planetary Science Conference, Absract 2584.
Whitfield, E., Harvey, A.M., 2012. Interaction between the controls on fluvial system development: tectonics, climate, base level and river capture–Rio Alias, Southeast Spain. Earth Surf. Process. Landf. 37 (13), 1387–1397.
Williams, R.M.E., Zimbelman, J.R., Johnston, A.K., 2006. Aspects of alluvial fan shape indicative of formation process: a case study in southwestern California with application to Mojave Crater fans on Mars. Geophys. Res. Lett. 33, L10201 https://doi.org/10.1029/2005GL025618.
Williams, R.M.E., Irwin, R.P.I., Zimbelman, J.R., 2009. Evaluation of paleohydrologic models for terrestrial inverted channels: implications for application to martian sinuous ridges. Geomorphology 107, 300–315. https://doi.org/10.1016/j.geomorph.2008.12.015.
Williams, R.M.E., Deanne Rogers, A., Chojnacki, M., Boyce, J., Seelos, K.D., Hardgrove, C., Chuang, F.C., 2011. Evidence for episodic alluvial fan formation in far western Terra Tyrrhena, Mars. Icarus 211, 222–237. https://doi.org/10.1016/j.icarus.2010.10.001.
Wilson, S.A., Howard, A.D., 2022. The distribution of Glacio-Fluvial landforms in the southern Mid-Latitude Region of Mars. In: 53rd Lunar and Planetary Science Conference, Abstract 2904.
Wilson, S.A., Moore, J.M., Howard, A.D., 2010. Evidence for ancient lakes in the Hellas region. In: Cabrol, N.A. (Ed.), Lakes on Mars, Ch. 7. Elsevier, pp. 195–222. https://doi.org/10.1016/C2009-0-06633-1.
Wilson, S.A., Howard, A.D., Moore, J.M., Grant, J.A., 2016. A cold-wet middle-latitude environment on Mars during the Hesperian-amazonian transition: evidence from northern Arabia valleys and paleolakes. J. Geophys. Res. Planets 121, 1667–1694. https://doi.org/10.1002/2016JE005052.
Wilson, S.A., Morgan, A.M., Howard, A.D., Grant, J.A., 2021. The global distribution of craters with alluvial fans and deltas on Mars. Geophys. Res. Lett. 48, e2020GL091653 https://doi.org/10.1029/2020GL091653.
Woodley, S.Z., Butcher, F.E.G., Fawdon, P., Clark, C.D., Ng, F.S.L., Davis, J.M., Gallagher, C., 2022. Multiple sites of recent wet-based glaciation identified from eskers in western Tempe Terra, Mars. Icarus 386, 115147. https://doi.org/10.1016/j.icarus.2022.115147.
Wordsworth, R.D., 2016. The climate of early Mars. Annu. Rev. Earth Planet. Sci. 44, 381–408. https://doi.org/10.1146/annurev-earth-060115-012355.
Wordsworth, R., Forget, F., Millour, E., Head, J.W., Madeleine, J.-B., Charnay, B., 2013. Global modeling of the early martian climate under a denser CO_2 atmosphere: water cycle and ice evolution. Icarus 222, 1–19, 0.1016/j.icarus.2012.09.036.
Zhang, M., Zhao, J., Xiao, L., Xu, Y., Bugiolacchi, R., Wang, J., 2023. Fan-shaped deposits in the northern Hellas region, Mars: implications for the evolution of water reservoir and climate. Icarus 395, 115470. https://doi.org/10.1016/j.icarus.2023.115470.